

2011

Development of a real-time high-resolution 3D ultrasound imaging system

Cesar Augusto Sandoval Leon
West Virginia University

Follow this and additional works at: <https://researchrepository.wvu.edu/etd>

Recommended Citation

Sandoval Leon, Cesar Augusto, "Development of a real-time high-resolution 3D ultrasound imaging system" (2011). *Graduate Theses, Dissertations, and Problem Reports*. 2226.
<https://researchrepository.wvu.edu/etd/2226>

This Thesis is protected by copyright and/or related rights. It has been brought to you by the The Research Repository @ WVU with permission from the rights-holder(s). You are free to use this Thesis in any way that is permitted by the copyright and related rights legislation that applies to your use. For other uses you must obtain permission from the rights-holder(s) directly, unless additional rights are indicated by a Creative Commons license in the record and/ or on the work itself. This Thesis has been accepted for inclusion in WVU Graduate Theses, Dissertations, and Problem Reports collection by an authorized administrator of The Research Repository @ WVU. For more information, please contact researchrepository@mail.wvu.edu.

**DEVELOPMENT OF A REAL-TIME HIGH-RESOLUTION 3D ULTRASOUND IMAGING
SYSTEM**

by

César Augusto Sandoval León

**Thesis submitted to the College of Engineering and Mineral Resources
at West Virginia University
in partial fulfillment of the requirements
for the degree of**

**Master of Science
in
Mechanical Engineering**

Approved by

**Osama Mukdadi, Ph.D., Committee Chairperson
Timothy McGraw, Ph.D.
Victor Mucino, Ph.D.**

Department of Mechanical and Aerospace Engineering

**Morgantown, West Virginia
2011**

Keywords: 3D Ultrasound Imaging; High-Resolution Ultrasound; Atherosclerosis.

© 2011 Sandoval León, César Augusto

ABSTRACT

DEVELOPMENT OF A REAL-TIME HIGH-RESOLUTION 3D ULTRASOUND IMAGING SYSTEM

by César Augusto Sandoval León

In this work a real-time high-resolution 3D ultrasound imaging system is developed, allowing the 3D acquisition and imaging of high-resolution ultrasound data for biomedical applications. The system uses ultrasound transducers in the ranges of 30 to 100 MHz, and allows full access of the radiofrequency (RF) ultrasound data for the 3D image reconstruction. This work includes the development of two graphical user interfaces in C++ to interact with a high-resolution ultrasound system and to image the high-resolution ultrasound data. In addition, a methodology is described and implemented in the system for 3D ultrasound reconstruction and visualization. The development of these GUIs allows easy 3D high-resolution ultrasound acquisition and imaging to any user with basic knowledge in ultrasound and with only minimal and faster training in the system and the GUIs. This capability opens the system to any researcher or person interested in performing experimentations with high-resolution ultrasound.

The high-resolution 3D ultrasound imaging system is tested to assess atherosclerosis using different mouse models. To assess atherosclerosis, a series of *in vitro* studies are performed to 3D scan vessels of mouse aortas and carotids vessels with atherosclerosis, as well as mouse hearts with atherosclerosis. The apolipoprotein E-knockout (APOE) and the apolipoprotein E-A1 adenosine receptor double knockout (DKO) mice model with their wild type control (C57) are used. Three-dimensional reconstructions were rendered showing good matches with the samples morphology. In addition, 3D sections of the data are reconstructed showing atherosclerotic plaque in the samples. The 3D ultrasound reconstruction allows for us to analyze a sample from outside and inside by rotating around any angle and cropping non-relevant data, allowing us to observe shape and appearance of the 3D structures. Finally, after reconstructing and analyzing the 3D ultrasound images, a 3D quantitative assessment of atherosclerotic

plaque is performed. After analyzing the samples, the plaque lesions of DKO mouse model exhibits smaller areas than those of the APOE mouse model. Additionally, the C57 mouse model is clean of any atherosclerosis. These findings are in agreement with a previous study of our group for these mouse models.

DEDICATION

I would like to dedicate this work to my family, my mom Emérita, my grandma Ana, and my brother Jairo, for giving me their support and strength to accomplish this stage of my life, and especially to Alana, for helping and encouraging me during this process.

ACKNOWLEDGEMENTS

I would like to thank my advisor Dr. Osama Mukdadi for giving me the opportunity to work with him, for his support, patience, dedication and help in this work. Also, I would like to thank the members of my graduate committee, Dr. Timothy McGraw and Dr. Victor Mucino, for their valuable help and advice. I also want to give thanks to all of the team members of the Ultrasonics Lab at WVU: Dr. Ahmed, Ahmed, Nithin, and Jeremy, and all my friends for their company and advice. I want to give special thanks to Dr. Teng for providing all of the animal samples for this work. Finally, I thank God for giving me the strength and health to accomplish this stage of my life.

TABLE OF CONTENTS

ABSTRACT.....	ii
DEDICATION	iv
ACKNOWLEDGEMENTS.....	v
TABLE OF CONTENTS	vi
LIST OF FIGURES	viii
LIST OF TABLES.....	xii
LIST OF SYMBOLS.....	xiii
- CHAPTER 1 -	1
INTRODUCTION.....	1
1.1. PROBLEM DEFINITION.....	1
1.2. THESIS OBJECTIVES	2
1.3. CONTRIBUTION AND IMPACT.....	3
- CHAPTER 2 -	5
BACKGROUND & LITERATURE REVIEW.....	5
2.1. ULTRASOUND IMAGING	5
2.2. HIGH-RESOLUTION ULTRASOUND IMAGING	7
2.3. 3D ULTRASOUND IMAGING.....	8
2.4. ATHEROSCLEROSIS IMAGING BY ULTRASOUND	10
- CHAPTER 3 -	12
HIGH-RESOLUTION ULTRASOUND IMAGE RECONSTRUCTION.....	12
3.1. RAW IMAGE	13
3.2. TIME GAIN COMPENSATION (TGC)	15
3.3. FILTERING.....	19
3.4. SYNTHETIC APERTURE FOCUSING TECHNIQUE (SAFT)	22
3.5. ENVELOPE DETECTION (HILBERT TRANSFORM)	26
3.6. LOGARITHMIC COMPRESSION	28
3.7. SPATIAL RESOLUTION ASSESSMENT	32
- CHAPTER 4 -	37
GRAPHICAL USER INTERFACES (GUIs) FOR HIGH-RESOLUTION ULTRASOUND ACQUISITION AND HIGH-RESOLUTION ULTRASOUND IMAGING	37
4.1. HIGH-RESOLUTION ULTRASOUND ACQUISITION SYSTEM GUI.....	37
4.1.1. System Description	39
4.1.2. Acquisition Modalities.....	41
4.1.3. Acquisition Cards Parameters.....	43
4.1.4. Motion Controller Parameters	45
4.1.5. Experiment Specifications Parameters.....	46
4.1.6. High-Resolution Ultrasound Transducer Description.....	47
4.2. HIGH-RESOLUTION ULTRASOUND IMAGING SYSTEM GUI.....	49
4.2.1. Raw Image.....	50
4.2.2. Time Gain Compensation (TGC).....	53
4.2.3. Filtering.....	55
4.2.4. Synthetic Aperture Focusing Technique (SAFT)	57

4.2.5.	<i>Envelope Detection (Hilbert Transform)</i>	59
4.2.6.	<i>Logarithmic Compression</i>	60
4.2.7.	<i>Save Ultrasound Image</i>	62
4.2.8.	<i>Ultrasound Reconstruction Sequence</i>	63
4.2.9.	<i>3D High-Resolution Ultrasound Reconstruction</i>	64
- CHAPTER 5 -		65
3D RECONSTRUCTION FOR ATHEROSCLEROSIS		65
5.1.	3D RECONSTRUCTION METHODOLOGY	65
5.2.	MICE SAMPLES ORIGIN	66
5.3.	3D RECONSTRUCTION RESULT.....	70
5.3.1.	<i>3D Mouse Aortas and Carotids</i>	71
5.3.2.	<i>3D Mouse Hearts</i>	80
5.4.	3D QUANTITATIVE ASSESSMENT OF ATHEROSCLEROTIC PLAQUE	82
- CHAPTER 6 -		83
CONCLUSIONS & FUTURE WORK		83
REFERENCES		85

LIST OF FIGURES

Figure 2.1. Schematic diagrams used for 3D ultrasound imaging [36].	9
Figure 2.2. 3D ultrasound rendering techniques.	10
Figure 2.3. Ultrasound image with atherosclerosis plaque outlined [51].	11
Figure 3.1. High-resolution ultrasound imaging procedure.	12
Figure 3.2. Original RF ultrasound signal.	13
Figure 3.3. RF ultrasound signal after cropped.	14
Figure 3.4. Ultrasound image of raw data.	15
Figure 3.5. Time gain compensation curves frequently used in ultrasonic imaging [58].	16
Figure 3.6. Time gain compensation curve used.	16
Figure 3.7. RF ultrasound signal during TGC.	17
Figure 3.8. Ultrasound image after time gain compensation (TGC).	18
Figure 3.9. Band pass filter specifications.	19
Figure 3.10. Hamming window with N=64.	20
Figure 3.11. RF ultrasound signal during filtering.	21
Figure 3.12. Ultrasound B-mode image after filtering.	22
Figure 3.13. Synthetic aperture focusing technique (SAFT) sketch [62].	22
Figure 3.14. RF ultrasound signal after SAFT.	24
Figure 3.15. Ultrasound image after SAFT focusing.	25

Figure 3.16. Comparison of envelope detection techniques [63].	26
Figure 3.17. RF ultrasound signal during envelope detection.	27
Figure 3.18. Ultrasound image after envelope detection with Hilbert transform.	28
Figure 3.19. Example of dynamic range of the RF signals until display [8].	29
Figure 3.20. RF ultrasound signal during logarithmic compression.....	30
Figure 3.21. Final ultrasound image after logarithmic compression.	31
Figure 3.22. Experimental calculation of spatial resolutions for ultrasound images. Arbitrary example data.	33
Figure 3.23. Ultrasound resolution assessed by processing step.	36
Figure 4.1. High-resolution ultrasound acquisition system GUI.	38
Figure 4.2. Some mal-function protections in the ultrasound acquisition GUI.	39
Figure 4.3. Block diagram of the high-resolution ultrasound system.....	40
Figure 4.4. High-resolution ultrasound acquisition system GUI after loaded.	42
Figure 4.5. Acquisition modalities using the acquisition GUI.....	42
Figure 4.6. High-resolution ultrasound acquisition system GUI after selecting the acquisition modality X/Y.....	43
Figure 4.7. Acquisition parameters using the acquisition GUI.....	44
Figure 4.8. High-resolution ultrasound acquisition system GUI after activating the RF visualization.	44
Figure 4.9. Motion controller parameters using the acquisition GUI.	45

Figure 4.10. High-resolution ultrasound acquisition system GUI after applying the motion parameters.	46
Figure 4.11. Experiment specifications parameters using the acquisition GUI.....	47
Figure 4.12. Frequency spectrum for the 55.2 MHz single-element ultrasound transducer [66]......	48
Figure 4.13. High-resolution ultrasound imaging GUI.....	50
Figure 4.14. Opening raw data using the imaging GUI.	51
Figure 4.15. Cropping ultrasound data using the imaging GUI.....	52
Figure 4.16. High-resolution ultrasound imaging GUI after selecting the raw data.....	53
Figure 4.17. Time gain compensation (TGC) using the imaging GUI.	54
Figure 4.18. High-resolution ultrasound imaging GUI after TGC.	55
Figure 4.19. Filtering using the imaging GUI.....	56
Figure 4.20. High-resolution ultrasound imaging GUI after filtering.	57
Figure 4.21. SAFT focusing using the imaging GUI.....	58
Figure 4.22. High-resolution ultrasound imaging GUI after SAFT focusing.	58
Figure 4.23. Envelope detection (Hilbert transform) using the imaging GUI.	59
Figure 4.24. High-resolution ultrasound imaging GUI after envelope detection.	60
Figure 4.25. Logarithmic compression using the imaging GUI.	61
Figure 4.26. High-resolution ultrasound imaging GUI after logarithmic compression....	62
Figure 4.27. Save ultrasound image button in imaging GUI.	62
Figure 4.28. Saving ultrasound image window using the imaging GUI.....	63

Figure 4.29. Apply all the steps and 3D reconstruction buttons in imaging GUI.....	63
Figure 4.30. 3D ultrasound reconstruction using the imaging GUI.....	64
Figure 5.1. Transversal views of the 3D ultrasound reconstruction of the aorta APOE M1 50 weeks – Sample 5.....	70
Figure 5.2. 3D ultrasound reconstruction of aorta DKO F (50 weeks, sample 8) and aorta C57 F (70 weeks, sample 6).....	72
Figure 5.3. 3D ultrasound reconstruction of aorta APOE M 50 weeks – Sample 3.	74
Figure 5.4. 3D ultrasound reconstruction of aorta APOE F 50 weeks – Sample 1.	75
Figure 5.5. 3D ultrasound reconstruction of aorta DKO M1 50 weeks – Sample 9.....	76
Figure 5.6. 3D ultrasound reconstruction of aorta DKO F1 50 weeks – Sample 8.	77
Figure 5.7. 3D ultrasound reconstruction of aorta C57 M 70 weeks – Sample 7.....	78
Figure 5.8. 3D ultrasound reconstruction of aorta C57 F 70 weeks – Sample 6.	79
Figure 5.9. 3D ultrasound reconstruction of mouse heart APOE M1 16 weeks – Sample 9.	80
Figure 5.10. 3D ultrasound reconstruction of mouse heart DKO M1 16 weeks – Sample 13.....	81

LIST OF TABLES

Table 2.1. General classifications of ultrasonic diagnostic modalities [8]	6
Table 3.1. Ultrasound resolution measured at the different processing steps.....	35
Table 4.1. Technical specifications for the 55.2 MHz single-element ultrasound transducer	48
Table 5.1. Mouse aortas and carotids samples by name	68
Table 5.2. Mouse aortas and carotids samples by category	68
Table 5.3. Mouse hearts samples by name	69
Table 5.4. Mouse hearts samples by category	69

LIST OF SYMBOLS

2D	acronym for “Two Dimensional”
3D	acronym for “Three Dimensional”
A/D	acronym for “Analog to Digital”
APOE	acronym for “Apolipoprotein E-knockout”
BMP	acronym for “Bitmap file”
CT	acronym for “Computed Tomography”
CVD	acronym for “Cardiovascular Disease”
D/A	acronym for “Digital to Analog”
DKO	acronym for “Apolipoprotein E and A1 Adenosine Receptor Double Knockout”
FIR	acronym for “Finite Impulse Response”
FOV	acronym for “Field of View”
GUI	acronym for “Graphical User Interface”
HT	acronym for “Hilbert Transform”
IED	acronym for “Ideal envelope detector”
MRI	acronym for “Magnetic Resonance Imaging”
PET	acronym for “Positron Emission Tomography”
RF	acronym for “Radiofrequency”
ROI	acronym for “Region of Interest”
SAFT	acronym for “Synthetic Aperture Focusing Technique”
TGC	acronym for “Time Gain Compensation”

- CHAPTER 1 -

INTRODUCTION

1.1. Problem Definition

Typically, medical ultrasound applications use transducers in the range of 1 to 15 MHz to create 2D images from the organ scanned, achieving spatial resolutions on the order of millimeters. The use of transducers in this range of frequencies allows both a good image resolution (small wavelength) and a good penetrating depth. However, some specialized medical applications require a spatial resolution in the order of micrometers, such as medical applications in ophthalmology, intravascular ultrasound, dermatology, and small animal imaging. This higher level of spatial resolution requires specialized transducers of high frequencies up to 120 MHz.

In traditional ultrasound imaging, 2D images are scanned by an ultrasound technician and these are mentally transformed into a 3D interpretation for an accurate medical diagnostic. The limitations with this method include that the ultrasound technician is not capable of seeing the morphology of a sample, he or she is not capable of accurately measuring 3D volumes as organs or tumors, and the results depend on the expertise of the ultrasound technician. Therefore, the purpose of 3D ultrasound imaging is to overcome these limitations.

A common disease imaged with ultrasound is atherosclerosis. Atherosclerosis is a cardiovascular disease (CVD) developed in the arteries, and it is considered the main disease affecting the cardiovascular system. In fact, CVDs causes a higher mortality rate than cancer [1] and it is affecting most of the Eastern and Western countries. In addition, CVDs were the number one cause of death in United States until the year 2005, and in 2007 it was estimated to be affecting 1 out of 3 Americans [2].

1.2. Thesis Objectives

The overall objective of this work is to develop a real-time 3D high-resolution ultrasound imaging system for biomedical imaging. A user friendly ultrasound system is required to achieve easy acquisition of the radiofrequency data; efficient control of the system components; and accurate 3D reconstruction of the ultrasound data. A graphical user interface in C++ is developed to interact with the hardware components of the high-resolution ultrasound system, allowing the 3D acquisition and imaging of high-resolution ultrasound data for biomedical applications.

The specific task-based objectives of this work are as follows:

1. Develop a graphical user interface (GUI) in C++ to facilitate the interaction with the high-resolution ultrasound hardware system available in the Ultrasonic Laboratory at West Virginia University.
2. Develop a graphical user interface (GUI) in C++ for acquiring and imaging high-resolution ultrasound radiofrequency (RF) data.
3. Integrate the high-resolution ultrasound system with a 3D image reconstruction capability.
4. Test the high-resolution 3D ultrasound imaging system to assess atherosclerosis *in vitro* using different mouse models.

By achieving these aims, an easy 3D high-resolution ultrasound acquisition and imaging is possible. In addition, these capabilities are open to any researcher or person interested in performing experiments after a minimal and faster training in the system and the GUIs. Furthermore, the high-resolution 3D ultrasound imaging system is tested to assess atherosclerosis using different mouse models.

1.3. Contribution and Impact

In this work the development of a real-time high-resolution 3D ultrasound imaging system is documented, allowing the 3D acquisition and imaging of high-resolution ultrasound data for biomedical applications.

This work consisted of the development of a graphical user interface (GUI) in C++ to interact with a high-resolution ultrasound system for biomedical applications. The system used ultrasound transducers in the ranges of 30 to 100 MHz, and allows to the user from the radio frequency (RF) data acquisition through the B-mode imaging reconstruction. The GUI controls a two-axis (two translational) precision positioning system with 1 μm resolution, and the RF data can be acquired using up to 1 GHz sampling rate with 8 bits resolution or up to 400 MHz sampling rate with 14 bits resolution. The custom user-friendly GUI is designed using Microsoft Visual C++ to control both, the data acquisition board and the positioning system. In addition, all the signal processing techniques to reconstruct the ultrasound B-mode images are implemented in C++, including time gain compensation (TGC) and band pass filtering. In addition, a methodology was described and implemented in the system for 3D ultrasound reconstruction and visualization.

This project has many challenges; the more important are the integration in the GUI of the high-resolution ultrasound devices, such as the positioning system and the acquisition boards. As well, other challenges are the development in C++ of each ultrasound image reconstruction technique including time gain compensation (TGC) and envelope detection using Hilbert transform. The final challenge is to test the system to assess atherosclerosis using different mouse models, that involve good skills in ultrasound experimental setups and a good performance of the ultrasound system designed.

An important contribution of this work is the development of these GUIs, which provides easy 3D high-resolution ultrasound acquisition and imaging to any user with

basic knowledge in ultrasound and with only minimal and faster training in the system and the GUIs. This capability opens the system to any researcher or person interested in performing experiments with high-resolution ultrasound, including biomedical applications such as small animal imaging.

The high-resolution 3D ultrasound imaging system is tested to assess atherosclerosis using different mouse models. The apolipoprotein E-knockout (APOE) and the apolipoprotein E-A1 adenosine receptor double knockout (DKO) mice model with their wild type control (C57) are used. To assess atherosclerosis, a series of in vitro studies are performed to 3D scan vessels of mouse aortas and mouse carotids with atherosclerosis, in addition to mouse hearts of these mouse models with atherosclerosis. Three-dimensional reconstructions are rendered showing good matches with the samples morphology. In addition, 3D sections of the data are reconstructed showing atherosclerotic plaque in the samples. The 3D ultrasound reconstruction allows for us to analyze a sample from outside and inside by rotating around any angle and cropping non-relevant data, allowing us to observe shape and appearance of the 3D structures. Also, 3D reconstruction allows us to reconstruct B-mode images of the cross sectional and longitudinal views, that were not available initially with the original transversal scans. As well, 3D image reconstructions are used to locate and select 2D regions of interest (ROI) precisely instead of using a reference point or a surgical needle. Finally, after reconstructing and analyzing the 3D ultrasound images, a 3D quantitative assessment of atherosclerotic plaque is performed. After analyzing the samples, the plaque lesions of DKO mouse model exhibits smaller areas than those of the APOE mouse model. Additionally, the C57 mouse model was clean of any atherosclerosis. These findings are in agreement with a previous study of our group for these mouse models

- CHAPTER 2 -

BACKGROUND & LITERATURE REVIEW

This chapter will provide a background and a review of the published literature concerning ultrasound imaging, ultrasound modalities, and high-resolution ultrasound. In addition, the 3D ultrasound imaging and its medical applications will be presented. Finally, the contributions of recent published studies in atherosclerosis imaging will be reviewed.

2.1. Ultrasound Imaging

Ultrasound technology was realized as a potential imaging modality in the late 1940s [3]. After that, several groups of investigators started exploring medical diagnostic capabilities of ultrasound, taking advantage of the sonar and radar technology developed during World War II. The pioneer ultrasound imaging devices were developed concurrently in Japan [4], United States [5], and Sweden [6]. Today in medical imaging, ultrasound technology is the most utilized diagnostic imaging modality after conventional X-ray [7], and it is an important diagnostic tool at any medical facility. Some of the features of ultrasound imaging include that it is non-invasive and it is considered safe for patients. Also, ultrasound is less expensive than other imaging modalities of similar capabilities, it can produce images in real time, it is portable, and therefore it can be easily transported. However, some ultrasound restrictions are that organs containing bony structures and air cannot be adequately imaged without introducing specialized procedures.

During these nearly 70 years, the ultrasound has developed many imaging modalities. Some of the most important modalities of ultrasound imaging are shown in Table 2.1. Some modalities provide spatial information about the region of interest, and others give motion or velocity information. The spatial information ultrasound modalities include the amplitude mode (A-mode), brightness mode (B-mode), and constant depth

mode (C-mode) modalities. The motion or velocity information ultrasound modalities include ultrasound motion mode (M-mode) and wave Doppler devices.

Table 2.1. General classifications of ultrasonic diagnostic modalities [8]

A-Mode (one-dimensional)
B-Mode (two-dimensional)
Manual scanners
Real-time scanners
Mechanical
Electronic
Linear array
Phased array
M-mode (motion)
C-mode (through-transmission)
Doppler (velocity)
Continuous-wave
Audible-output
Analog-output
Spectrum-output
Doppler imagers
CW transverse scanners
Pulsed Doppler
Combined with B-mode (duplex)
Miscellaneous

The initial ultrasound application was the A-mode modality providing one dimensional information [9]. This mode is still being used for applications as midline echoencephalography [10] and ophthalmological scanning [11]. The A-mode ultrasound was rapidly substituted with the two dimensional B-mode ultrasound imaging [12]. B-mode imaging is currently the most used ultrasound modality and provides good spatial details. In addition, B-mode ultrasound allows users an easy understanding of the scanned objects. Other ultrasound modalities are continuous wave (CW) [13] and pulsed wave Doppler (PW) [14], that are used to measure velocity and motion of red blood cells in a pulsating blood vessel.

2.2. High-Resolution Ultrasound Imaging

Typically, medical ultrasound applications use transducers in the range of 1 to 15 MHz, achieving spatial resolutions on the order of millimeters. The use of transducers in this range of frequencies allows both a good image resolution (small wavelength) and a good penetrating depth, which is inversely proportional to the wave frequency (Section 3.7). However, some specialized medical applications require a spatial resolution in the order of micrometers, such as medical applications in ophthalmology, intravascular ultrasound, dermatology, and small animal imaging. For example, with the small size of mouse vasculature it requires a spatial resolution of 50 μm or less. This higher level of spatial resolution requires specialized transducers of high frequencies up to 120 MHz. The imaging with these frequencies of transducers is referred to in the literature as high-resolution ultrasound imaging or ultrasound biomicroscopy [15].

In the last few decades, many high-resolution ultrasound systems have been developed. In 1987, high-resolution ultrasound images of biological targets such as tumor spheroids started to be achieved using 100 MHz transducers [16]. After this, other high-resolution medical application incursions were in ophthalmology [17, 18], intravascular ultrasound [19, 20], dermatology [21, 22], and small animal imaging [23, 24]. Important achievements in high-resolution ultrasound imaging for small animals includes the imaging of an early mouse embryonic brain in 1995 [24], the *in utero* imaging of a mouse embryonic heart with a 40 MHz transducer in 1998[25], and the *in vivo* mice vasculature imaging in 2002 [26].

Nearly all of the high-resolution ultrasound studies are being conducted using custom high-frequency ultrasound systems, usually for *in vitro* studies and only some for *in vivo* studies. However, in the last few years a company located in Canada started to offer the Vevo system (Vevo 770 and 2100 from VisualSonics). The Vevo system is the only commercial system at the moment that allows the users to conduct *in vivo* high-frequency high-resolution ultrasound imaging. Some applications with this system include the microimaging of the thyroid gland in living mice [27], the examination of regional blood flow in a mouse kidney [28], between others [29-31].

2.3. 3D Ultrasound Imaging

In traditional ultrasound imaging, 2D images are scanned for an ultrasound technician and these are mentally transformed into a 3D interpretation for an accurate medical diagnostic. The limitations with this method include that the ultrasound technician is not capable of seeing the morphology of a sample, he or she is not capable of accurately measuring 3D volumes as organs or tumors, and the results depend on the expertise of the ultrasound technician. Therefore, the purpose of 3D ultrasound imaging is to overcome these limitations.

Three dimensional (3D) ultrasound imaging has been used since the last few decades, developing different techniques and styles for 3D ultrasound imaging [32-35]. There are mainly four different approaches for 3D ultrasound scanning [36]: the use of 2D array transducers, the mechanical scanning, and the scanning using freehand techniques with and without positioning information.

In the 2D array technique, the 3D ultrasound system keeps the transducer stationary and uses electronics to activate the different components of the 2D arrays producing a 3D image. However, due to the relatively small size of these transducers, their field of view is limited to imaging small region or organs. There are some publications in the fabrication and use of this transducer, and in 1991 a very advanced 2D arrays transducer used for medical imaging in real time was described [37].

The other three approaches include the motion of the transducer. Figure 2.1 shows schematic diagrams showing the typical types of transducer motion for 3D ultrasound imaging. Part (a) shows the linear motion approach, in which a sequence of parallel 2D images are collected and used to reconstruct the 3D image. Part (b) shows the tilt motion approach, in which a sequence of 2D images are acquired around a central axis, during the scanning time the transducer is tilted and the 3D image is reconstructed into a cone shape. These techniques can be applied for a mechanically ultrasound scanning or for a freehand ultrasound scanning. Our system at WVU has the linear motion approach with precise mechanical scanning, as will be shown in Section 4.1.

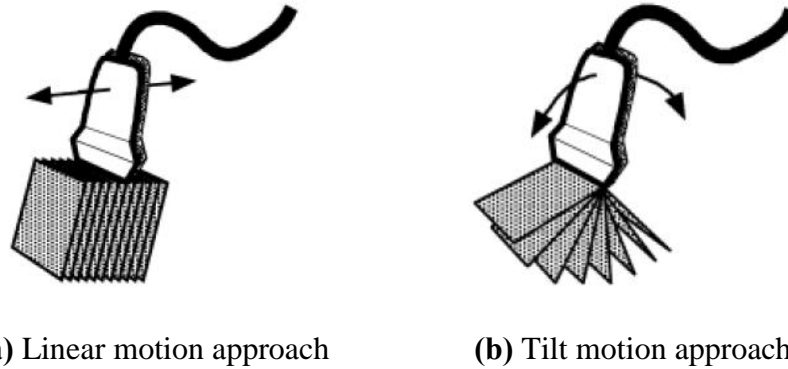


Figure 2.1. Schematic diagrams used for 3D ultrasound imaging [36].

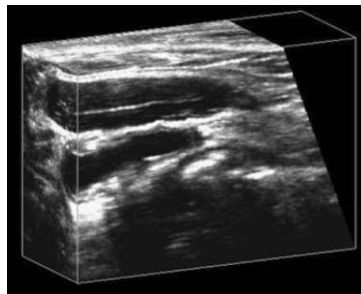
The mechanical ultrasound scanning consists of attaching the transducer to a mechanical motion system. During the scanning, the motion system moves the transducer in a linear or tilt approach saving the 2D images and each position acquired. The positions are later used for the 3D reconstruction, giving a very accurate image reconstruction.

In the freehand ultrasound scanning the transducer motion is provided by an ultrasound technician. The ultrasound technician needs to move the transducer with an appropriate constant velocity in a linear or tilt motion approach for the 3D reconstruction. In some cases, the 3D ultrasound systems provide the transducer with a positioning information system in order to improve the 3D reconstruction. The position information systems in the transducer interact with the 3D ultrasound systems by different sensors, which can be optical, magnetic, or wireless. The freehand motion is used since the mechanical motion systems can be considerably larger and inconvenient to use with some patients.

A series of publications can be found using these scanning approaches including for mechanical scanning [38, 39], for freehand with positioning information [40, 41], and for freehand without positioning information [42].

After the 3D ultrasound system finishes acquiring the images they reconstructs the data into a 3D volume, which can be viewed and manipulated interactively by the ultrasound technician with a variety of 3D visualization and rendering software. Even though there are many techniques for displaying 3D images, in 3D ultrasound the most

used are the multiplanar technique and the volume-based rendering technique. Figure 2.2 shows 3D ultrasound images reconstructed with these two techniques. Part (a) shows the multiplanar technique applied to a carotid artery [43], and part (b) shows the volume-based rendering technique applied to a 11-week-old fetus [44]. The multiplanar technique displays arbitrarily oriented 2D planes from the originally acquired images. On the other hand, the volume-based rendering technique displays the entire 3D data after it has been projected onto a 2D plane. For our studies at WVU, we used the volume-based rendering technique as it will be shown in Section 5.3



(a) Multiplanar [43]



(b) Volume-based [44]

Figure 2.2. 3D ultrasound rendering techniques.

2.4. Atherosclerosis Imaging by Ultrasound

Atherosclerosis is a cardiovascular disease (CVD) developed in the arteries, and it is considered the main disease affecting the cardiovascular system. In fact, CVDs causes a higher mortality rate than cancer [1] and it is affecting most of the Eastern and Western countries. In addition, CVDs was the number one cause of death in United States until the year 2005, and in 2007 it was estimated to be affecting 1 out of 3 Americans [2].

Atherosclerosis consists of the accumulation of fatty materials, such as cholesterol, around the artery wall. Also, atherosclerosis affects all the cardiovascular system flow and it is a potential cause of a stroke. Atherosclerosis lesions are divided in six types [45]. Types I, II, and III are the initial, the fatty streak, and the intermediate lesion types respectively. Advanced atherosclerotic lesions can also be subdivided into

three main types: IV, V, and VI. To recognize the different stages of atherosclerosis, several imaging techniques have been applied. However, for small animals, examples of atherosclerosis imaging techniques include electron-beam computed tomography (CT) [46], magnetic resonance imaging (MRI) [47], positron emission tomography (PET) [48], optical coherent tomography [49], and high-resolution ultrasound [50].

Figure 2.3 shows an ultrasound image for a human carotid artery with atherosclerosis plaque outlined [51]. In addition, some 3D ultrasound imaging employed for the identification and localization of potential atherosclerotic plaques are described for humans in [52-54], and for small animals in [55].

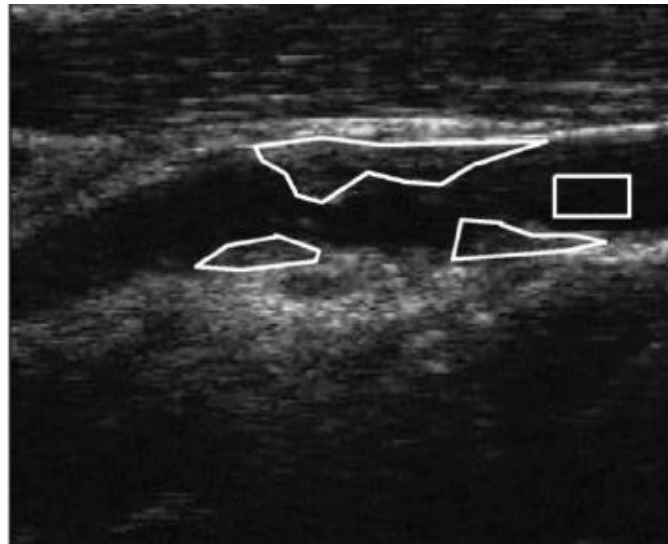


Figure 2.3. Ultrasound image with atherosclerosis plaque outlined [51].

- CHAPTER 3 -

HIGH-RESOLUTION ULTRASOUND IMAGE RECONSTRUCTION

The procedure used in this work for high-resolution ultrasound imaging is outlined in Figure 3.1. It consists of six processing steps [56, 57] before obtaining the final high-resolution B-mode ultrasound image. The procedure begins with the opening and imaging of the ultrasound raw signals, improvement of the strength and quality of the ultrasound data using time gain compensation (TGC), digital filtering of the data, focusing of the ultrasound data using the synthetic aperture focusing technique (SAFT), envelope detection using Hilbert transform, and finally, contrast improvement using logarithmic compression. In addition, all the techniques had been implemented in Microsoft Visual C++ (Microsoft Corp., Redmond, WA), allowing an easier and faster performance than other programming languages such as MATLAB (The MathWorks, Inc., Natick, MA, USA), as it will be described in Section 4.2.

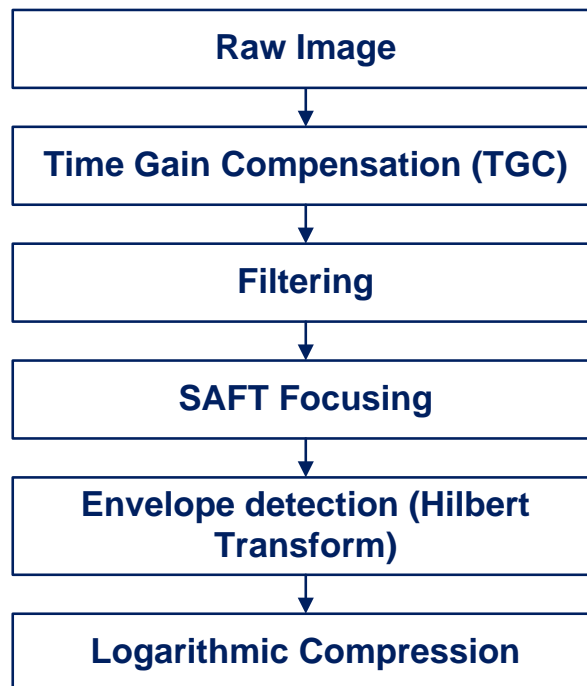


Figure 3.1. High-resolution ultrasound imaging procedure.

This chapter describes the high-resolution ultrasound image reconstruction procedure in detail, from the step of raw image to the step of logarithmic compression. The example figures used in this chapter are reconstructed using ultrasound signals acquired in our custom ultrasound system with a 55.2 MHz transducer and sampling rate of 400 MHz (14 bits of analog to digital (A/D) resolution). Ultrasound signals corresponds from a cross sectional scan of an 8 μm (diameter) tungsten wire phantom and to a 50-week-male APOE mouse aorta after removing the adventia layer cross section.

3.1. Raw Image

The first step is opening the raw data with the radiofrequency (RF) ultrasound signals, where no manipulation or processing is applied. Figure 3.2 shows an example of an original RF signal bounced back for an 8 μm wire phantom experiment. Usually, original signals begin with a strong reflection due to the pulse excitation of the transducer followed by reflections as the transmitted pulse progresses through the tissue. Figure 3.2 shows a peak reflection around sample number 8100 corresponding to the middle of the 8 μm wire phantom, where the sampling rate was 400 MHz with 14 bits of A/D resolution. RF ultrasound signals are then cropped to remove unwanted regions, reduce data size and improve the imaging performance. Figure 3.3 shows the original RF signal of the wire phantom experiment after the cropping procedure. Note that the initial reflections were removed, and better visualization was obtained.

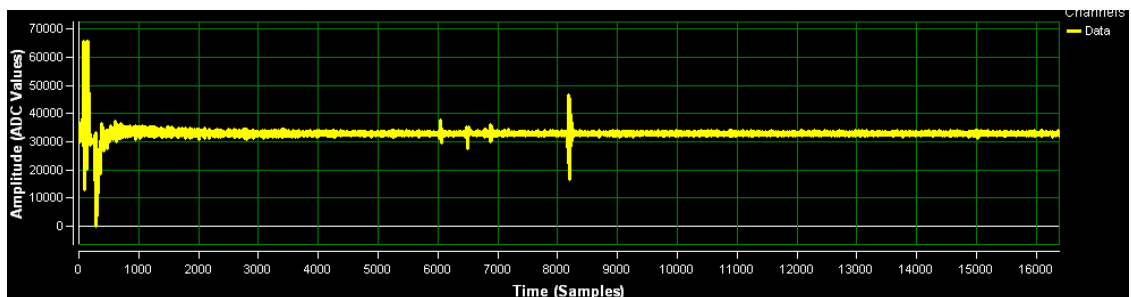


Figure 3.2. Original RF ultrasound signal.

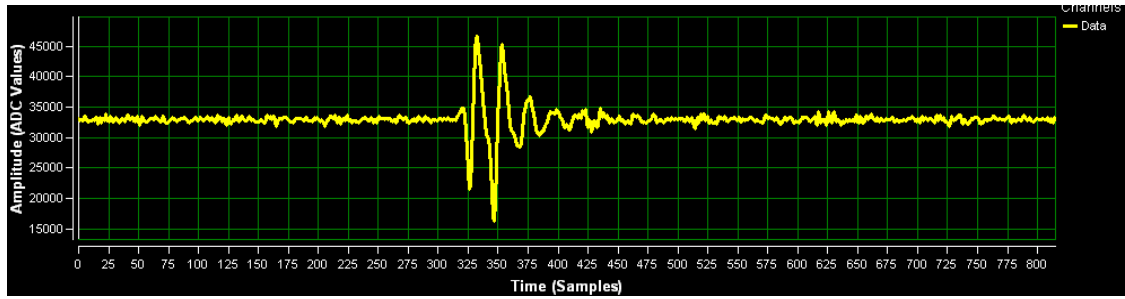
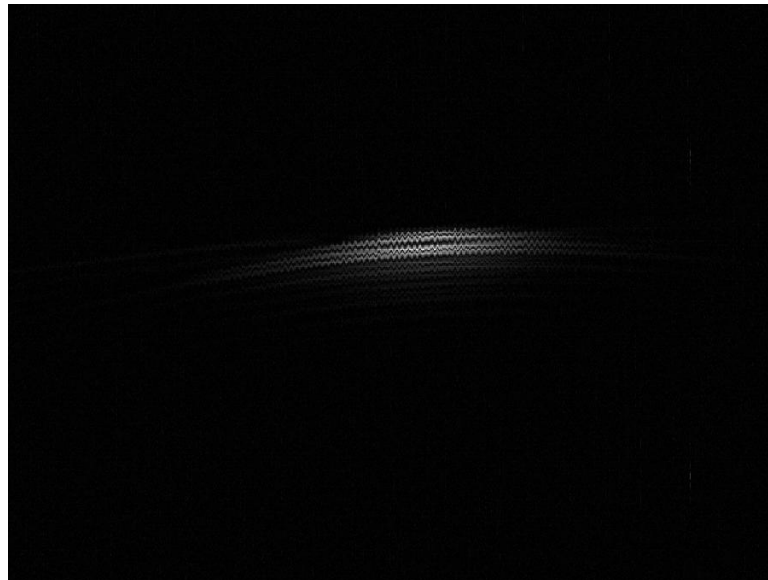
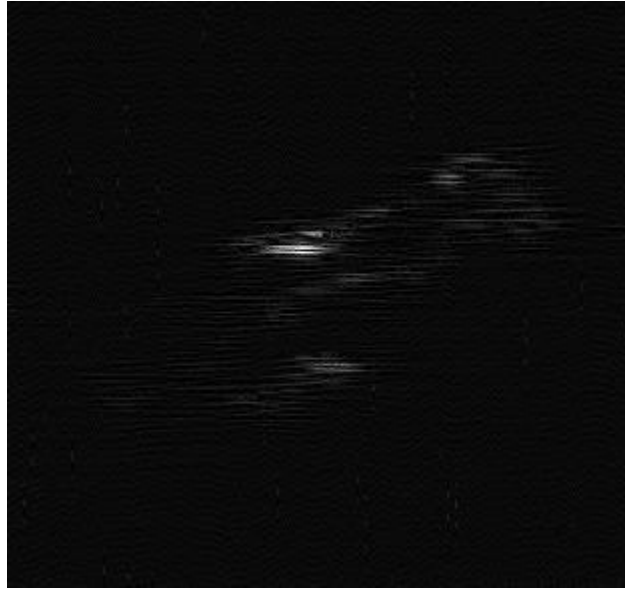


Figure 3.3. RF ultrasound signal after cropped.

Thus, raw data is opened and cropped selecting the ultrasound information in the main object region. Figure 3.4 shows example raw images: (a) 8 μm wire phantom, and (b) mouse aorta *in vitro*. Typically, ultrasound images are displayed in grayscale and the brightness of each pixel in the image is proportional to echo amplitude of the RF ultrasound signal (more details in Section 3.6). This step accentuates the region of interest (ROI) and improves the overall composition of the image by removing unwanted areas or irrelevant details from the ultrasound data.



(a) Wire phantom.



(b) APOE mouse aorta.

Figure 3.4. Ultrasound image of raw data.

As an initial step, raw images do not show the region of interest properly and attenuation may alter the image quality. Consequently, additional procedures are needed to improve the ultrasound images.

3.2. *Time Gain Compensation (TGC)*

The second processing step in the ultrasound imaging is the time gain compensation (TGC). TGC is applied to compensate the attenuation effect of ultrasound energy as it propagates through objects (biological tissues). As the name implies, TGC applies a varying gain function to the RF signal according to the penetration depth within the field of view (FOV). A variety of TGC curves, shown in Figure 3.5, can be used for the ultrasound operator, and in our custom designed ultrasound system any of these curves can be applied to the RF signals (Section 4.2.2).

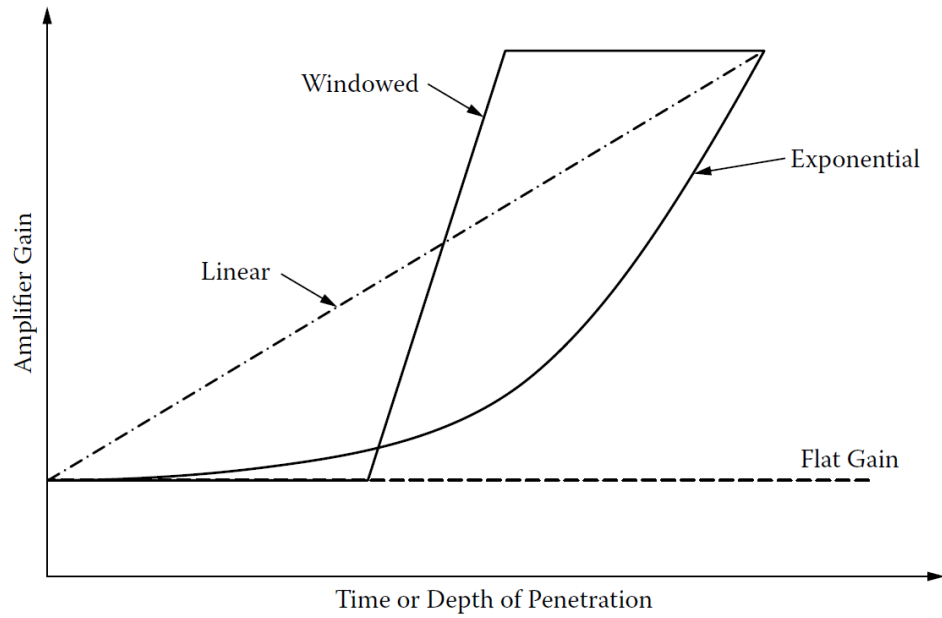


Figure 3.5. Time gain compensation curves frequently used in ultrasonic imaging [58].

Figure 3.6 shows an example of a linear TGC curve that was applied to the 8 μm wire phantom ultrasound data, where the gain increases linearly from 1 to 100 (0 to 40 dB). Figure 3.7 (a) and (b) shows the RF ultrasound signal before and after applying TGC for the wire phantom data, respectively. From these signals it can be seen that after TGC the signal has higher overall amplitude, but may include some amplified noise components, mostly at the end of the RF signal.

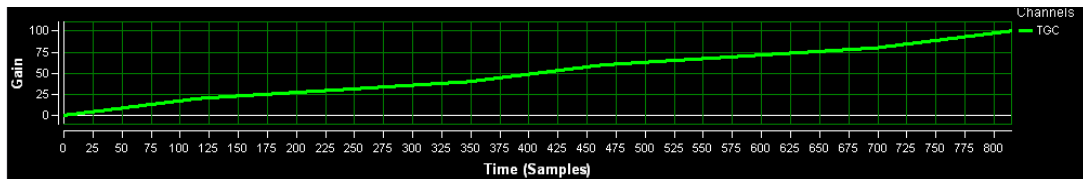
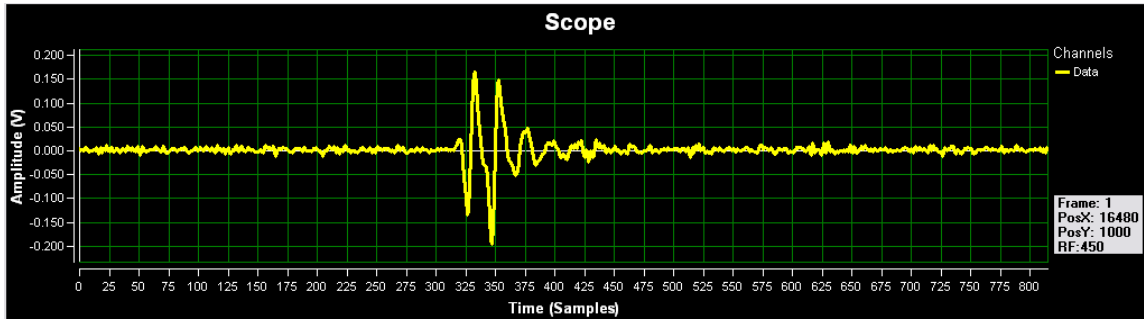
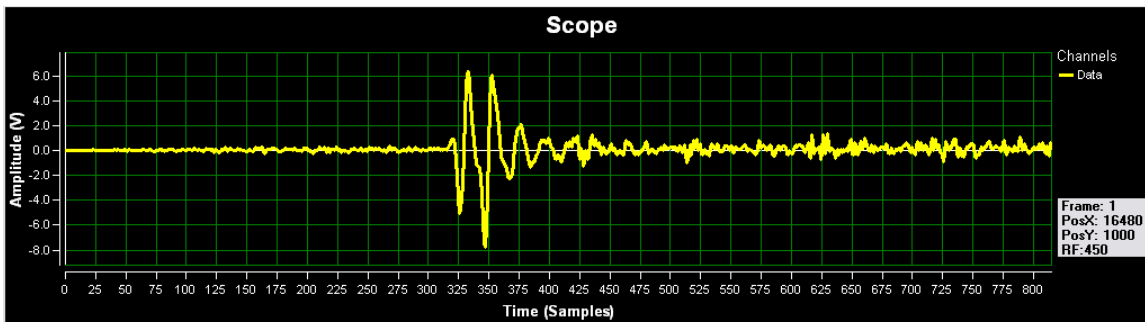


Figure 3.6. Time gain compensation curve used.



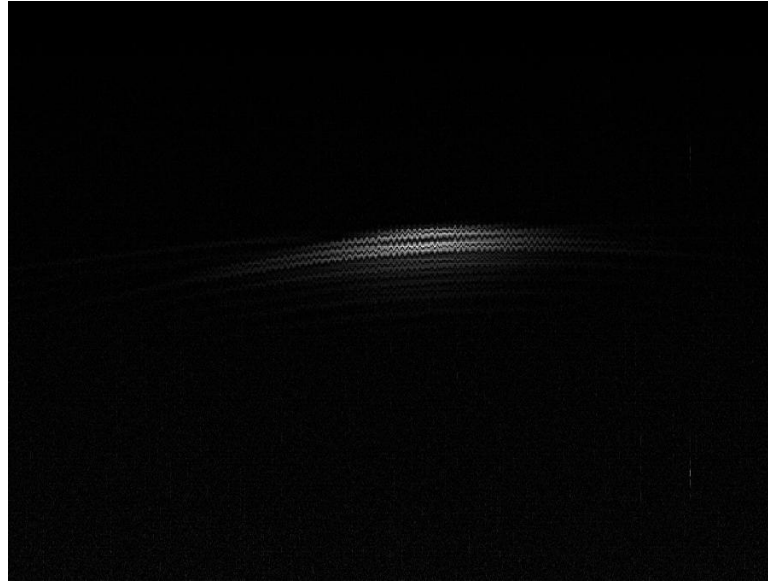
(a) RF ultrasound signal before TGC.



(b) RF ultrasound signal after TGC.

Figure 3.7. RF ultrasound signal during TGC.

Figure 3.8 shows an example of B-mode images after linear TGC is applied to the ultrasound data: (a) 8 μm wire phantom, and (b) mouse aorta. In this intermediate step of the high-resolution ultrasound image reconstruction procedure, the contrast of the ultrasound image has been improved making the ultrasound energy constant during all the tissue penetration and the energy attenuation had been corrected.



(a) Wire phantom.



(b) APOE mouse aorta.

Figure 3.8. Ultrasound image after time gain compensation (TGC).

3.3. Filtering

The compensated RF data is then filtered using a band pass filter in order to remove noise from the ultrasound data. The band pass filter implemented is a finite impulse response (FIR) filter using a Hamming window of length 41, where the low and high cutoff frequencies can be easily assigned (Section 4.2.3) depending on the transducer specifications and its center frequency. A band pass filter is a filter that allows signals between two specific frequencies to pass, and attenuates signals with frequencies outside this range. The amplitude response of an ideal band pass filter is flat from the center frequency down and up to the cutoff frequencies. The cutoff frequencies (low and high) are the points where the amplitude has decreased by 3 dB or 70.7% of its original amplitude. This is the pass band of the filter. The regions above the pass band to infinity, and below the pass band to zero are the stop bands of the filter. Figure 3.9 shows the specifications of a band pass filter, where F_s is the sampling frequency, F_{c1} the low cutoff frequency, and F_{c2} the high cutoff frequency.

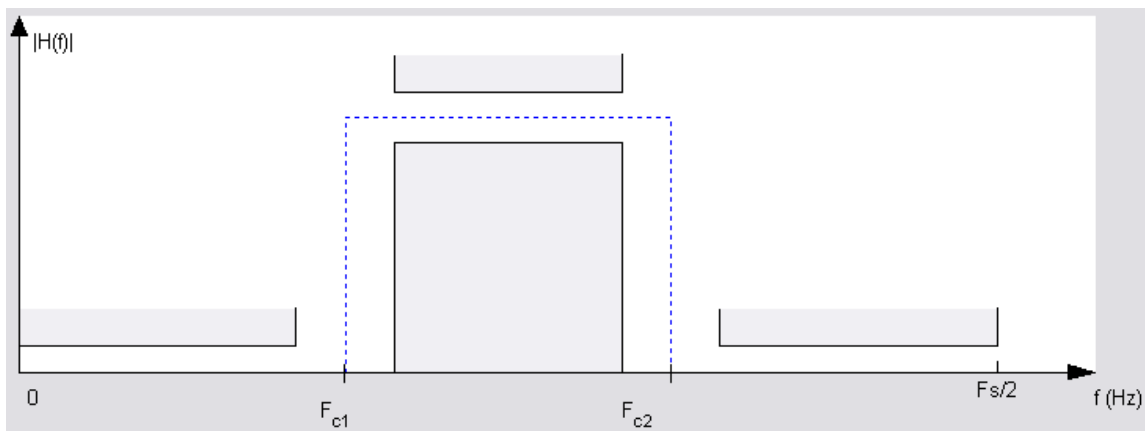


Figure 3.9. Band pass filter specifications.

The impulse response sequence $h(n)$ for a band pass FIR filter is defined as:

$$h(n) = \frac{1}{2\pi} \int_{-\pi}^{\pi} H(\omega) e^{j\omega n} d\omega, \quad 0 \leq n \leq N, \quad (3.1)$$

where $H(\omega)$ is the magnitude response of the desired filter. To create a finite-duration impulse response, this response is truncated applying a window. In this work a Hamming window was applied. The coefficients of a Hamming window are computed from the following equation [59]:

$$\omega(n) = 0.54 - 0.46 \cdot \cos\left(2\pi \frac{n}{N}\right), \quad 0 \leq n \leq N, \quad (3.2)$$

where the window length is $L = N + 1$. Figure 3.10 shows the time domain and frequency response for an example Hamming window with $N=64$.

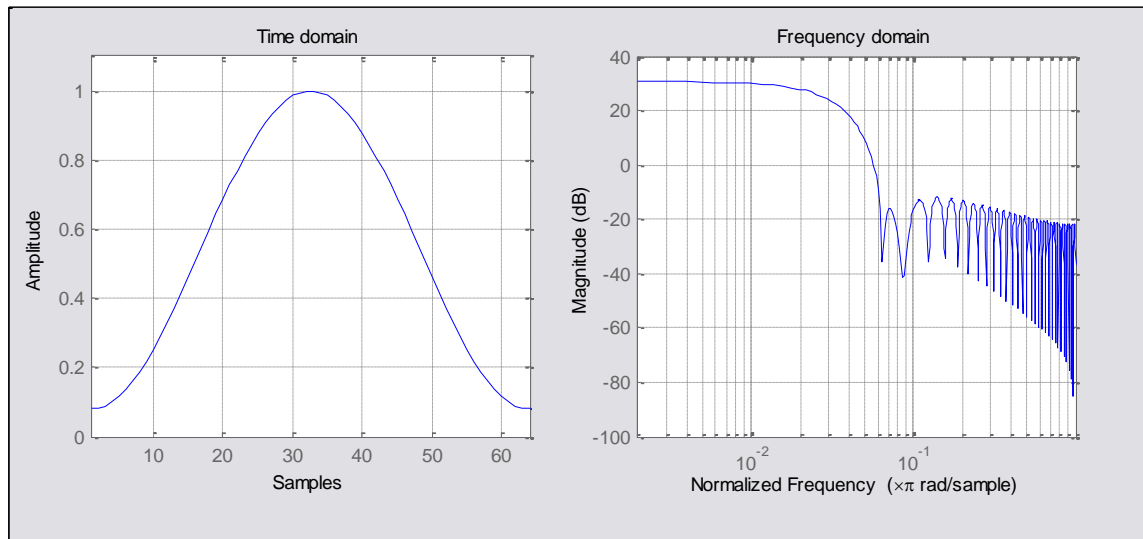


Figure 3.10. Hamming window with $N=64$.

The resulted impulse response $b(n)$ of the designed filter is the product:

$$b(n) = \omega(n) \cdot h(n), \quad 0 \leq n \leq N, \quad (3.3)$$

where multiplying in time domain corresponds to convolution in frequency domain.

Figure 3.11 shows the RF signals for the wire phantom data before and after band pass filtering, where the signal in yellow represents the ultrasound data after TGC and the signal in green corresponds to the signal after filtering. Figure 3.12 shows B-mode images after filtering of ultrasound data: (a) 8 μm wire phantom, and (b) mouse aorta. The low and high cutoff frequencies were 29.2 MHz and 81.2 MHz, respectively, that corresponds to a 94.2% bandwidth of the transducer. The same parameters were used for all the experiments, which is the 6 dB attenuation of the transducer (center frequency of 55.2 MHz, Section 4.1.6).

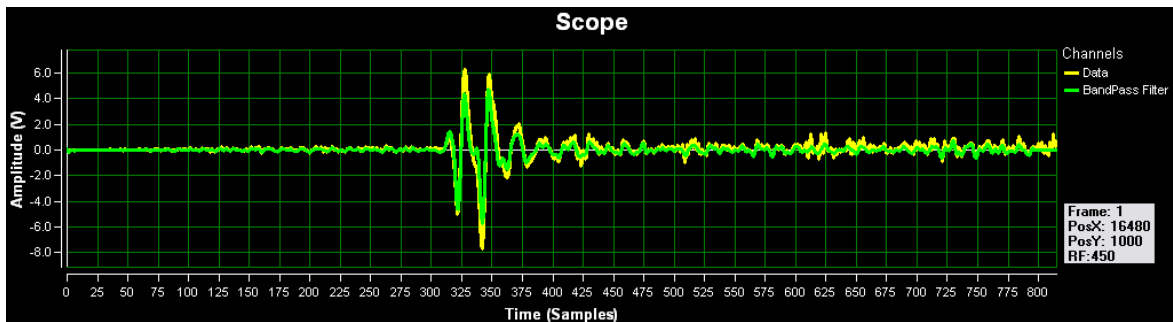
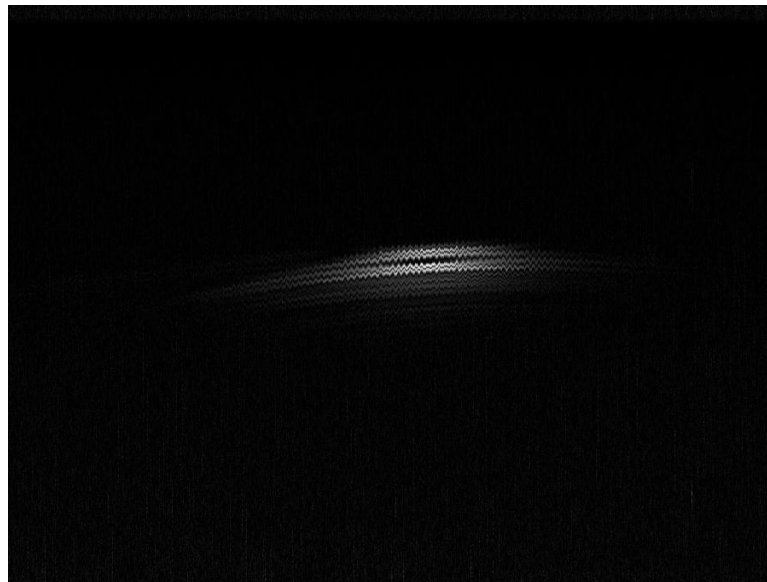
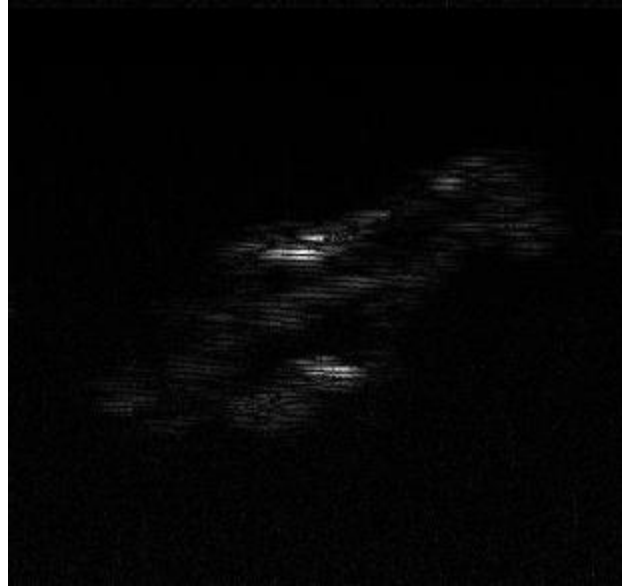


Figure 3.11. RF ultrasound signal during filtering.



(a) Wire phantom.

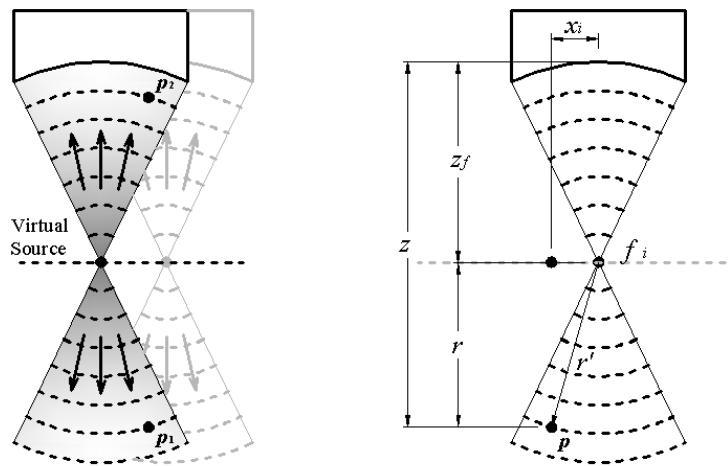


(b) APOE mouse aorta.

Figure 3.12. Ultrasound B-mode image after filtering.

3.4. Synthetic Aperture Focusing Technique (SAFT)

In order to overcome the problem of limited depth of field for a highly focused transducer [60] and to improve lateral resolution beyond the focus of the transducer [61] the weighted synthetic aperture focusing technique (SAFT) [60] is applied on the filtered RF signals. Figure 3.13 shows a sketch [62] illustrating the basic concepts of SAFT.



(a) Sketch for virtual-source concept. (b) Focusing geometry with a virtual source.

Figure 3.13. Synthetic aperture focusing technique (SAFT) sketch [62].

SAFT technique assumes the transducer's focal point as a virtual source, as shown in part (a) of Figure 3.13. This virtual source is considered to produce a wave propagating both forward and backward with respect to itself that is spherical within a certain angular extent. When a linear scan is performed with the transducer (Section 4.1.1), the sound field generated by the virtual source at the current position will overlap with the sound fields produced at adjacent positions. Hence, synthetic aperture focusing can be performed in the overlapping region before and after the virtual source. In Figure 3.13 (a) points p_1 and p_2 are in the overlapping region before and after the virtual source, and they can be synthetically focused using the received scan lines at which the points p_1 and p_2 are illuminated by the sound field. Figure 3.13 (b) shows the virtual-source concept where the scan line i is a distance x_i away from the axis of the synthesized beam. Since the sound field of a scan line i propagates through the desired focal point p , the echo signal from scan line i can be added to the beam constructively by applying an appropriate time delay. Based on the virtual-source concept, the time delay applied to the received signal of scan line i is expressed as:

$$\Delta t_i = 2 \cdot \text{sgn}(z - z_f) \cdot \frac{(r' - r)}{c}, \quad (3.4)$$

where z is the depth of the synthetic focal point p , z_f the transducer's focal depth, $r = \text{abs}(z - z_f)$ the axial distance from the transducer's focal depth to the synthetic focal depth, $r' = \sqrt{r^2 + x_i^2}$ the distance from the virtual source f_i to the synthetic focal point, c the speed of sound, and $\text{sgn}(\cdot)$ the signum function [61]. Note that if the synthetic focal point is located in front of the transducer's focal point, the time delay is negative. After appropriate delays relative to the virtual source are applied to all corresponding scan lines according to the above equation, weighted SAFT is implemented as the following sum:

$$A(t) = \sum_i w_i S_i(t - \Delta t_i), \quad (3.5)$$

where $A(t)$ is the computed RF echo return, and w_j is a weight assigned to the returned signal, $S(t)$, for scan line i . The number of signals included in the sum is determined by the aperture angle of the transducer beam beyond the transducer's focus. The beam spread of a source is determined by the geometry of the source and the wavelength of sound in the medium [60]. Both virtual and aperture focal points are adaptively changing based on the field of view (FOV) or the region of interest (ROI). The upper part of the FOV/ROI is placed near the transducer virtual focus, where the aperture focus is kept at the bottom.

SAFT parameters such as aperture size, synthetic focal point (z), and transducer focus (z_f) can be easily assigned in our system (Section 4.2.4) depending on the transducer specifications and the experimental setup. Figure 3.14 shows the RF ultrasound signal after SAFT technique is applied to the wire phantom data. Figure 3.15 shows an example of images after SAFT: (a) 8 μm wire phantom, and (b) mouse aorta. The same parameters were used for all figures and experiment examples. SAFT was applied with aperture size of 8, synthetic focal point of 12 mm, and transducer focus of 9.6 mm, which are specific parameters of the transducer used and the experiment setup.

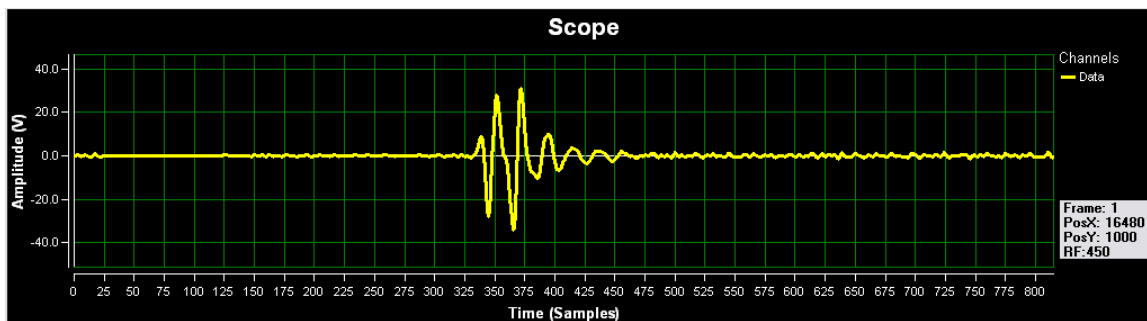
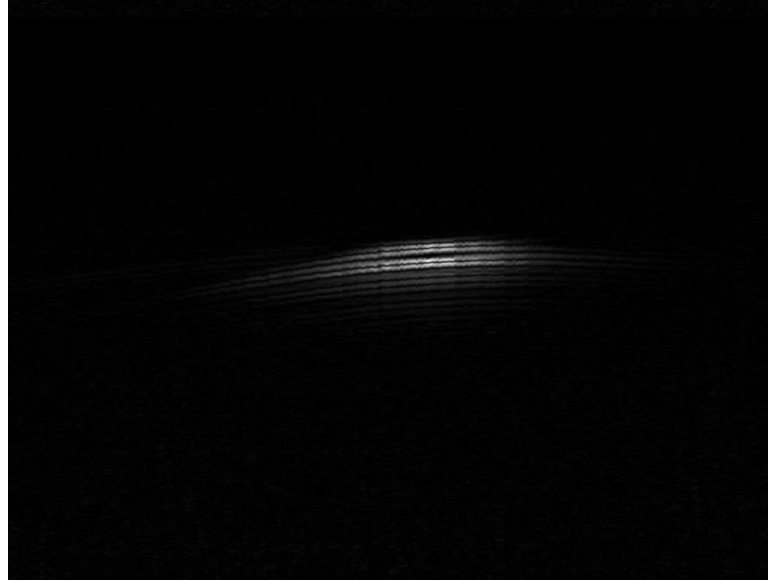
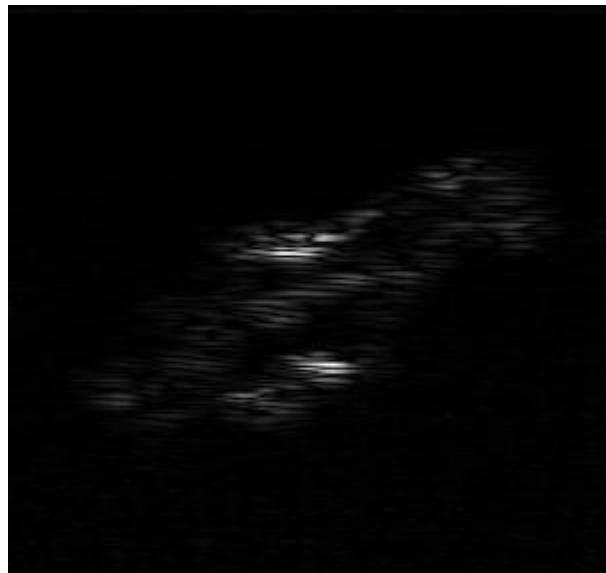


Figure 3.14. RF ultrasound signal after SAFT.



(a) Wire phantom.



(b) APOE mouse aorta.

Figure 3.15. Ultrasound image after SAFT focusing.

3.5. Envelope Detection (Hilbert Transform)

The next step used for the high-resolution ultrasound imaging is the envelope detection of the RF signals with Hilbert transform. Some algorithms for envelope detection [63] include: ideal Hilbert transformer, rectification of RF signal followed by filter, approximate Hilbert transformer, and quadrature demodulation. However, Hilbert transform (HT) and a subsequent computation of the magnitude gives the ideal RF signal envelope [64]. Figure 3.16 shows a comparison between the more important techniques for envelope detection in ultrasound imaging.

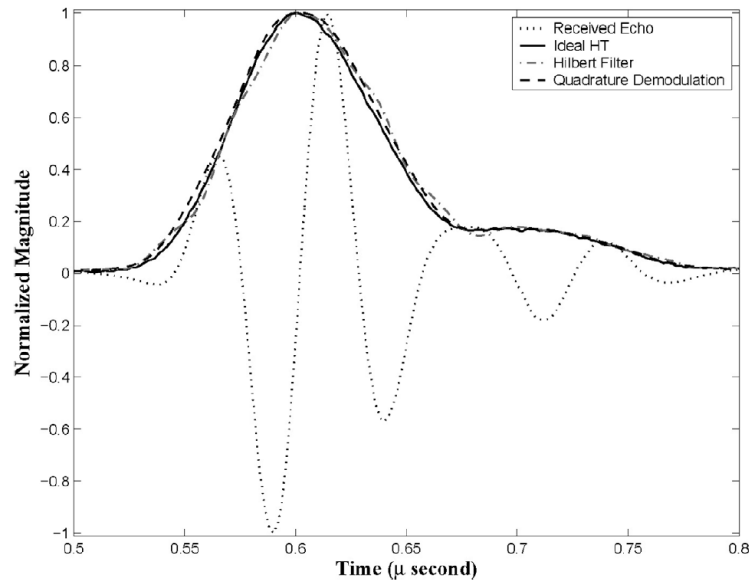


Figure 3.16. Comparison of envelope detection techniques [63].

For high-resolution ultrasound signals the envelope detection is ideally computed using the Hilbert Transform (HT) followed by the magnitude of the resulting complex representation of the RF data [65]. This envelope detector is referred as the ideal envelope detector (IED). The Hilbert Transform rotates all frequency components of the signals by 90 degrees $\left(\frac{\pi}{2}\right)$, and it is defined as:

$$r_{HT}(t) = r(t) * \frac{1}{\pi t}, \quad (3.6)$$

$$r_{HT}(t) = \int_{-\infty}^{\infty} \frac{r(u)}{\pi(t-u)} dt, \quad (3.7)$$

where $r(t)$ is the received echo signal, $*$ represents convolution, and $r_{HT}(t)$ is the Hilbert transform. Then, Hilbert transform $r_{HT}(t)$ is used as the imaginary term in the complex representation signal $r_c(t)$:

$$r_c(t) = r(t) + jr_{HT}(t), \quad (3.8)$$

Finally, the ideal envelope $E_{IDE}(t)$ is obtained by computing the magnitude of the complex representation signal $r_c(t)$:

$$E_{IED}(t) = \sqrt{r(t)^2 + r_H(t)^2}, \quad (3.9)$$

Figure 3.17 show the RF signals before and after IED for the wire phantom data, where the signal in yellow represents the ultrasound data after SAFT and the signal in green corresponds to their ideal envelope detector. Figure 3.18 shows an example of B-mode images after envelope detection with Hilbert transform is applied to ultrasound data: (a) 8 μm wire phantom, and (b) mouse aorta.

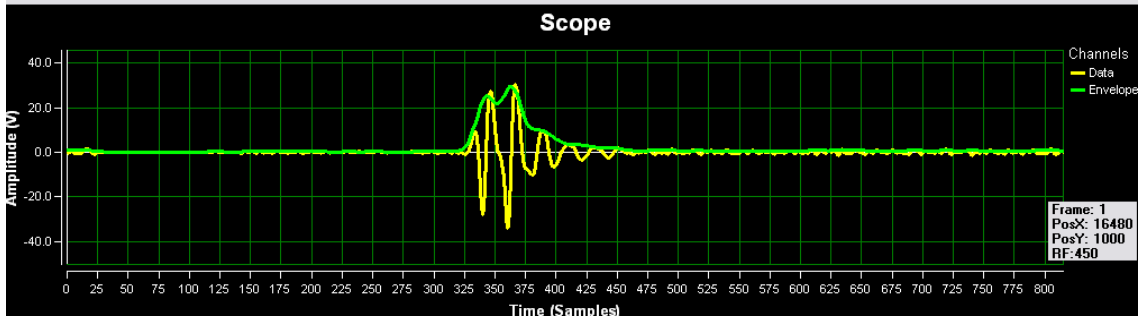
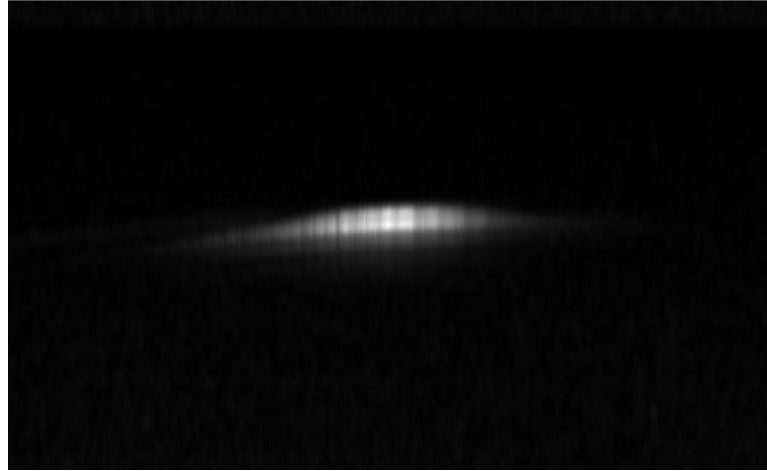
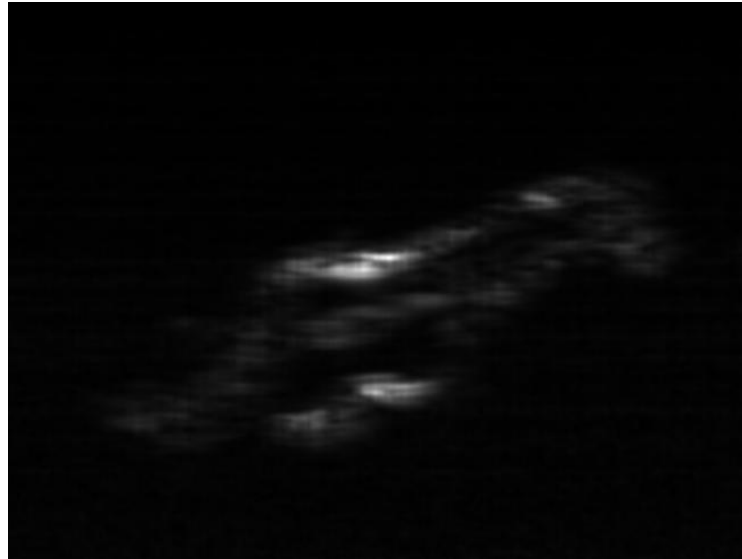


Figure 3.17. RF ultrasound signal during envelope detection.



(a) Wire phantom.



(b) APOE mouse aorta.

Figure 3.18. Ultrasound image after envelope detection with Hilbert transform.

3.6. *Logarithmic Compression*

Logarithmic compression is then applied to reduce the dynamic range of the RF signal for visualization, finalizing the high-resolution ultrasound image reconstruction procedure. Figure 3.19 shows an example of how the dynamic range of input signals is usually reduced, using only the stages of the time gain compensation (TGC) (reduction by approximately 60 dB) and the logarithmic compression to match the 20 dB capability

of a grayscale display. Example dB values correspond to a typical region being viewed for an adult human heart to a depth of 15 cm [8].

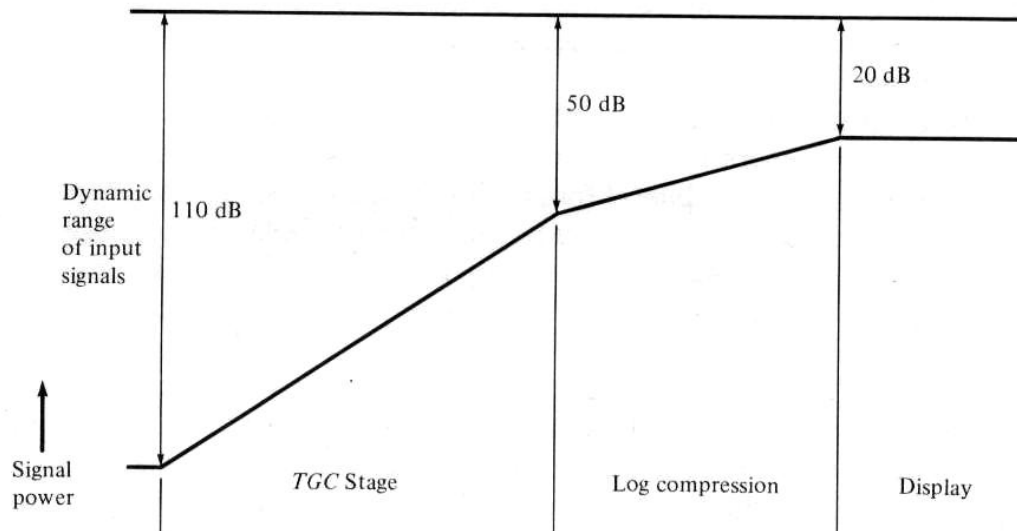


Figure 3.19. Example of dynamic range of the RF signals until display [8].

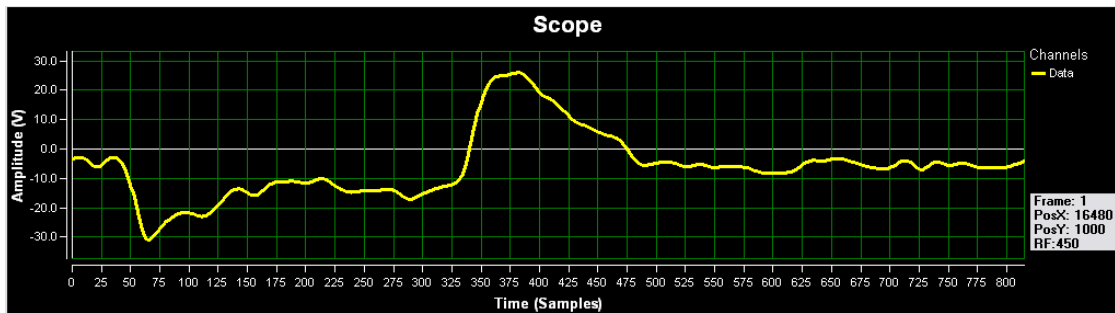
Grayscale representation of RF strengths allows an easier ultrasound data interpretation, however, the dynamic range of a typical grayscale display is limited to about 20 dB. On the other hand, the range of RF strengths, from strongest to weakest, from a typical view is about 110 dB. The strongest RF is limited to the amount of power that can be generated in the transmit pulse (Section 4.1.1), while the weakest RF is determined by the noise levels in the receiver system (typically some microvolts). For example in Figure 3.19, the 110 dB of input dynamic range will be reduced by an amount of approximately 60 dB by the action of TGC stage. This leaves a dynamic range of 50 dB which is compressed to be adequately displayed within the 20 dB dynamic range of a grayscale image, which is accomplished by the logarithmic compression technique. Nevertheless, depending on the experiments and tissue samples other dynamic ranges can be used, making the ultrasound display image before the grayscale mapping wider around 20 dB, for example of 30, 35, or 45 dB.

Logarithmic compression technique changes the reflected signal magnitude from voltage (V) to decibels (dB), eliminating small amplitude voltage pulses. The commonly used decibel scale is defined as:

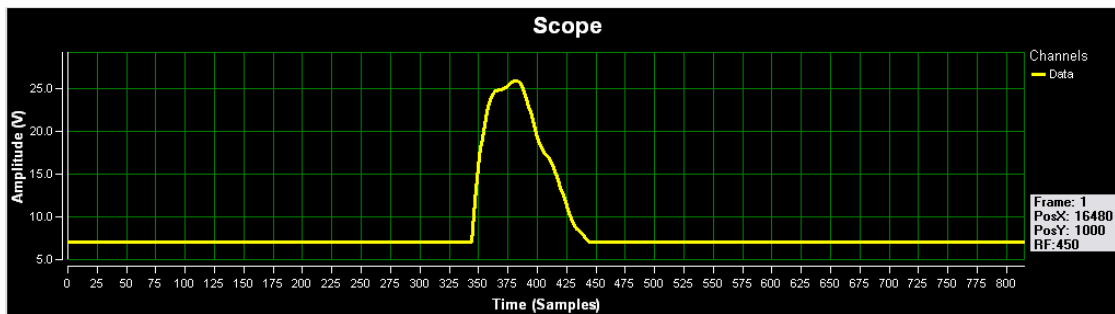
$$dB = 20\text{Log}_{10}(p), \quad (3.10)$$

where dB is the decibel measure of the pressure signal p , also known as RF ultrasound signal.

After logarithmic compression is applied to the ultrasound data this is improved through thresholding. Logarithmic compression parameters such as minimum and maximum RF amplitude (dynamic range) can be easily assigned in our system (Section 4.2.6) providing a great deal of visualization flexibility to the ultrasound operator. Figure 3.20 shows the RF ultrasound signals during logarithmic compression for the 8 μm wire phantom ultrasound data: (a) after the logarithmic compression is applied, and (b) after thresholding the data previously to visualization. In this case the dynamic range was 20 dB, with minimum threshold of 10 dB and maximum RF amplitude of 30 dB.



(a) RF ultrasound signal after logarithmic compression.



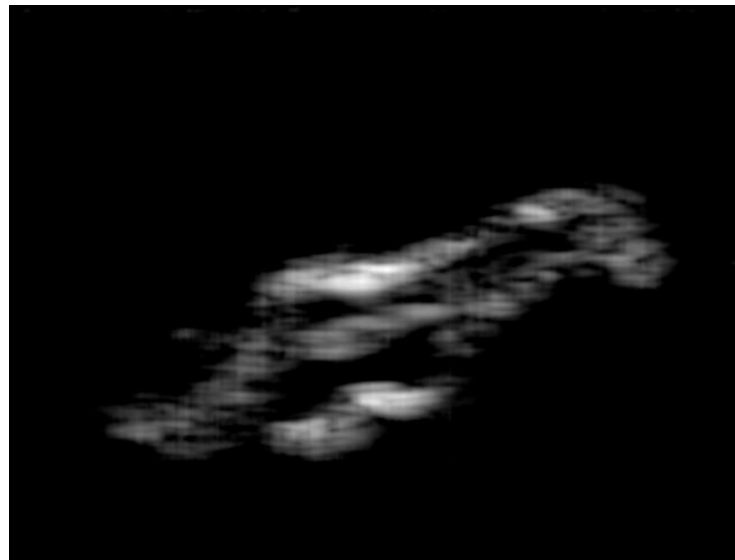
(b) RF ultrasound signal after logarithmic compression and thresholding.

Figure 3.20. RF ultrasound signal during logarithmic compression.

Figure 3.21 shows final B-mode images after the ultrasound reconstruction procedure: (a) 8 μm wire phantom, and (b) mouse aorta, where the dynamic range was assigned as 20 dB and 30 dB respectively.



(a) Wire phantom.



(b) APOE mouse aorta.

Figure 3.21. Final ultrasound image after logarithmic compression.

3.7. Spatial Resolution Assessment

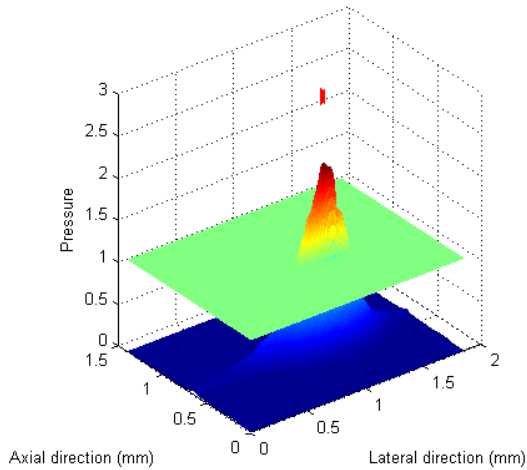
The spatial resolution assessed with our system (Section 4.1.1) depends on the transducer used. The transducer mainly used for this study was a 55.2 MHz spherically focused transducer, explained in detail at Section 4.1.6. The theoretical axial resolution (R_{ax}) and lateral resolution (R_{lat}) of a focused ultrasound transducer can be expressed by the following equations [15, 26]:

$$R_{ax} = \frac{1}{2} \cdot \frac{c}{BW}, \quad (3.11)$$

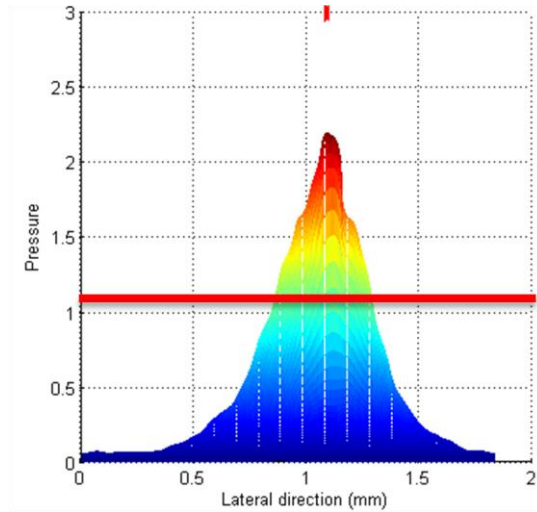
$$R_{lat} = \frac{c}{f_c} \cdot \frac{FD}{A}, \quad (3.12)$$

where c is the speed of sound (1540 m/s in water), BW is the transducer bandwidth (52 MHz, 94.2% BW of the transducer), f_c is the transducer center frequency (55.2 MHz), FD is the transducer focal distance (10.64 mm), and A is the transducer's element diameter (3.17 mm). Also, lateral resolution can be calculated using the wavelength λ at the central frequency as $\frac{c}{f_c} = \lambda$. According to the previous equations, the theoretical axial and lateral resolutions achieved using this transducer are 14.8 μm and 93.6 μm , respectively.

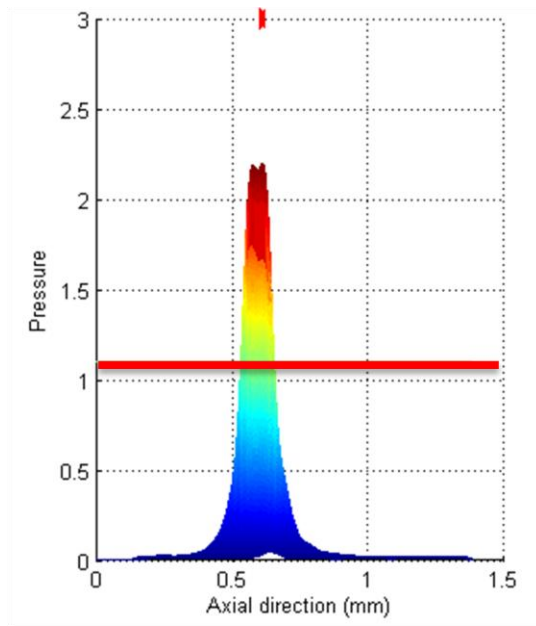
The experimental spatial resolutions were obtained from a cross-sectional scan of an 8 μm (diameter) tungsten wire placed in water at the transducer focal point after each technique in the high-resolution ultrasound image reconstruction procedure. The experimental axial and lateral resolutions are typically measured as the dimensions of -6 dB pressure distribution with respect to the peak amplitude [15, 26]. Figure 3.22 shows an example of the calculation of the axial and lateral resolution from ultrasound B-mode images using arbitrary example data.



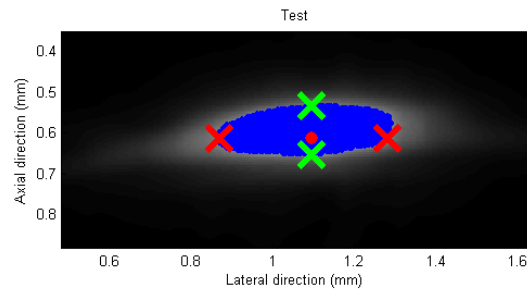
(a) 3D view of ultrasound pressure field with a -6 dB plane superimposed. Red point in the top is showing the location of the maximum pressure value.



(b) Lateral resolution of $410.2 \mu\text{m}$ was measured as the distance between the intersection of the -6dB plane with the pressure curve.



(c) Axial resolution of $120.4 \mu\text{m}$ was measured as the distance between the intersection of the -6dB plane with the pressure curve.



(d) B-Mode image showing region of pressure amplitudes above -6 dB highlighted in blue. Red point is the maximum pressure value. Red marks are the lateral resolution, and green marks the axial resolution.

Figure 3.22. Experimental calculation of spatial resolutions for ultrasound images.

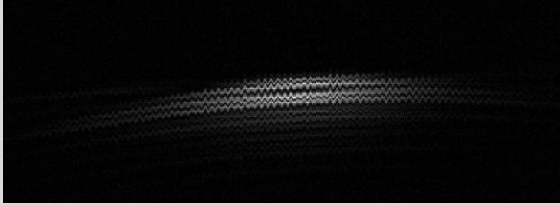
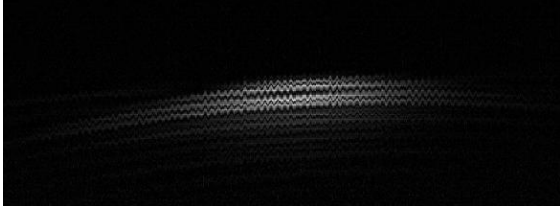
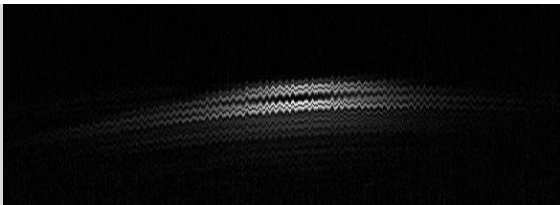
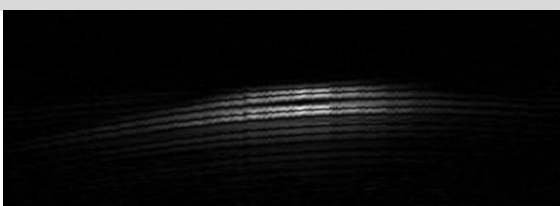
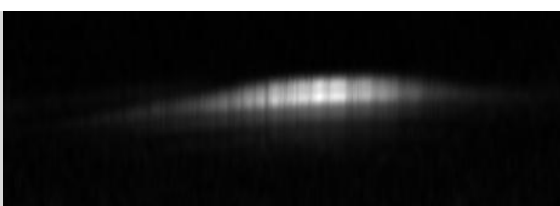
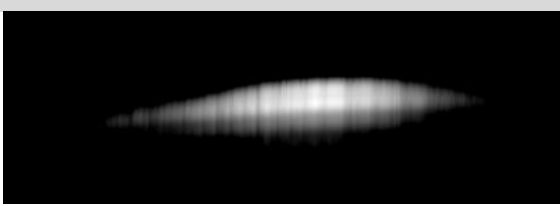
Arbitrary example data.

In Figure 3.22 ultrasound data is represented as a 3D pressure amplitude views and as a B-mode image in order to measure the axial and lateral resolutions: (a) is a 3D view of the pressure data with a cross section plane at -6 dB or half of the maximum pressure amplitude, (b) is the lateral pressure view showing a red line at -6 dB, (c) is the axial pressure view showing a red line at -6 dB, and (d) is the B-mode image where the blue area indicates values above -6 dB, the red point is the maximum pressure value, the red marks are the axial resolution, and the green marks are the lateral resolution. For this arbitrary example data the axial and lateral resolutions were measured as 120.4 μm , and 410.2 μm , respectively.

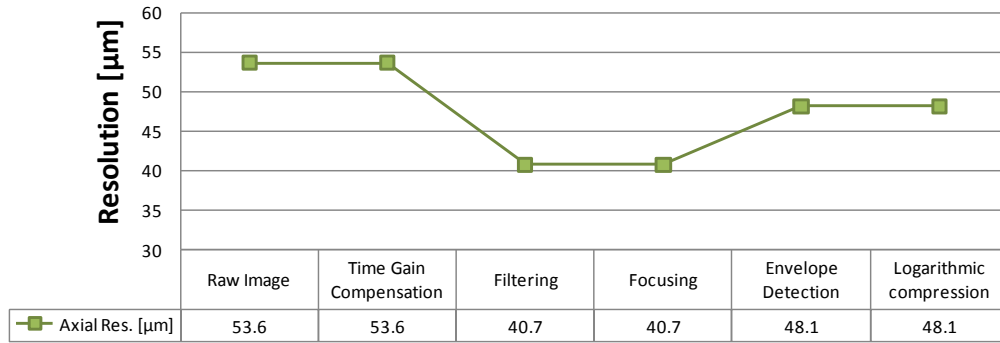
Table 3.1 shows a summary of the experimental spatial resolutions obtained from the 8 μm tungsten wire phantom immersed in water after each processing step to reconstruct the high-resolution ultrasound image. In order to allow an easy analysis of the changes in the resolution during the imaging procedure, the resolutions reported in Table 3.1 are plotted in Figure 3.23 versus the processing steps.

The theoretical resolution values are typically compared with the experimental measure after the step of weighted SAFT focusing, that where found as 40.7 and 151.2 μm for the axial and lateral resolutions respectively at -6 dB. The experimental spatial resolution showed a good agreement with the theoretical values described earlier. However laterally, one major cause of the difference is the small spatial shift of the wire out of the transducer focus, 10.64 mm during the experiment, which causes the wire elongation. Axially, the difference is reasonable and expected due to the 8 μm wire diameter.

Table 3.1. Ultrasound resolution measured at the different processing steps

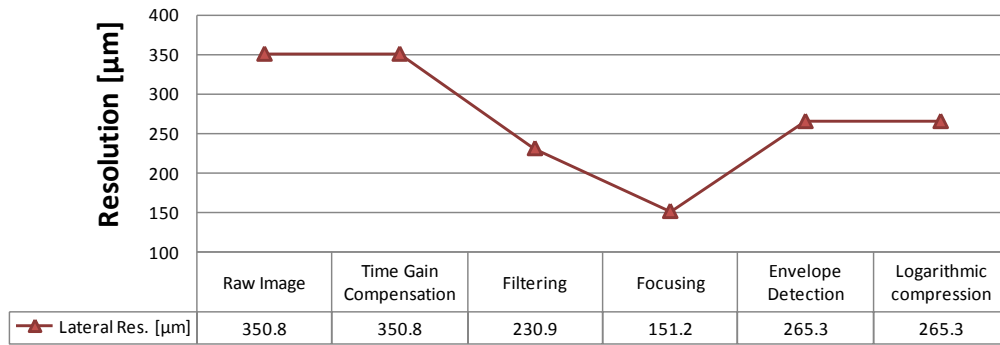
#	Steps	<i>B-Mode Ultrasound Image</i>	<i>Axial Res. [μm]</i>	<i>Lateral Res. [μm]</i>
1	Raw Image		53.6	350.8
2	Time Gain Compensation		53.6	350.8
3	Filtering		40.7	230.9
4	Focusing		40.7	151.2
5	Envelope Detection		48.1	265.3
6	Logarithmic compression		48.1	265.3

Ultrasound Axial Resolution Assessed by Step



(a) Axial resolution.

Ultrasound Lateral Resolution Assessed by Step



(b) Lateral resolution.

Figure 3.23. Ultrasound resolution assessed by processing step.

- CHAPTER 4 -

GRAPHICAL USER INTERFACES (GUIs) FOR HIGH-RESOLUTION ULTRASOUND ACQUISITION AND HIGH-RESOLUTION ULTRASOUND IMAGING

Two custom user-friendly computer graphical user interfaces (GUIs) are developed in order to enhance the efficiency and to allow an easy interaction with all the electronic devices of the high-resolution ultrasound system. One GUI is developed for high-resolution ultrasound control and acquisition (Section 4.1) and another GUI for high-resolution ultrasound imaging (Section 4.2). The GUIs and all the electronic device's interactions and ultrasound imaging techniques are developed using Microsoft Visual C++ programming language (Microsoft Corp., Redmond, WA). In addition, all the widgets components in the GUIs are implemented using Windows Forms version 2.0.0.0 that is the graphical application programming interface (API) included as a part of Microsoft .NET Framework (Microsoft Corp., Redmond, WA). The development of these GUIs allows a real-time high-resolution ultrasound imaging system using a single element transducer.

This chapter will describe the high-resolution ultrasound acquisition and imaging GUIs in detail, as well as the system specifications and the high-resolution ultrasound transducer used. Finally, it will describe how the sequence of B-mode images for a 3D reconstruction is created using the ultrasound imaging GUI.

4.1. High-Resolution Ultrasound Acquisition System GUI

The high-resolution ultrasound acquisition system GUI developed in Visual C++ is shown in Figure 4.1. It allows the selection of the acquisition axis or axes modalities, the acquisition A/D cards parameters, the motion controller parameters, and the experiment scan specification parameters, all with an easier and faster interaction. Also, it allows the RF signal visualization and to see the actual position of the system at any moment. The development of this GUI allows an easy high-resolution ultrasound

acquisition to any user with basic knowledge in ultrasound and with only minimum and faster training in the system and the acquisition GUI. This capability opens the system to any researcher or person interested in performing experimentations with high-resolution ultrasound.

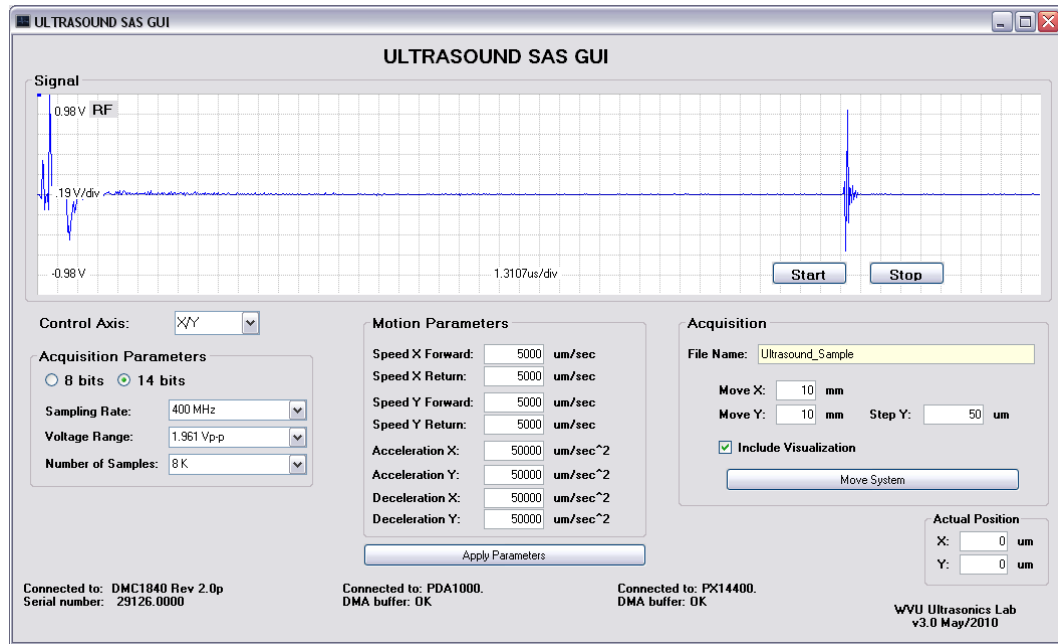


Figure 4.1. High-resolution ultrasound acquisition system GUI.

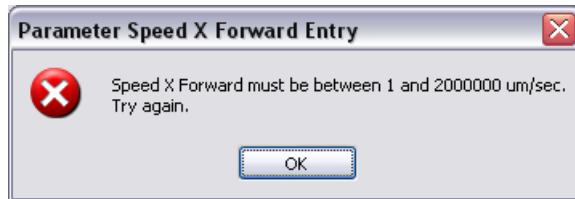
The high-resolution ultrasound acquisition system GUI should be used after all the electronic devices of the system are synchronized and ready to use. In addition, the ultrasound transducer should be connected to the system and placed in the starting position for the ultrasound scan of the sample. However, the acquisition GUI checks all of the electronic devices and prevents the user from performing a malfunction in the system or from selecting a non-valid parameter. Some of these preventions are shown in Figure 4.2.



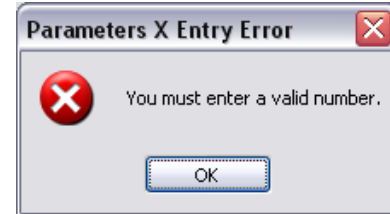
(a) Motion card not detected



(b) D/A acquisition card not detected



(c) Parameter out of valid range



(d) Parameter not valid

Figure 4.2. Some mal-function protections in the ultrasound acquisition GUI.

4.1.1. System Description

The block diagram shown in Figure 4.3 explains the main components of the high-frequency ultrasound imaging system [56, 62]. The ultrasound transducer uses a signal of negative impulse type as the excitation signal. The general purpose ultrasonic pulser-receiver (Model 5900PR, Olympus NDT Inc., Waltham, MA, USA) generates and amplifies this excitation signal. The impulse has 175 Volts amplitude and rise-time of 2 ns with no-load at the transmitter output. These specifications allow using our system with ultrasound transducers in the range of 30 to 120 MHz frequencies. The IEEE-488 (GPIB) standard interface could be used to control and communicate with the ultrasonic pulser-receiver. The excitation signal is synchronized with the data acquisition trigger input using a common signal generated by a computer controlled function generator with 1 GHz sampling rate and 14 bit amplitude resolution (Model AFG3102, Tektronix Inc., Beaverton, OR, USA). The ultrasound transducer is used as both ultrasound transmitter and receiver and is connected to the transmit/receive port of the ultrasound pulser-receiver, which is operated in the pulse-echo mode.

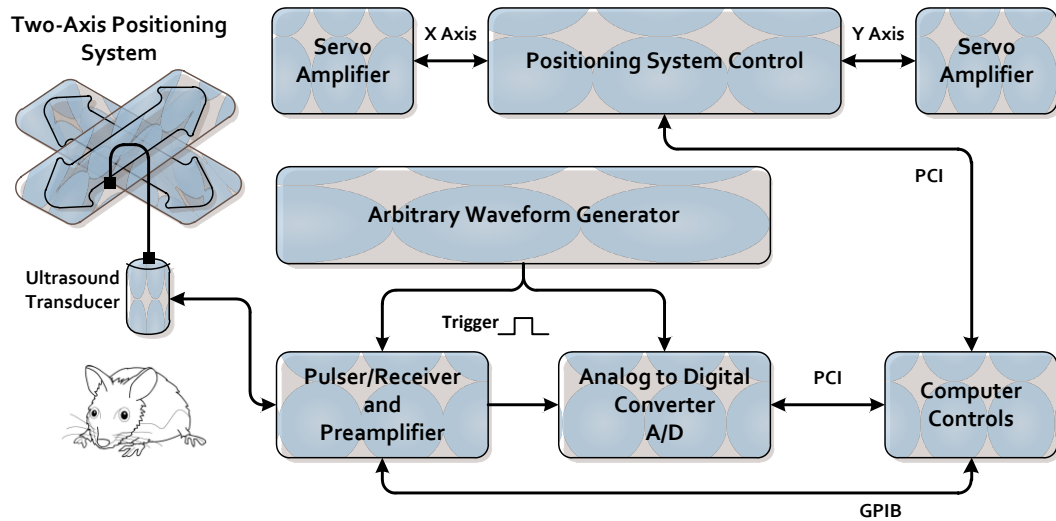


Figure 4.3. Block diagram of the high-resolution ultrasound system.

The system can be integrated with several single element ultrasound transducers. Nevertheless, only one ultrasound transducer of 55.2 MHz in center frequency was used (Olympus NDT Inc., Waltham, MA, USA). The technical specifications of this transducer are explained in detail in Section 4.1.6. The single-element transducers are used to convert the electrical energy into acoustical energy and vice versa. Ultrasound waves reflected from the field of view are received by the ultrasound transducer forming the desired echo. This echo signal is then amplified and filtered by the ultrasonic pulser-receiver. Filtered and amplified signals are fed to one of the two high-speed waveform digitizers which are synchronized with the excitation signal. The system allows high-speed waveform digitization using a PDA1000 data acquisition board (1 GHz maximum sampling rate, 8 bits resolution) or a PX14400 data acquisition board (400 MHz maximum sampling rate, 14 bits resolution) (Signatec Inc., Newport Beach, CA, USA). The system uses a high performance PC based system for system control, synchronization, and for further signal processing steps. The PC controls a two-axis (two translational) precision positioning system with 1 μm resolution (Danaher Corp., Washington, DC, USA).

The positioning system consists of two stages (X and Y axis) that can provide high speeds up to 2.5 m/s . For this, the system uses a linear motor, a linear encoder, and

recirculating bearings. The electronics for the positioning system uses a motion controller card (Galil Motion Control Inc., Rocklin, CA, USA). The stages are powered by a pair of servo amplifiers (Model Servostar CD, Danaher Corp., Washington, DC, USA). The positioning system control is controlled by the PC via the PCI port. The positioning system is synchronized with the data acquisition to collect the ultrasound signals continuously *on the fly* during the transducer movement down to 8.5 μm apart. The lateral resolution of the B-mode image is affected by the transducer movement spacing. The received RF signals are digitized and saved with sampling rates up to 1 GHz (8 bit resolution) or 400 MHz (14 bit resolution) using the high-speed data acquisition boards (Signatec Inc., Newport Beach, CA, USA). To avoid aliasing errors the sampling frequencies have been selected based on the Nyquist-Shannon sampling theorem (sampling rate $\geq 2 \times$ transducer frequency). The high-speed data acquisition boards are fully controlled with the main PC via PCI buses. Most of the system components are placed and bolted on a custom designed anti-vibration table to minimize motion errors and to assure accurate acquisition. The custom user-friendly computer graphical user interface (GUI) was designed using Microsoft Visual C++ (Microsoft Corp., Redmond, WA) to control both the data acquisition boards and the positioning system. Raw RF signals are collected from the field of view (FOV) during the transducer movement. These signals are saved sequentially according to the lateral location for further post processing. The data is then transferred to the high-resolution ultrasound imaging system GUI (Section 4.2) for post processing and image reconstruction.

4.1.2. Acquisition Modalities

The acquisition GUI allows four scanning modalities in the system, two single linear acquisition modalities (through X axis or Y axis) and two 3D acquisition modalities (through X/Y axes or Y/X axes). As the acquisition GUI is loading it checks and reports if all the electronic devices are working well, and then it allows the selection of the acquisition modalities. Figure 4.4 shows the acquisition GUI after it has loaded and finished checking the electronic devices. Figure 4.5 shows how the acquisition

modalities can be selected from a menu using the high-resolution ultrasound acquisition system GUI.



Figure 4.4. High-resolution ultrasound acquisition system GUI after loaded.

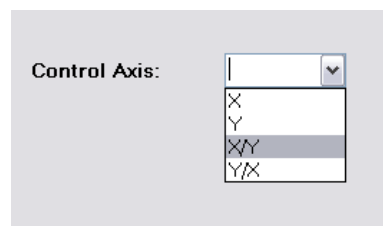


Figure 4.5. Acquisition modalities using the acquisition GUI.

After the acquisition modality is selected, the GUI activates the GUI sections for selecting the acquisition A/D card parameters and to define the motion controller parameters, as well as the RF signal visualization. Figure 4.6 shows the acquisition system GUI after selecting the acquisition modality X/Y.

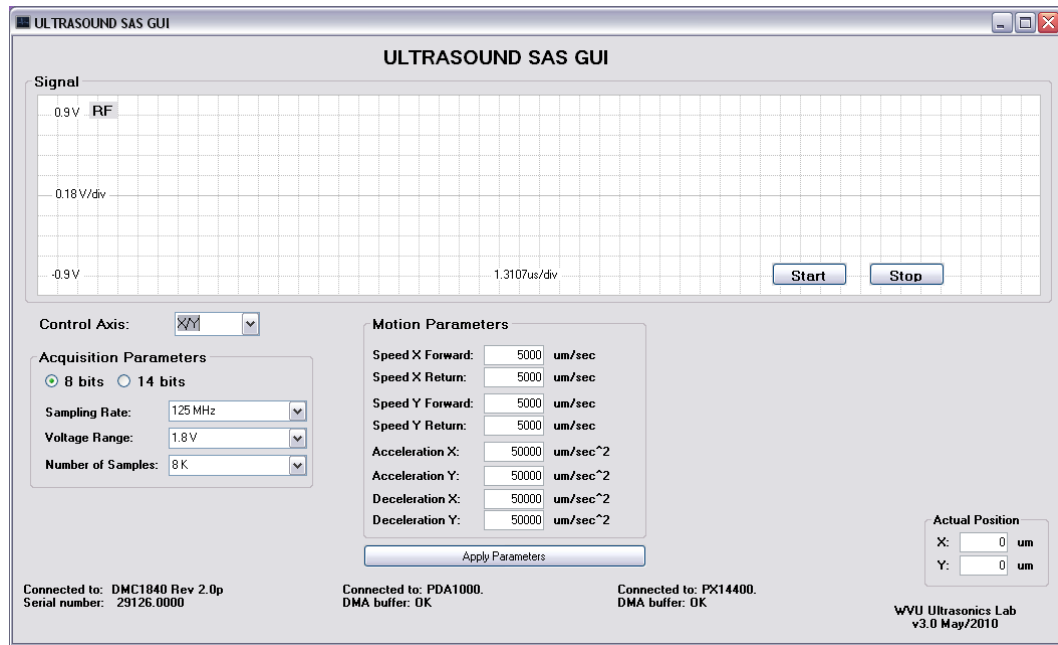
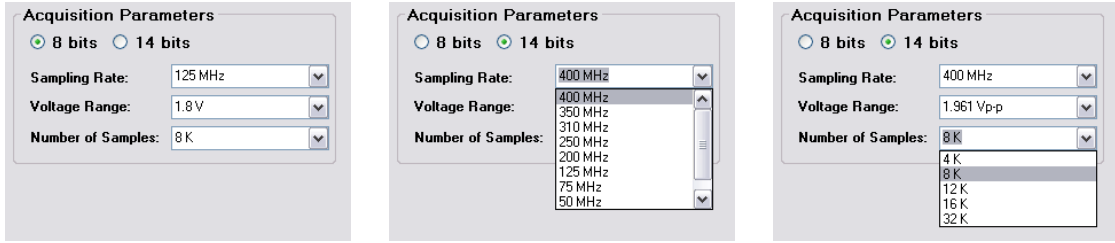


Figure 4.6. High-resolution ultrasound acquisition system GUI after selecting the acquisition modality X/Y.

4.1.3. Acquisition Cards Parameters

The acquisition parameters section in the GUI allows the user to select between the two high-speed waveform digitizer cards. The system allows high-speed waveform digitization using a PDA1000 data acquisition board (1 GHz maximum sampling rate, 8 bits resolution) or a PX14400 data acquisition board (400 MHz maximum sampling rate, 14 bits resolution) (Signatec Inc., Newport Beach, CA, USA). The main parameters for both A/D cards are sampling rate, voltage range, and number of samples. The values for these parameters are different depending on each A/D board, but the acquisition GUI automatically updates the selection menus with the right values after selecting the 8 bit or 14 bit card. Figure 4.7 shows the selection of the acquisition parameters using the high-resolution ultrasound acquisition system GUI.



(a) Acquisition parameters for the A/D cards (b) Sampling rate menu for the 14 bits card (c) Number of sample menu for the 14 bits card

Figure 4.7. Acquisition parameters using the acquisition GUI.

After the acquisition parameters are selected in the GUI the actual RF signal can be visualized in the acquisition GUI. The RF signal visualization can be activated or deactivated using the buttons of “Start” and “Stop” respectively, as shown in Figure 4.8.

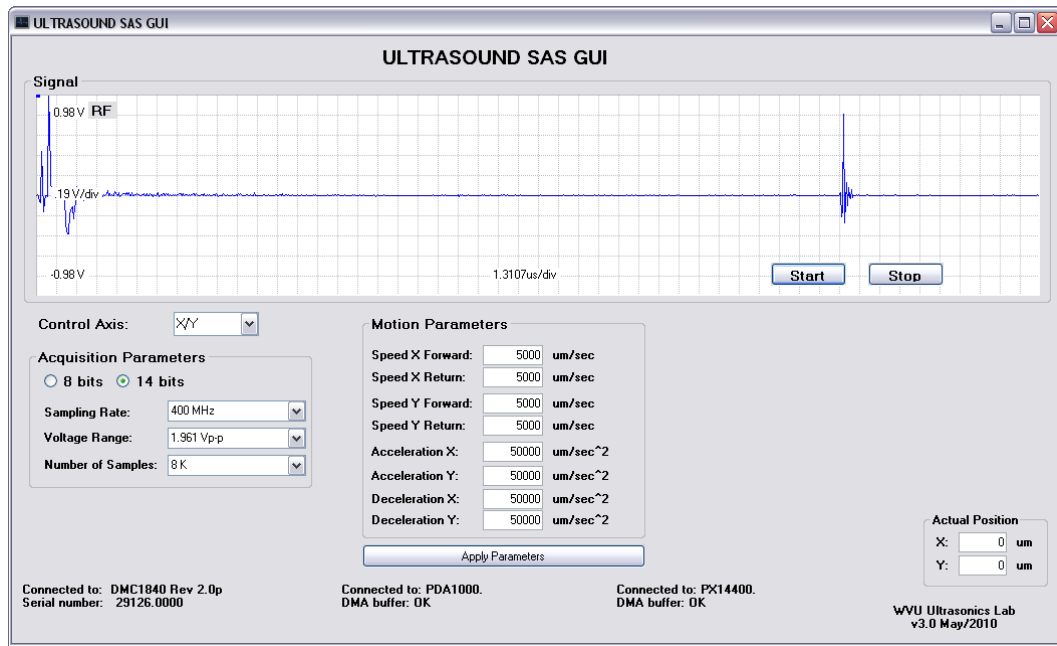


Figure 4.8. High-resolution ultrasound acquisition system GUI after activating the RF visualization.

4.1.4. Motion Controller Parameters

The acquisition GUI controls the two-axis (two translational) precision positioning system that has 1 μm resolution (Danaher Corp., Washington, DC, USA). The positioning system consists of XY stages that can provide high speeds up to 2.5 m/s combined with good accuracy and repeatability. To control the motion and positioning of the system, the GUI interacts with a PCI motion controller card (Galil Motion Control Inc., Rocklin, CA, USA). Depending on the acquisition modality (X or Y axis for a single scanning, X/Y or Y/X for a 3D scanning) the GUI activates only the necessary motion parameters for that axis or those axes. The motion parameters of the system are the speed forward and backward for each axis, as well as the acceleration and deceleration as shown in Fig. 4.9. All these parameters are submitted to the motion system after clicking the “Apply Parameters” button in the acquisition GUI. Figure 4.9 shows the motion parameters section in the high-resolution ultrasound acquisition system GUI for a 3D scanning (X/Y or Y/X axes).

Motion Parameters		
Speed X Forward:	5000	um/sec
Speed X Return:	5000	um/sec
Speed Y Forward:	5000	um/sec
Speed Y Return:	5000	um/sec
Acceleration X:	50000	um/sec ²
Acceleration Y:	50000	um/sec ²
Deceleration X:	50000	um/sec ²
Deceleration Y:	50000	um/sec ²

Apply Parameters

Figure 4.9. Motion controller parameters using the acquisition GUI.

After the motion parameters are submitted, the GUI activates the GUI section for defining the experiment specifications parameters. Figure 4.10 shows the high-resolution ultrasound acquisition system GUI after applying the motion parameters.

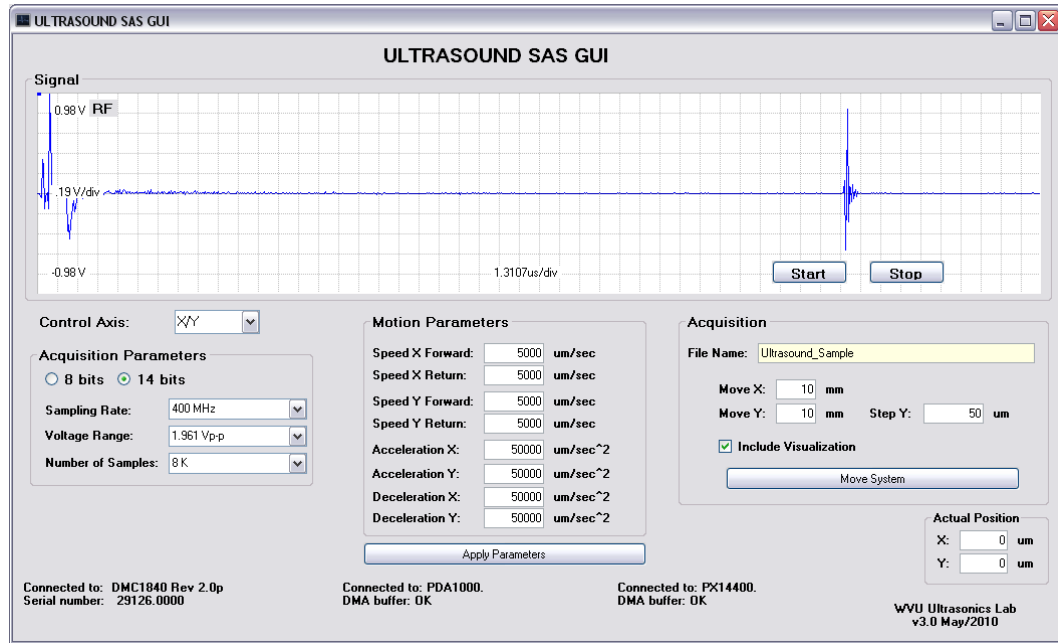


Figure 4.10. High-resolution ultrasound acquisition system GUI after applying the motion parameters.

4.1.5. Experiment Specifications Parameters

Finally, after the acquisition and motion parameters are configured the acquisition GUI allows for the specification of the experiment scan parameters. The experiment scan parameters are the file name for the experiment and the scanning distances (in X or Y axis for a single scanning, or in X and Y axes for a 3D scanning). In addition, when it is a 3D acquisition modality the acquisition GUI has an extra parameter to define the distance between scans (Step Y or Step X parameter, depending if the modality selected is X/Y or Y/X, respectively). Also, the acquisition GUI has a checkmark to allow the plotting of the RF signals that are being saved during the experiment, in order to see and detect errors in the ultrasound experiment. Figure 4.11 shows the experiment specifications parameters section in the high-resolution ultrasound acquisition system GUI for a X/Y scanning. In this case, the scanning section will be 10 mm in the X axis, and 10 mm in the Y axis with a Step Y of 50 μm that is a total of 200 scans. After these parameters are defined the user can start the experiment clicking in the “Move System” button.

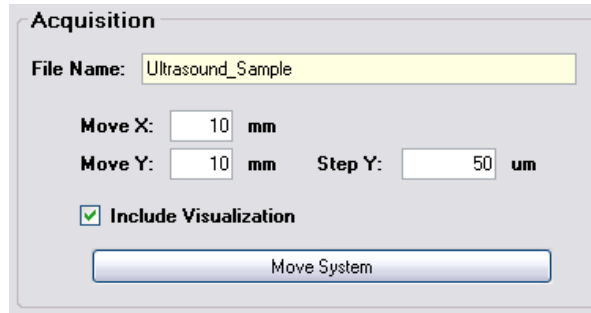


Figure 4.11. Experiment specifications parameters using the acquisition GUI.

When the scanning of the entire region is finalized, the acquisition GUI shows a window to save the experiment data. This allows the user to keep the experiment data or to immediately delete experiment data that had problems or errors during the scanning, as error covering the desired sample region. High-resolution ultrasound experiment data size depends on the A/D acquisition card parameters, the speed motion, and the scanning distance. This data could be from a few Megabytes for a single scan up to a few Gigabytes for a 3D scan. Experiment data is saved in two files: one file with the RF signals in binary format, and other file with all the experiment information: acquisition modality, acquisition card parameters, motion parameters, and scanning specification parameters. In addition, for 3D acquisition experiments it includes the average lateral distance for each scan. After the high-resolution ultrasound experiment data is saved or deleted the acquisition GUI is ready for a new ultrasound experiment with the previous defined parameters, nevertheless new parameters can be defined for the new experiment.

4.1.6. High-Resolution Ultrasound Transducer Description

The high-resolution ultrasound system design and hardware specification used allows the integration of any kind of single-element transducer in a wide range of frequencies from 30 MHz up to 120 MHz. However, during this study a spherical ultrasound transducer with 55.2 MHz in center frequency was used (Olympus NDT Inc., Waltham, MA, USA). Table 4.1 shows the technical specifications of this transducer [66], and Figure 4.12 shows the transducer frequency spectrum.

Table 4.1. Technical specifications for the 55.2 MHz single-element ultrasound transducer

<i>Technical Specification</i>	<i>Value</i>
Center Frequency	55.2 MHz
Peak Frequency	50.4 MHz
-6 dB Bandwidth	52 MHz / 94.098%
Element Diameter Size	0.125 in / 3.175 mm
Focal Length	0.419 in / 10.643 mm

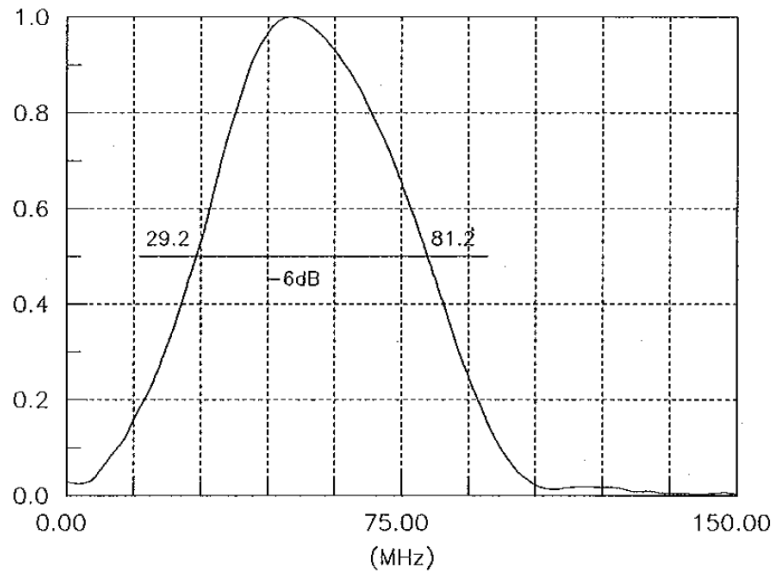


Figure 4.12. Frequency spectrum for the 55.2 MHz single-element ultrasound transducer [66].

4.2. High-Resolution Ultrasound Imaging System GUI

The high-resolution ultrasound imaging system GUI developed in Visual C++ is shown in Figure 4.13. It implements and follows the high-resolution ultrasound imaging procedure previously outlined in Figure 3.1, all in an easier and faster environment. The ultrasound imaging GUI allows the user to apply the 6 post processing techniques, shown in Chapter 3, to high-resolution ultrasound data. In addition, the imaging GUI provides access to the ultrasound data at all stages, allowing the user to interchange, skip, or reapply any of the imaging techniques of the procedure. The high-resolution ultrasound data used for this GUI should be acquired and saved using the high-resolution ultrasound imaging system GUI (Section 4.1) or have the same binary format and structure. The development of this GUI allows for an easy high-resolution ultrasound imaging to any user with basic knowledge in ultrasound and with only a minimum and faster training in the imaging GUI. This capability opens the imaging GUI to any researcher or person interested in reconstructing high-resolution ultrasound data.

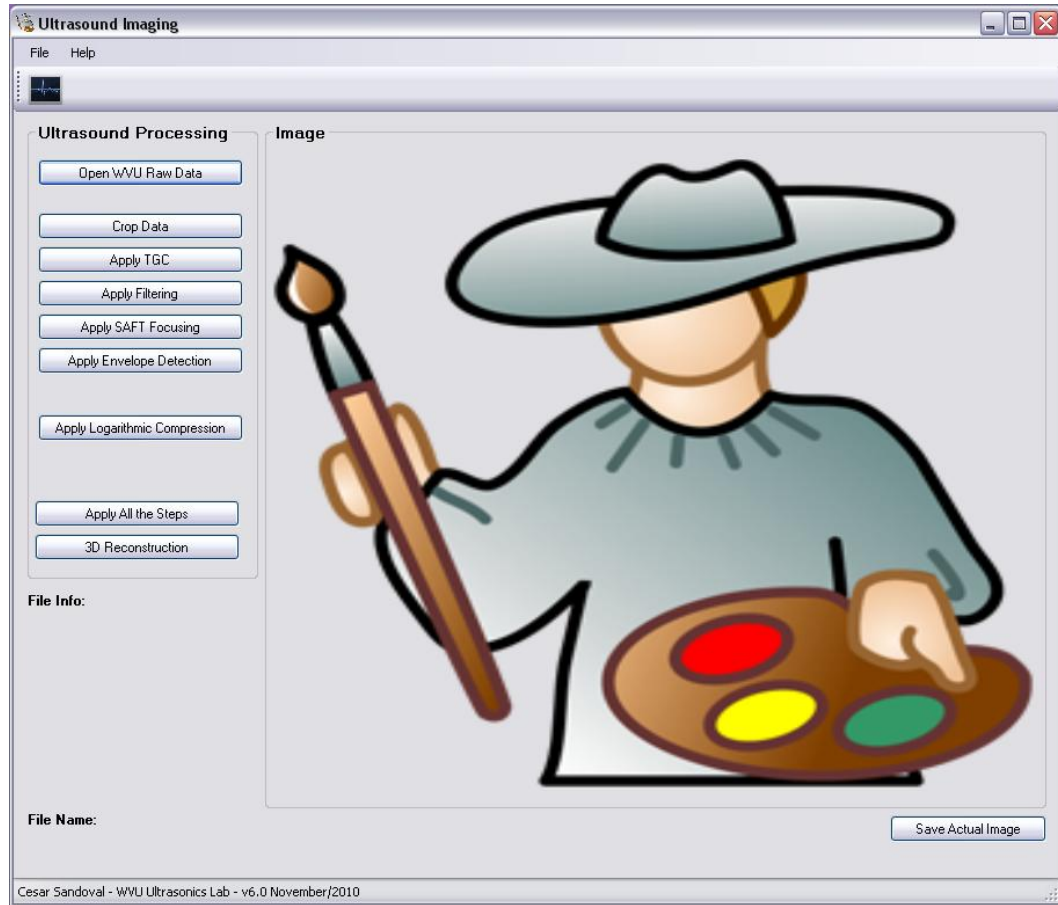


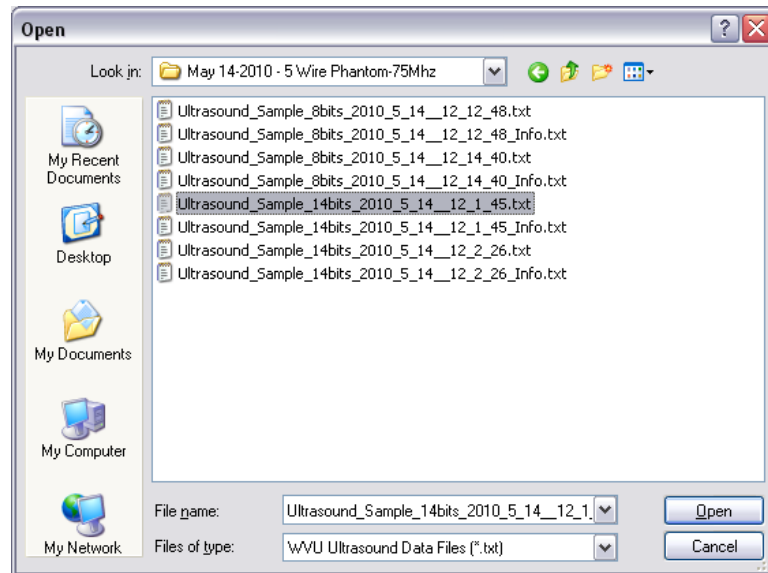
Figure 4.13. High-resolution ultrasound imaging GUI.

The following sections will describe the use and capabilities of the high-resolution ultrasound imaging GUI in detail, from the step of Raw Image and opening of the data to the step of Logarithmic Compression. The high-resolution ultrasound data example had been acquired in our system with a 55.2 MHz transducer and sampling rate of 400 MHz (14 bits of A/D resolution). Ultrasound data corresponds from a cross sectional scan of an 8 μm (diameter) tungsten wire phantom.

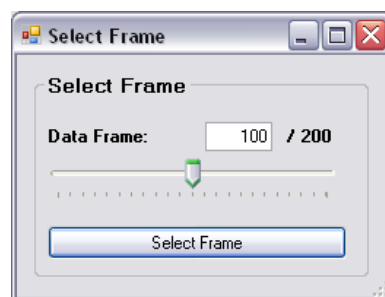
4.2.1. Raw Image

The first step in the high-resolution ultrasound imaging GUI is the opening of the raw data with the radiofrequency (RF) ultrasound signals, where the raw data has not been subjected to any previous manipulation or processing. Using the “Open WVU Raw

Data” button in the imaging GUI allows the user to find and select the data using a file window, as shown in Figure 4.14 (a). Then, the imaging GUI loads the high-resolution ultrasound data and automatically extracts all the ultrasound data parameters from the info file. If the ultrasound data include multiples scans, as 3D data, it automatically allows the selection of a specific scan in the data, as shown in Figure 4.14 (b).



(a) Selecting data file

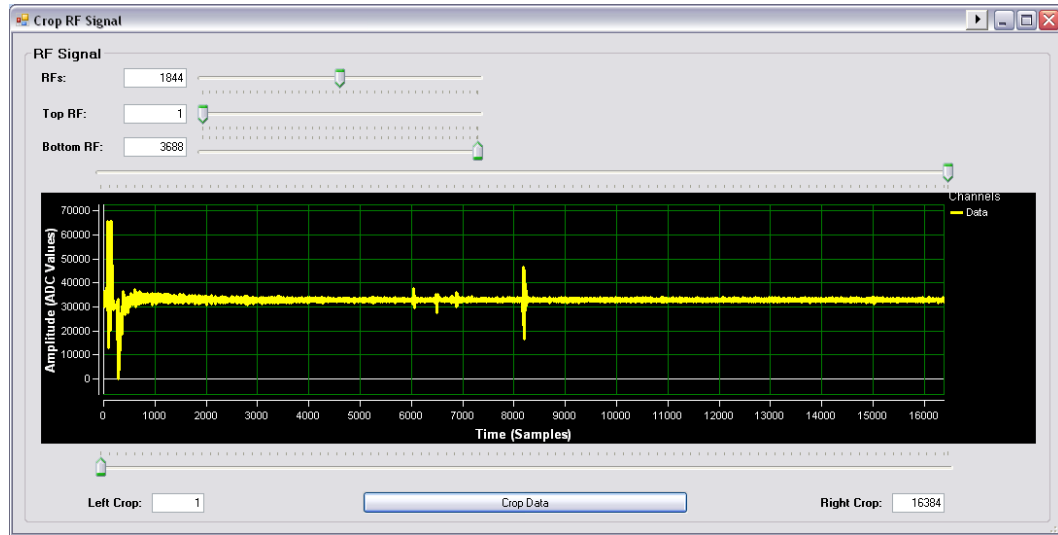


(b) Selecting data scan for 3D data

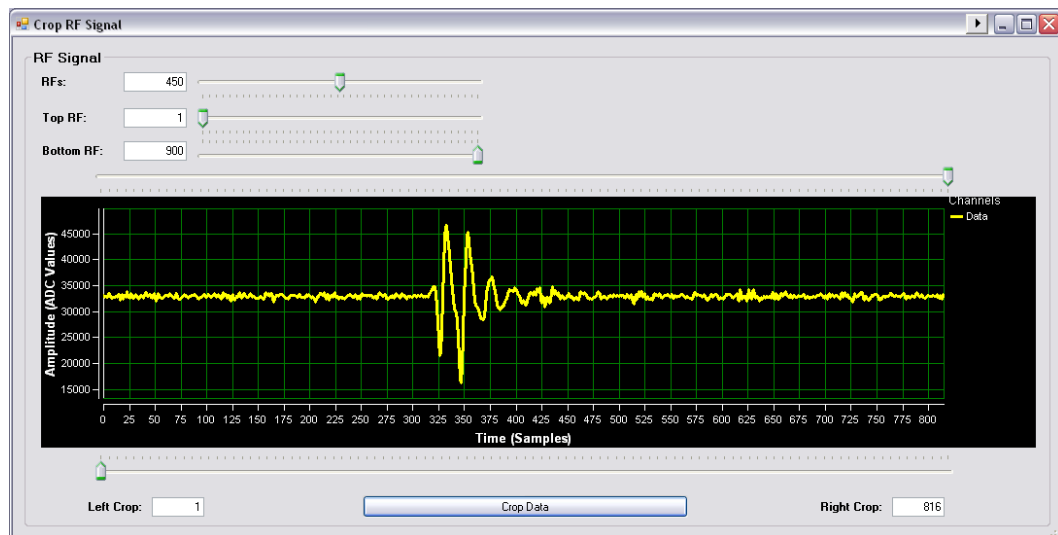
Figure 4.14. Opening raw data using the imaging GUI.

After the ultrasound data scan is loaded, the imaging GUI opens a cropping RF signals window, as shown Figure 4.15 (a). It allows for the analysis of contiguous RF ultrasound signals in order to find the location of the main object region. Main object

region data is then cropped to reduce data and improve the imaging performance. Figure 4.15 (b) shows the RF signal of the wire phantom experiment after the cropping procedure. This step accentuates the interested region and improves the overall composition of the image by removing unwanted areas or irrelevant details from the ultrasound data.



(a) Original RF ultrasound signal



(b) RF Ultrasound signal after cropped

Figure 4.15. Cropping ultrasound data using the imaging GUI.

The cropping step can be repeated as many times as it is necessary using the “Crop Data” button in the imaging GUI, until selecting the specific interest region. Figure 4.16 shows the high-resolution ultrasound imaging GUI after selecting the raw data for the wire data example.

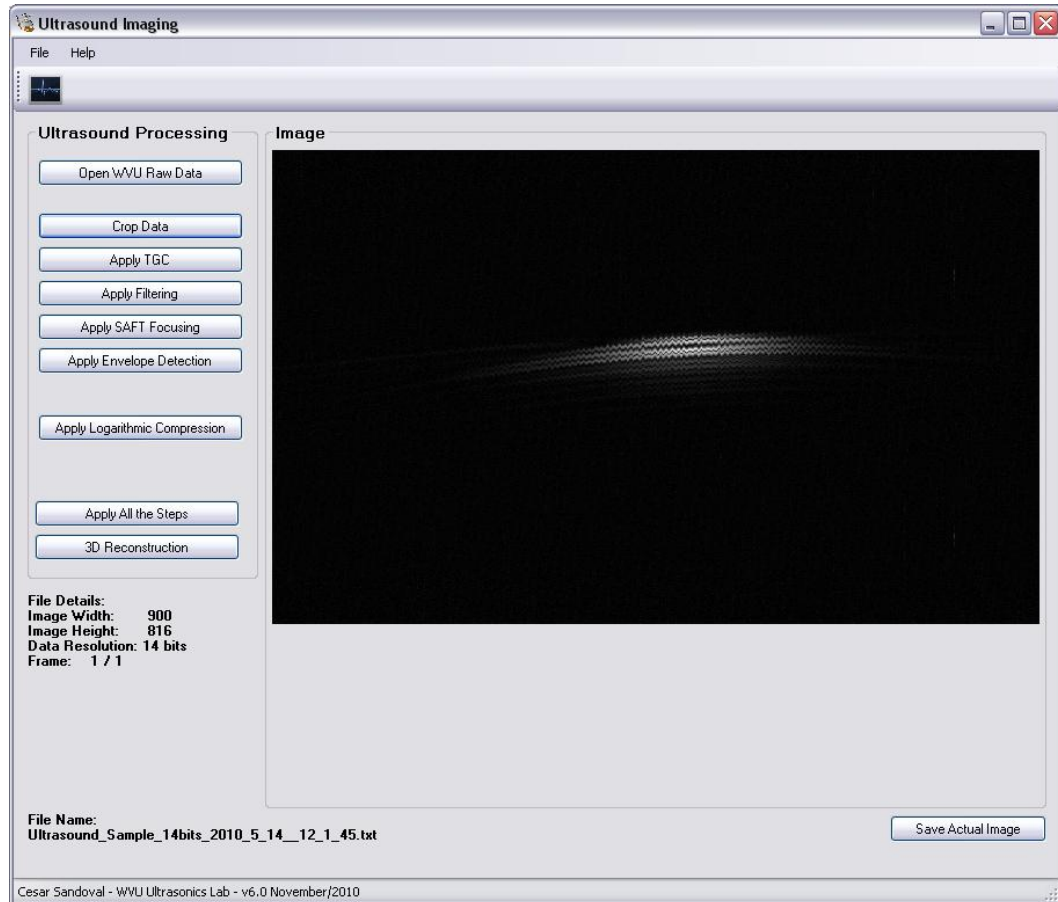


Figure 4.16. High-resolution ultrasound imaging GUI after selecting the raw data.

4.2.2. Time Gain Compensation (TGC)

Another technique in the ultrasound imaging procedure is the time gain compensation or TGC technique. To use this technique the user needs to click the “Apply TGC” button in the imaging GUI. TGC is applied to compensate the attenuation effect of

the ultrasound energy of the tissue as it penetrates deeper into the sample region. Figure 4.17 shows the time gain compensation (TGC) using the imaging GUI. It shows the RF signal at the top, the TGC curve in the middle, and the controls of the TGC gains at the bottom. Any type of TGC curve can be used for the user and applied to the RF signals using the TGC gains controls, in a similar way as a commercial ultrasound machine.

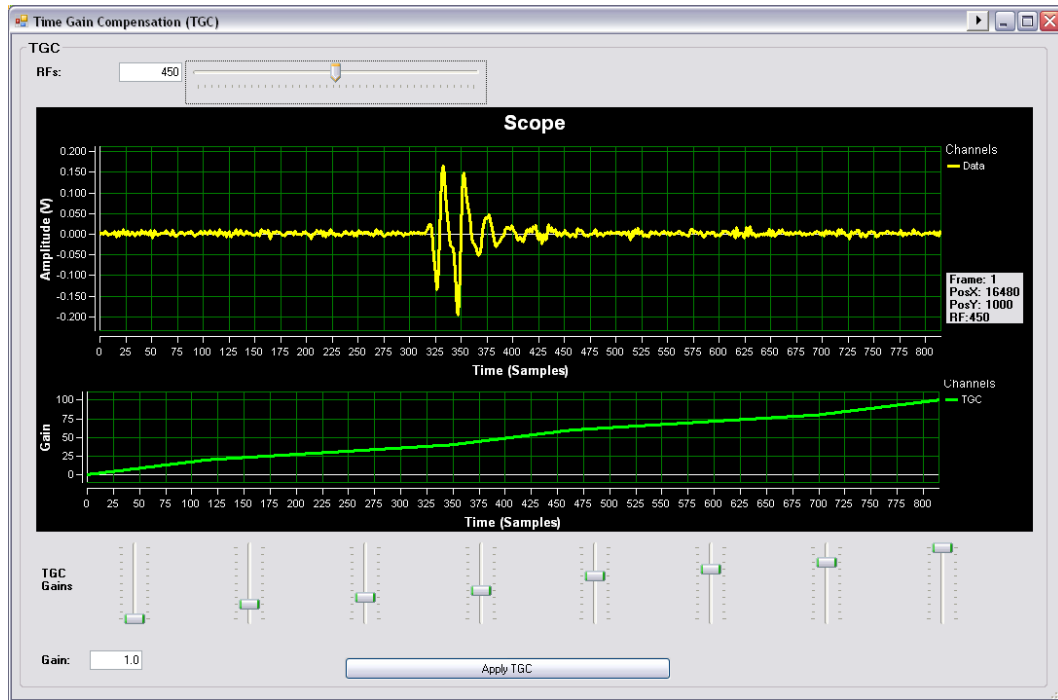


Figure 4.17. Time gain compensation (TGC) using the imaging GUI.

Figure 4.18 shows the high-resolution ultrasound imaging GUI after applying a linear TGC curve to the wire data example, where the gain increases linearly from 1 to 100.

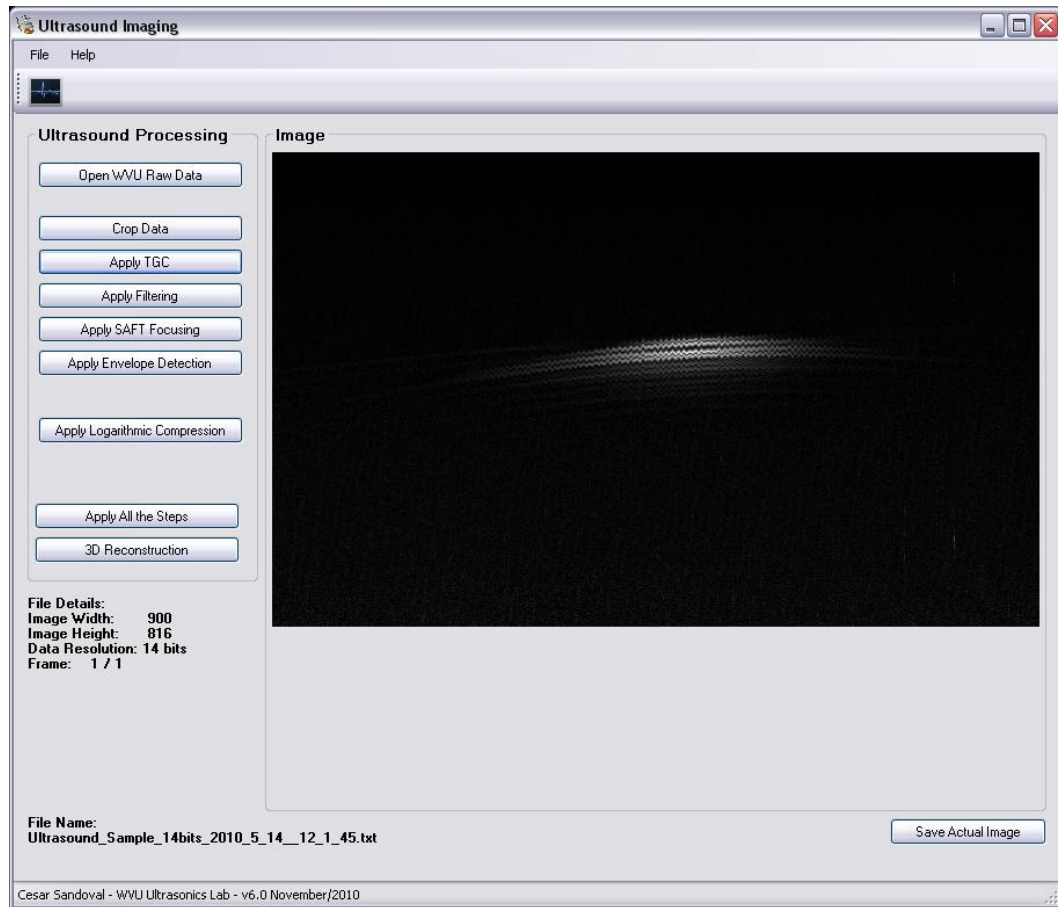


Figure 4.18. High-resolution ultrasound imaging GUI after TGC.

4.2.3. Filtering

Ultrasound data can be filtered using a band pass filter in order to remove noise from the ultrasound data, by clicking in the “Apply Filtering” button in the imaging GUI. The band pass filter implemented is explained in detail in the previous Section 3.3. Figure 4.19 shows the filtering step using the Imaging GUI. It allows the user to see the RF ultrasound signals after the band pass filter (in green) and the actual RF ultrasound data (in yellow). In addition, it allows the user to update the cutoff frequencies (low and high) for the band pass filter and see how the changes in these frequencies affect the filtered RF signals. Note that the cutoff frequencies depend of the central frequency of the transducer used for the acquisition.



Figure 4.19. Filtering using the imaging GUI.

Figure 4.20 shows the high-resolution ultrasound imaging GUI after filtering is applied to the wire data example. The low cutoff frequency was 29.2 MHz and the high cutoff frequency of 81.2 MHz that corresponds to a 94.2% bandwidth of the transducer used.

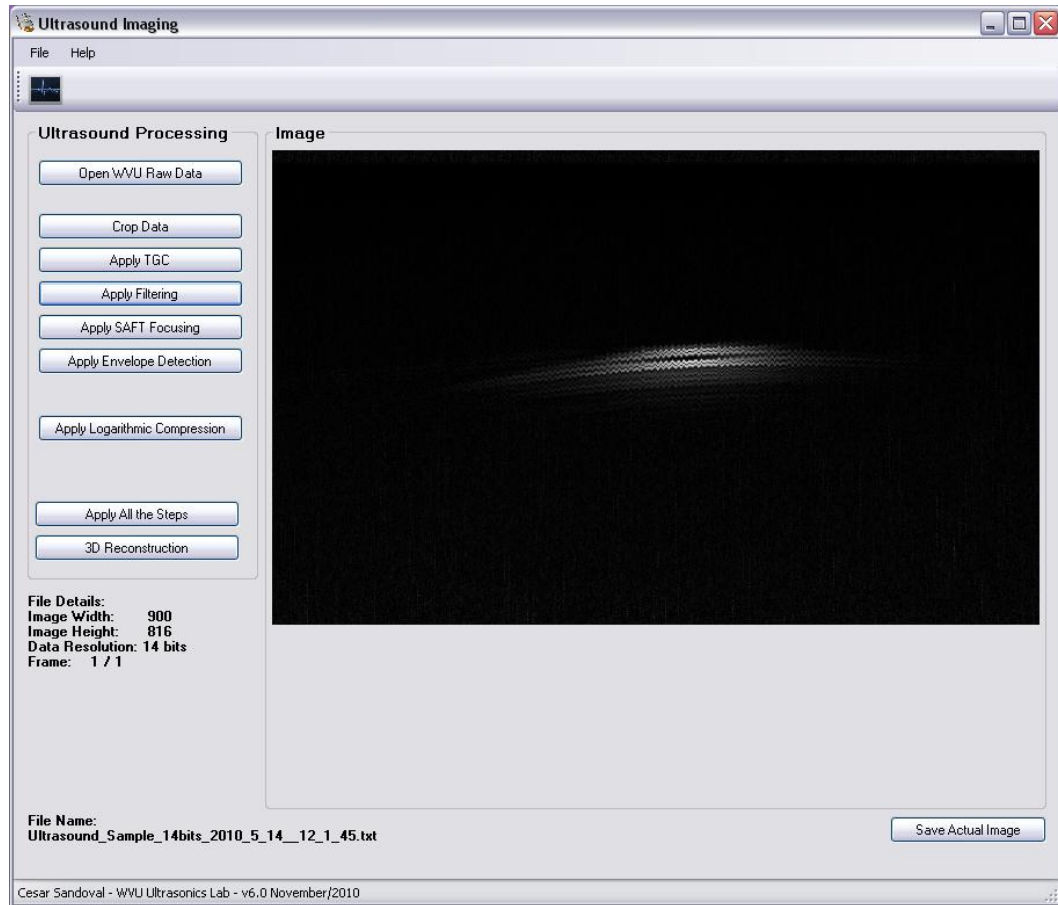


Figure 4.20. High-resolution ultrasound imaging GUI after filtering.

4.2.4. Synthetic Aperture Focusing Technique (SAFT)

The weighted synthetic aperture focusing technique (SAFT) is applied to overcome the limited depth of field for a highly focused transducer and to improve lateral resolution beyond the focus of the transducer. This technique is explained in detail in the previous Section 3.4. Figure 4.21 shows the SAFT window using the imaging GUI, that is loaded by clicking in the “Apply SAFT” button. SAFT parameters (aperture size, synthetic focal point, and transducer focus) are specific parameters of the transducer used and the experiment setup. Figure 4.22 shows the high-resolution ultrasound imaging GUI after SAFT is applied to the wire data example, using aperture size of 8, synthetic focal point of 12 mm, and transducer focus of 9.6 mm.

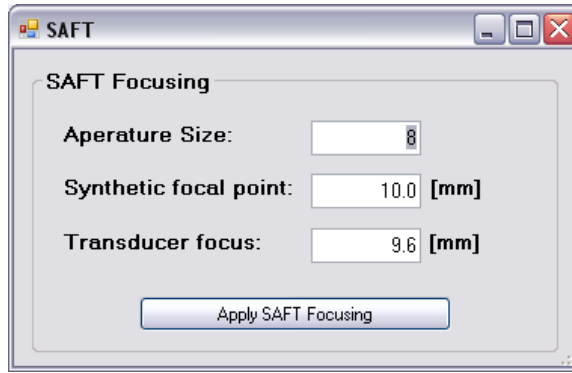


Figure 4.21. SAFT focusing using the imaging GUI.

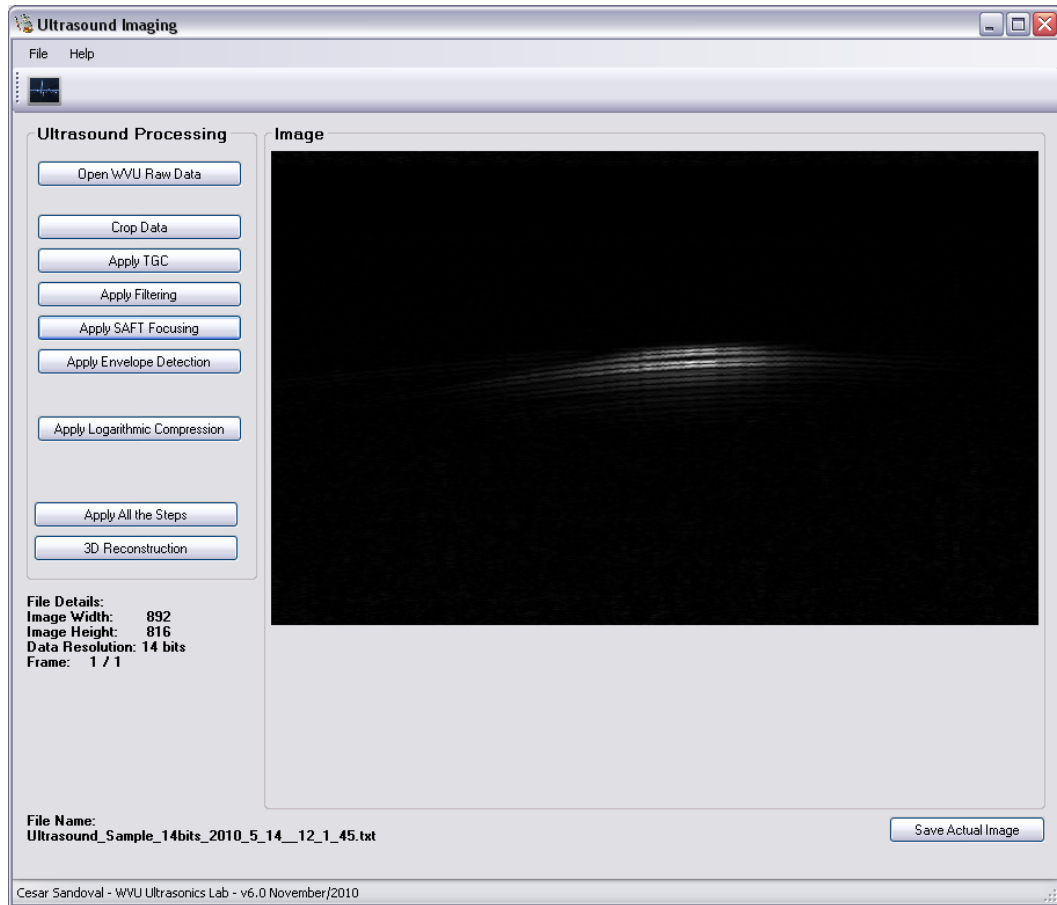


Figure 4.22. High-resolution ultrasound imaging GUI after SAFT focusing.

4.2.5. Envelope Detection (Hilbert Transform)

The envelope detection of the RF signals with Hilbert transform technique can be applied by clicking in the “Apply Envelope Detection” in the high-resolution ultrasound imaging GUI. This technique is explained in detail in the previous Section 3.5. Figure 4.23 shows the envelope detection (Hilbert Transform) using the imaging GUI. In yellow it shows the actual RF ultrasound data, and in green the RF signals after the ideal envelope detector. Figure 4.24 shows the high-resolution ultrasound imaging GUI after envelope detection is applied to the wire data example.

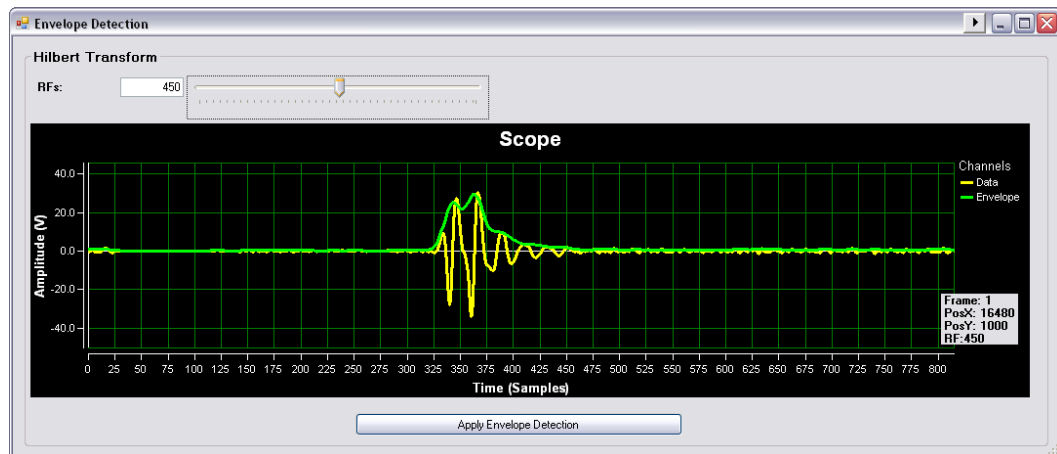


Figure 4.23. Envelope detection (Hilbert transform) using the imaging GUI.

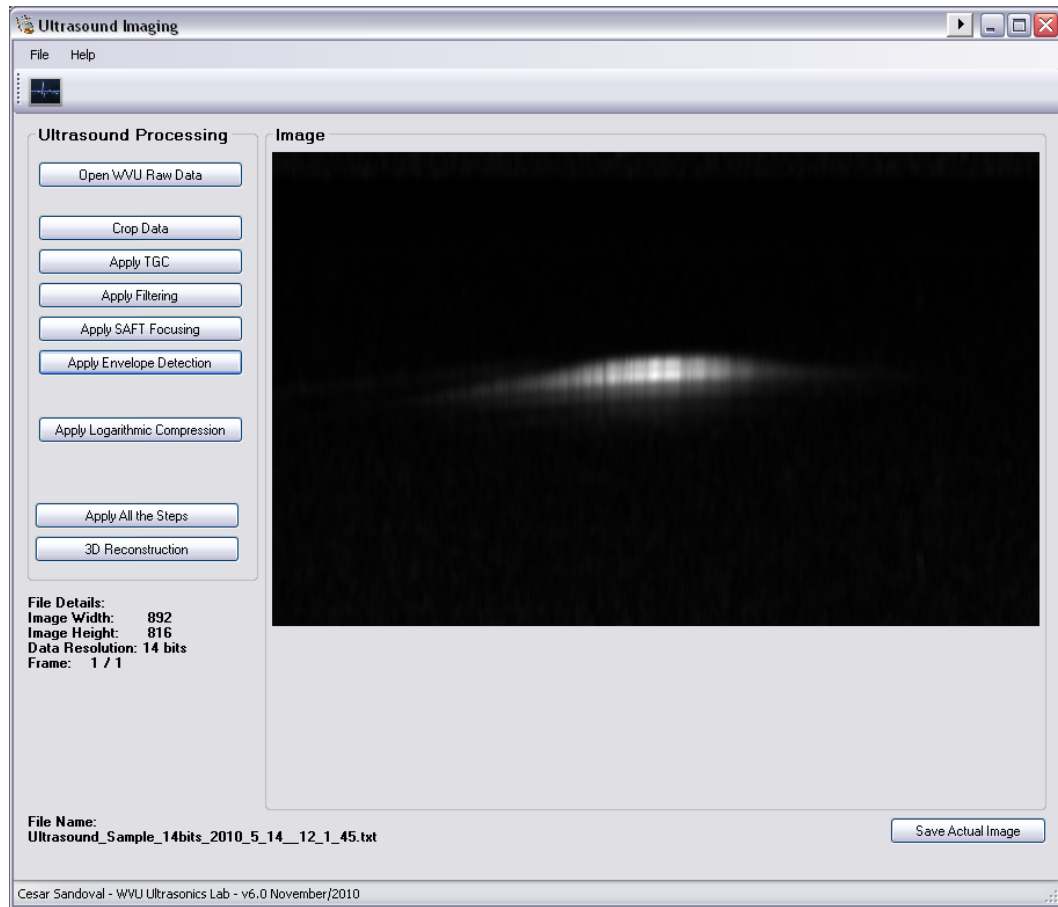


Figure 4.24. High-resolution ultrasound imaging GUI after envelope detection.

4.2.6. Logarithmic Compression

The last technique is the logarithmic compression. It can be applied to the ultrasound data by clicking on the “Apply Logarithmic Compression” button in the imaging GUI. Logarithmic compression is used to reduce the dynamic range of the RF signals for visualization. Figure 4.25 shows the logarithmic compression window using the imaging GUI. It has three main parameters: color data min, color data max, and threshold. The initial values for these parameters are extracted from the actual ultrasound data. Then, the imaging GUI allows the user to see an updated ultrasound image (to the right) after changing each parameter, and this provides a great deal of visualization flexibility to the ultrasound user. This technique is explained in detail in the previous Section 3.6.

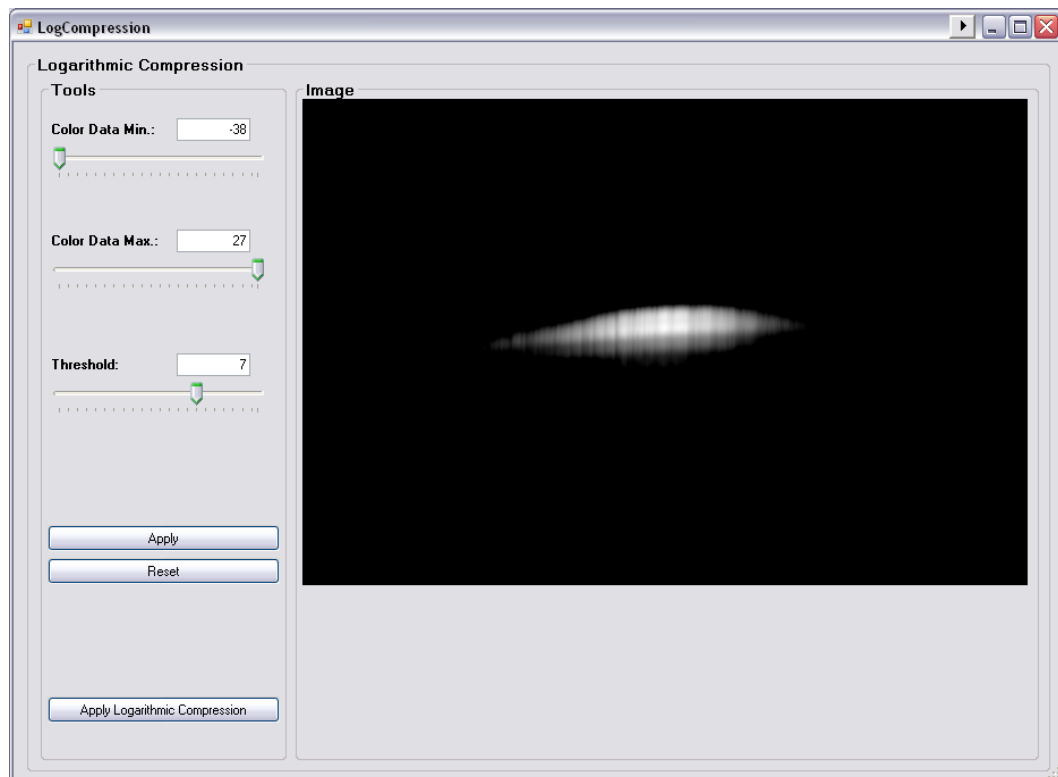


Figure 4.25. Logarithmic compression using the imaging GUI.

After the dynamic range is selected, the high-resolution ultrasound imaging procedure is finalized. Figure 4.26 shows the high-resolution ultrasound imaging GUI after logarithmic compression to the 8 μm wire phantom data, where the dynamic range was assigned as 20 dB.

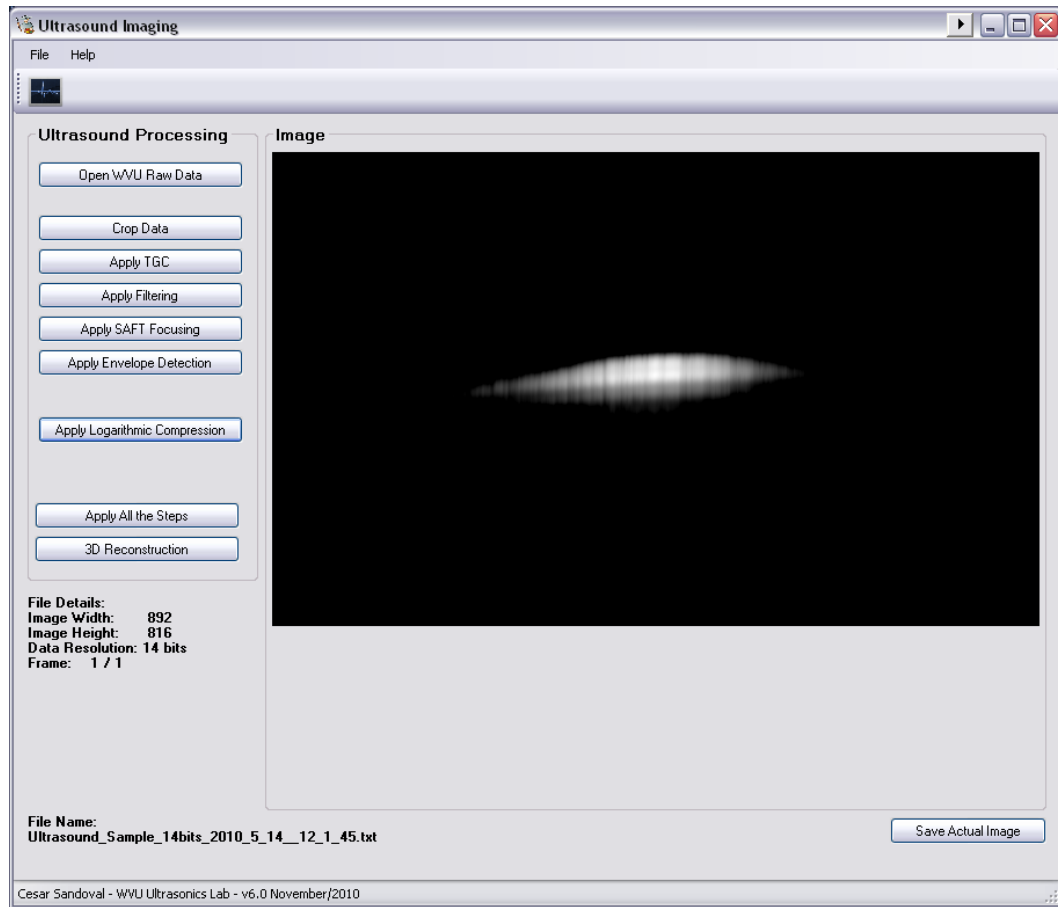


Figure 4.26. High-resolution ultrasound imaging GUI after logarithmic compression.

4.2.7. Save Ultrasound Image

An additional feature of the imaging GUI is the possibility of saving in an image file the actual ultrasound image at any stage of the reconstruction by using the “Save Actual Image” button located at the right in the bottom of the image GUI, as shown in Figure 4.27. It allows the user to save the ultrasound image with the correct aspect ratio of the scanning as a Bitmap format (BMP) file. In addition, the image file can be saved with any name at any location, as shown in Figure 4.28.

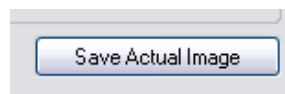


Figure 4.27. Save ultrasound image button in imaging GUI.

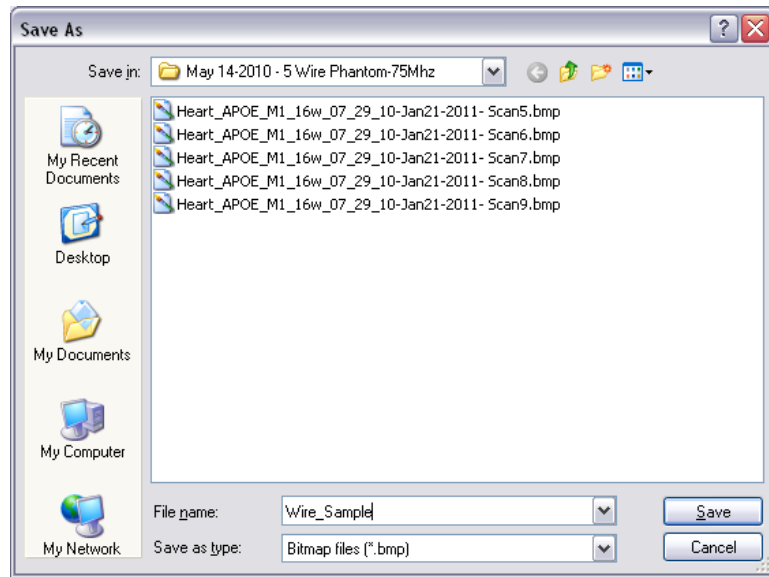


Figure 4.28. Saving ultrasound image window using the imaging GUI.

4.2.8. Ultrasound Reconstruction Sequence

Another extra feature in the imaging GUI is the possibility to apply all the high-resolution ultrasound imaging techniques (Figure 3.1) with only one click. For this, the user can use the “Apply All the Steps” button, that applies the techniques using the default parameters in the imaging GUI or the parameters previously defined by the user. This button is located at the left in the bottom of the imaging GUI, as shown in Figure 4.29. Some benefits of using this option are saving time and improving the overall performance of the reconstruction, as well as having the same dynamic range when reconstructing multiples scans, for example for 3D ultrasound data.

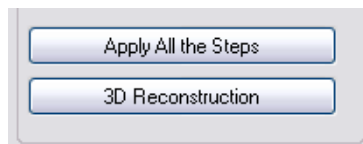


Figure 4.29. Apply all the steps and 3D reconstruction buttons in imaging GUI.

4.2.9. 3D High-Resolution Ultrasound Reconstruction

Finally, the “3D Reconstruction” button, shown in Figure 4.29, allows the reconstruction of multiple scans of 3D ultrasound data by creating a sequence of B-mode images using the same parameters. Figure 4.30 shows the 3D ultrasound reconstruction window using the imaging GUI. It allows the user to select the range of the desired scans from the 3D ultrasound data, to define the normalization factor (use for tissue classification [67]), and to define the dynamic range of the B-mode images. After starting the 3D reconstruction, by the “Start 3D Reconstruction” button, the imaging GUI automatically opens each scan of the 3D data, applies the high-resolution ultrasound imaging procedure (using the default parameters of the techniques or the parameters previously defined by the user), and saves the final B-mode image, generating a set of sequential images. This sequence of B-mode images later allows the 3D visualization (Section 5.1).

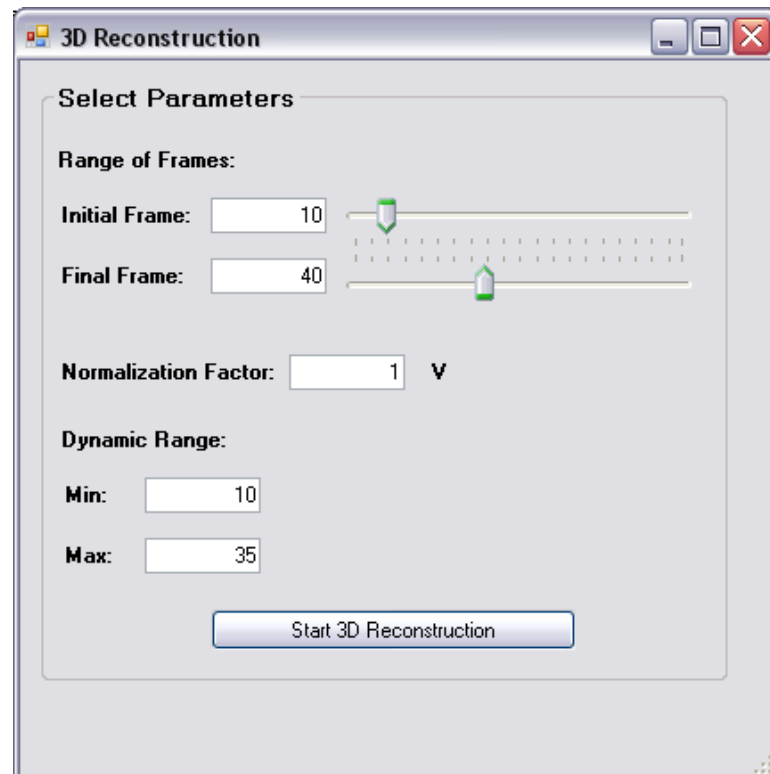


Figure 4.30. 3D ultrasound reconstruction using the imaging GUI.

- CHAPTER 5 -

3D RECONSTRUCTION FOR ATHEROSCLEROSIS

Three-dimensional (3D) ultrasound imaging has been used since the late 1990s [32-35], and was recently employed for the identification and localization of potential atherosclerotic plaques in humans [52, 53]. Regular histology images represent a 2D view of atherosclerosis and are not able to render the plaque volume and/or complete morphology of a sample. Also, conventional ultrasound B-mode images represent thin slices of an organ anatomy at a specific location and orientation, which are difficult to analyze manually at a later time, particularly in small animals studies. Additionally, 3D image reconstructions can be used to locate and select 2D regions of interest (ROI) precisely instead of using a reference point or a surgical needle. In this work, 3D ultrasound images for hearts and small vessels of mice with atherosclerosis are reconstructed, finding accurate and precise atherosclerosis plaque size and orientation in various mouse models.

5.1. 3D Reconstruction Methodology

A set of sequential scans were acquired using our ultrasound imaging system GUI (Section 4.2). This sequence of scans allows 3D data representation of the scanned region. The high-resolution B-mode ultrasound image techniques (Figure 3.1) were applied to each scan generating a set of sequential images. The sequence of images was opened in MATLAB 7.1 (The MathWorks, Inc., Natick, MA, USA) in order to generate a 3D data file with the entire sequence of images. In addition, a parameters information file was created including the images resolution, number of scans, data format, and acquisition parameters. The two files were created to aid the volume data analysis and visualization. The 3D data files were integrated into the Voreen volume rendering engine

[68] that provides a great deal of visualization flexibility and allows the 3D image reconstruction. The 3D ultrasound reconstruction allows an easy volumetric data analysis for atherosclerotic plaque assessment through varying all the relevant 3D rendering parameters such as transfer functions, lighting parameters, and camera view. In addition, volumetric data analysis allows the detection of lesions with atherosclerotic plaque for a later volume measurement (Section 5.4).

5.2. *Mice Samples Origin*

All animals were part of the colony maintained by Drs. Mustafa and Teng at the Health Science Center (HSC) in West Virginia University. These mice were cared for in accordance with the protocol approved by WVU Animal Care and Use committee. The mice housed in the HSC laboratory was at a temperature constant at $23 \pm 2^\circ\text{C}$ and humidity at $60 \pm 10\%$, where an inverted light-dark cycle of 12:12 h was used, and the food and water were available *ad libitum*. A series of apolipoprotein E-knockout (APOE) and the apolipoprotein E-A1 adenosine receptor double knockout (DKO) mice model with their wild type control (C57) were used. These mouse models are described in [69, 70]. A previous study from our group has shown a decrease in atherosclerosis development in DKO when compared to APOE [71]. Therefore, we used DKO mouse model to test the severity of the atherosclerosis lesions with ultrasound imaging.

While mice were under deep anesthesia with pentobarbital sodium (100 mg/kg ip), a thoracotomy was performed. The heart and aorta were gently removed. Fat and connective tissue was carefully removed. Aorta was cut off at the base of the heart. Both heart and aorta were fixed in 10% phosphate-buffered formalin before the *in vitro* scans. *In vitro* experiments were conducted to investigate the efficacy of the system on reconstructing high-resolution B-mode and parametric images for real objects. Studies were performed to image isolated mouse hearts (16-20 week old) and mouse

vessels (aortas and carotids) (50 week old) of APOE and DKO and the wild type control C57 (70 weeks old).

Mouse hearts and mouse vessels (aortas and carotids) were placed near the transducer focus on a thin layer of silicone gel lining in a glass plate and forming the reference echos. RF signals were collected using a separation distances along the scan line down to 8.5 μm between adjacent signals. More than ninety ultrasound scans down to 50 μm apart in the elevation direction were acquired for the short axis of mouse hearts covering from the upper part to the lower part including the aortic root. In addition, more than 150 cross-sectional ultrasound scans were acquired for each mouse artery covering from the aortic sinus to the thoracic aorta.

The following tables summarize the mouse samples used in this study. Table 5.1 and Table 5.2 show a summary of the mouse aortas and carotids samples organized by name and category respectively. Table 5.3 and Table 5.4 show a summary of the mouse hearts samples organized by name and category respectively. All these samples were acquired and reconstructed in 3D using our high-resolution ultrasound system. During this study we analyzed and reconstructed in 3D a total of 26 mouse arteries samples and 15 mouse hearts samples.

Table 5.1. Mouse aortas and carotids samples by name

Sample	Artery	Type	Gender	Weeks	Parts	Date
1	Aorta	APOE	F	50	1	11/18/2010
2	Aorta	APOE	F1	50	1	10/27/2010
3	Aorta	APOE	M	50	1	10/27/2010
4	Aorta	APOE	M	50	1	11/18/2010
5	Aorta	APOE	M1	50	1	9/4/2010
6	Aorta	C57	F	70	2	10/20/2010
7	Aorta	C57	M	70	1	10/12/2010
8	Aorta	DKO	F1	50	1	9/23/2010
9	Aorta	DKO	M1	50	1	11/22/2010
10	Aorta	DKO	M2	50	1	11/22/2010
11	Carotid	APOE	F	50	1	11/18/2010
12	Carotid	APOE	M	50	2	11/18/2010
13	Carotid	C57	F	70	2	10/20/2010
14	Carotid	C57	M	70	2	10/20/2010
15	Carotid	DKO	F1	50	2	9/23/2010
16	Carotid	DKO	F2	50	2	9/15/2010
17	Carotid	DKO	M1	50	2	11/22/2010
18	Carotid	DKO	M3	50	2	11/22/2010

Table 5.2. Mouse aortas and carotids samples by category

Sample	Artery		Type			Gender		Weeks	Parts	Date
	Aorta	Carotid	APOE	C57	DKO	Female	Male			
1	X		X			X		50	1	11/18/2010
2	X		X			X		50	1	10/27/2010
3	X		X				X	50	1	10/27/2010
4	X		X				X	50	1	11/18/2010
5	X		X				X	50	1	9/4/2010
6	X			X		X		70	2	10/20/2010
7	X			X			X	70	1	10/12/2010
8	X				X	X		50	1	9/23/2010
9	X				X		X	50	1	11/22/2010
10	X				X		X	50	1	11/22/2010
11		X	X			X		50	1	11/18/2010
12		X	X				X	50	2	11/18/2010
13		X		X		X		70	2	10/20/2010
14		X		X			X	70	2	10/20/2010
15		X			X	X		50	2	9/23/2010
16		X			X	X		50	2	9/15/2010
17		X			X		X	50	2	11/22/2010
18		X			X		X	50	2	11/22/2010
Total	10	8	7	4	7	8	10		26	

Table 5.3. Mouse hearts samples by name

Sample	Organ	Type	Gender	Weeks	Date
1	Heart	APOE	F2	20	4/23/2010
2	Heart	APOE	F1	20	5/21/2010
3	Heart	APOE	F2	20	5/21/2010
4	Heart	APOE	M1	20	5/21/2010
5	Heart	APOE	M2	20	5/21/2010
6	Heart	APOE	M1	20	6/4/2010
7	Heart	APOE	M2	20	6/4/2010
8	Heart	APOE	M3	20	6/4/2010
9	Heart	APOE	M1	16	7/29/2010
10	Heart	APOE	M2	16	7/29/2010
11	Heart	APOE	M	16	1/19/2011
12	Heart	C57	M2	20	4/23/2010
13	Heart	DKO	M1	16	7/28/2010
14	Heart	DKO	M2	16	7/28/2010
15	Heart	DKO	M1	16	8/5/2010

Table 5.4. Mouse hearts samples by category

Sample	Heart	Type			Gender		Weeks	Date
		APOE	C57	DKO	Female	Male		
1	X	X			X		20	4/23/2010
2	X	X			X		20	5/21/2010
3	X	X			X		20	5/21/2010
4	X	X				X	20	5/21/2010
5	X	X				X	20	5/21/2010
6	X	X				X	20	6/4/2010
7	X	X				X	20	6/4/2010
8	X	X				X	20	6/4/2010
9	X	X				X	16	7/29/2010
10	X	X				X	16	7/29/2010
11	X	X				X	16	1/19/2011
12	X		X			X	20	4/23/2010
13	X			X		X	16	7/28/2010
14	X			X		X	16	7/28/2010
15	X			X		X	16	8/5/2010
Total	15	11	1	3	3	12		

5.3. 3D Reconstruction Result

3D ultrasound reconstruction allows the user to analyze a sample from outside and inside by rotating around any angle and cropping non-relevant data, allowing them to observe shape and appearance of the 3D structures. In addition, 3D reconstruction allows the user to reconstruct B-mode images of the cross sectional and longitudinal views, that were not available initially with the original transversal scans, as shown in Figure 5.1.

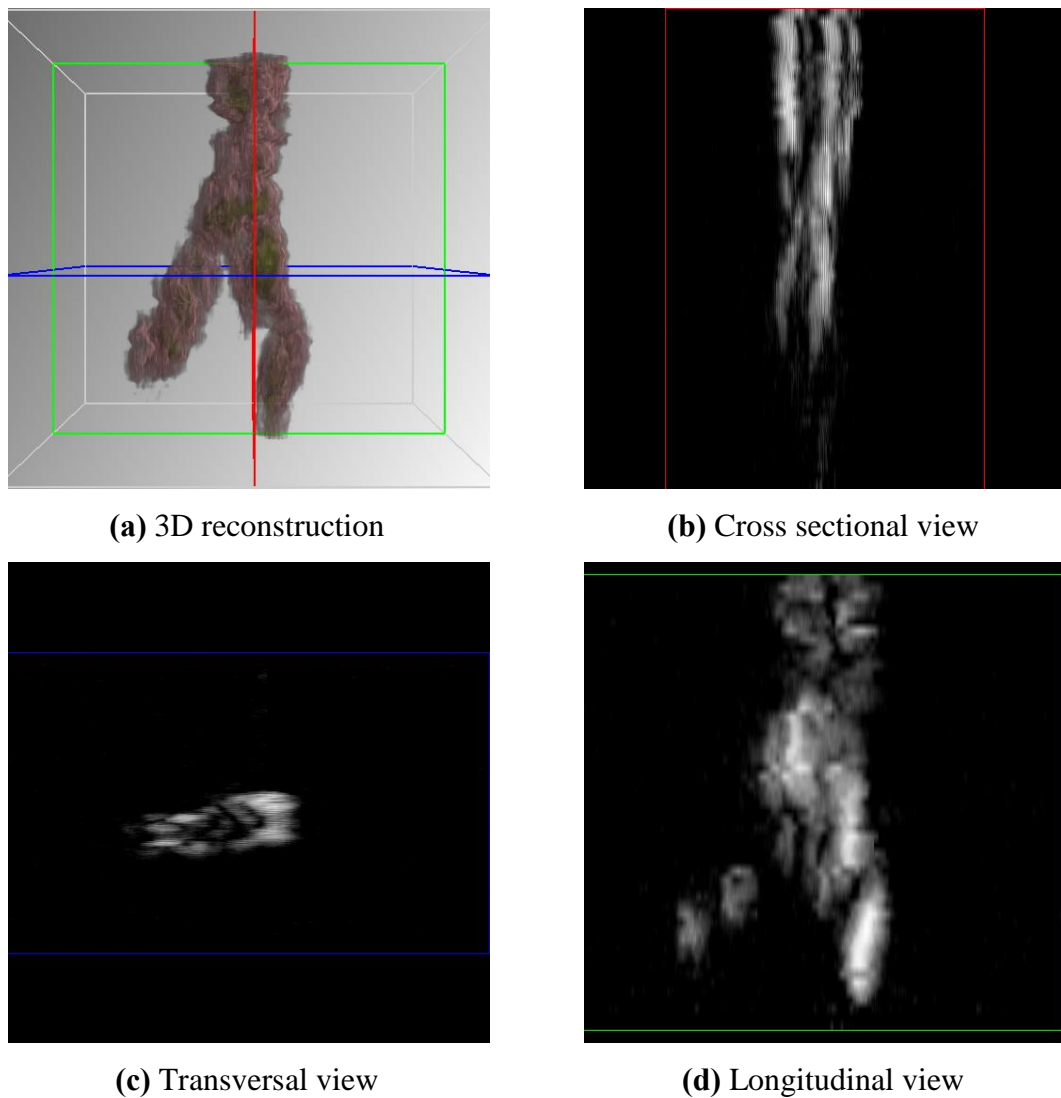


Figure 5.1. Transversal views of the 3D ultrasound reconstruction of the aorta APOE M1 50 weeks – Sample 5.

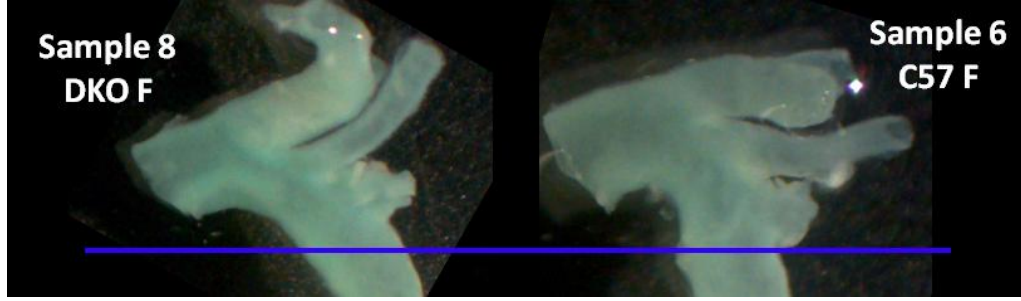
Figure 5.1 shows the possibility of other transversal views for 3D ultrasound data: (a) is the 3D reconstruction, (c) is one of the original transversal B-mode images (blue plane in figure (a)), (b) and (d) are B-mode images of the cross sectional and longitudinal views (red and green planes in figure (a)) respectively, that were reconstructed using the original transversal scans. 3D data corresponds to sample 5 in Table 5.1 or Table 5.2 for a APOE mouse aorta at 50 weeks.

All the 3D images results showing in this chapter were reconstructed using the Voreen volume rendering engine [68].

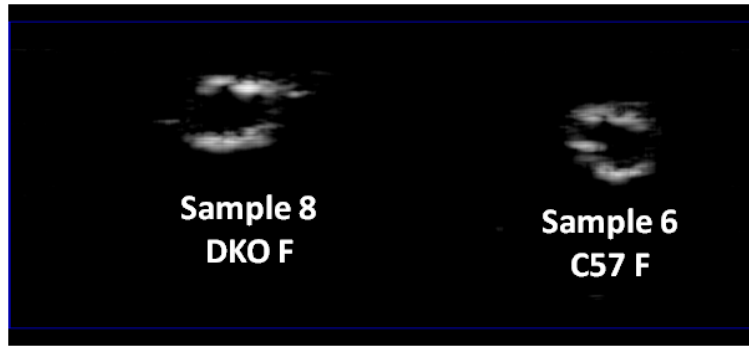
5.3.1. 3D Mouse Aortas and Carotids

To assess atherosclerosis more closely, a series of *in vitro* studies were performed to scan vessels of mouse aortas and mouse carotids with atherosclerosis. The adventia layer was removed from all samples, and the intima and media layers were kept where atherosclerotic plaques were expected. 3D reconstructions were rendered showing good matches with the vessel morphology. In addition, 3D sections of the data were reconstructed showing atherosclerotic plaque in the samples.

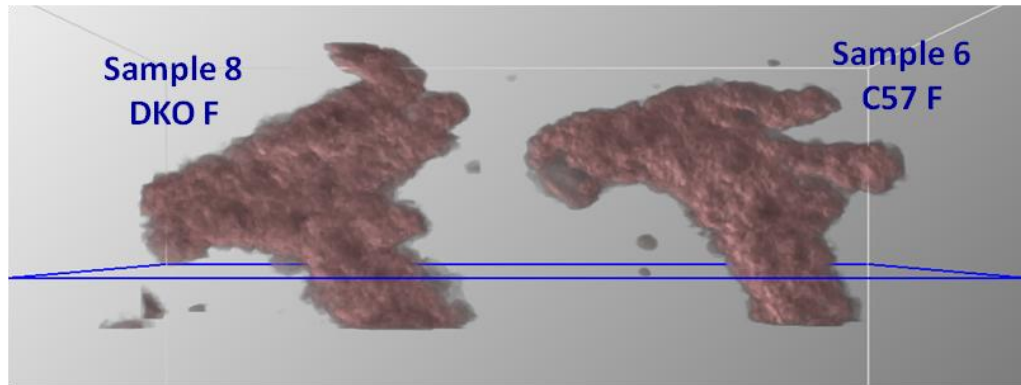
Figure 5.2 shows the morphology match of optical images with the 3D ultrasound reconstructions for a experiment acquiring two mouse aortas at the same time: (a) shows the optical image of the samples acquired with the aid of a microscope, (c) shows the 3D structure of the samples after 3D ultrasound reconstruction, and (b) corresponds to the B-mode image of the cross section located at the blue lines in figures (a) and (c). The samples scanned were an Aorta DKO F of 50 weeks (Sample 8) and an Aorta C57 F (Sample 6) of 70 weeks. It could be seen from Figure 5.2 that the 3D reconstruction has a good structural match with the optical image of the samples. This aids to select precisely the B-mode ultrasound images of cross sectional scans with atherosclerotic plaque without the need of using reference points or surgical needles.



(a) Optical image



(b) B-Mode cross section

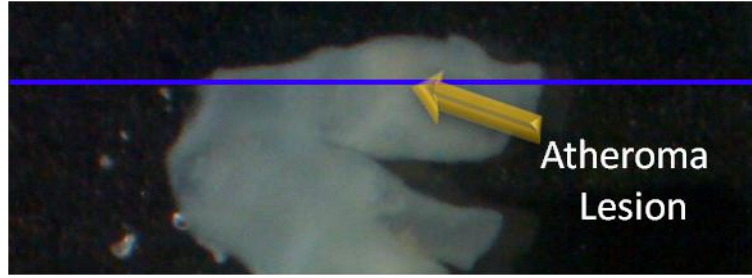


(c) 3D reconstruction

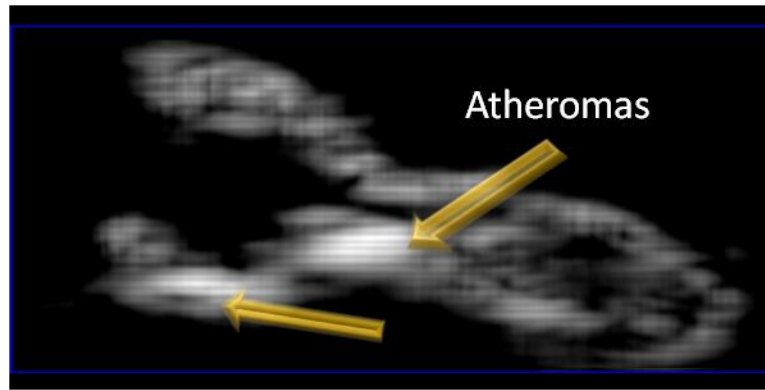
Figure 5.2. 3D ultrasound reconstruction of aorta DKO F (50 weeks, sample 8) and aorta C57 F (70 weeks, sample 6).

The 3D ultrasound reconstructions were used with mouse aortas and mouse carotids samples to compare images of the wild type control C57 with those of severe atherosclerosis (APOE mouse model) and with mild atherosclerosis (DKO mouse model). Figure 5.3 and Figure 5.4 show 3D results for the APOE mouse model, Figure 5.5 and Figure 5.6 show 3D results for the DKO mouse model, and Figure 5.7 and Figure 5.8 show 3D results for the C57 mouse model. Each figure describes a comparison between the optical and 3D images for aortas samples, where the 3D reconstruction corresponds to a section of the 3D data where atherosclerotic components were found. Atherosclerotic components such as calcification and fibrosis have strong ultrasound reflections and these are seen in 3D by using tuned transparency parameters when rendering the 3D section. Arrows in figures indicate patches of such atherosclerotic components developed in the aortas of the mice. The blue lines correspond to the cross section of interest and 3D reconstruction includes scans around this cross section. Data corresponds to 3D ultrasound acquisitions of samples in Table 5.1 or Table 5.2.

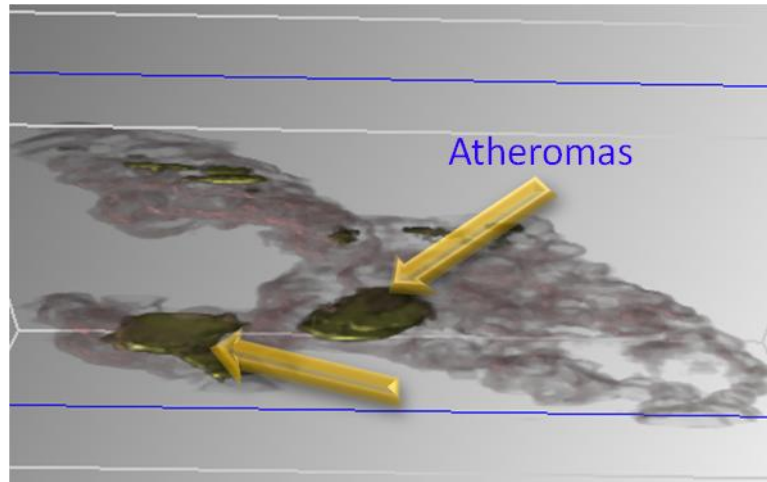
From Figures 5.3 to 5.6 for APOE and DKO mouse models it can be seen that atherosclerotic plaque is found at the region of the aorta bifurcation, as indicated with the yellow arrows and the blue line. On the other hand, Figures 5.7 and 5.8 for C57 control mouse model show no signs of atherosclerotic plaque. Additionally, the plaque lesions of DKO are smaller areas than those of APOE. These findings are in agreement with a previous study of our group for these mouse models [71].



(a) Optical image

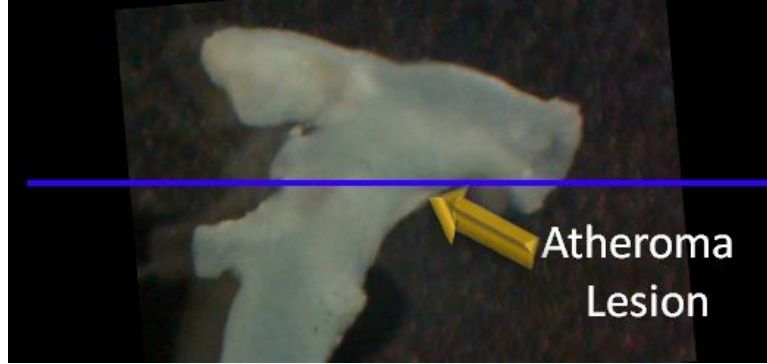


(b) B-Mode cross section

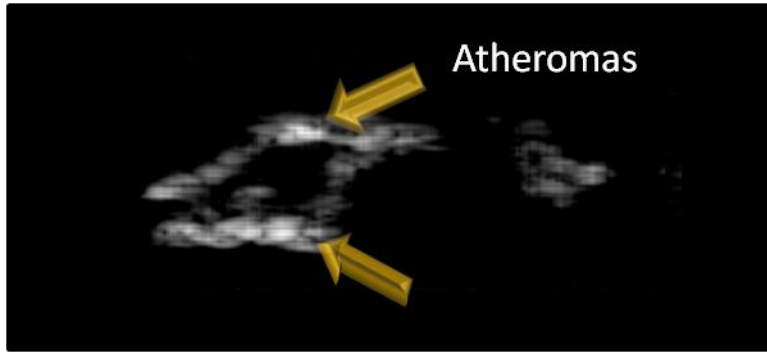


(c) 3D reconstruction - Atheroma lesion slide - Front view

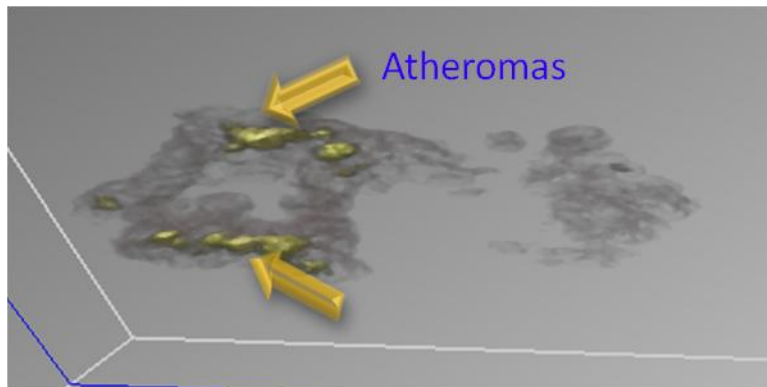
Figure 5.3. 3D ultrasound reconstruction of aorta APOE M 50 weeks – Sample 3.



(a) Optical image

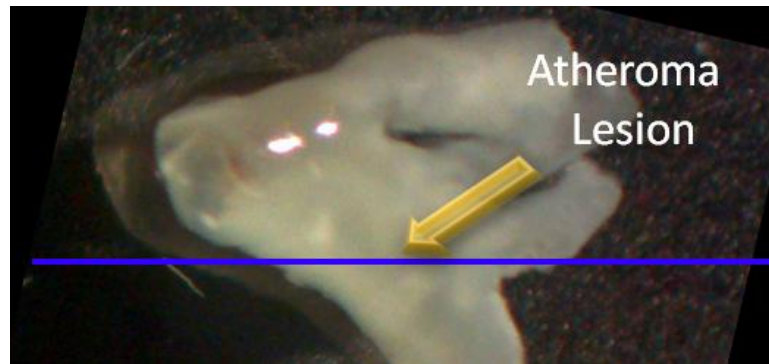


(b) B-Mode cross section

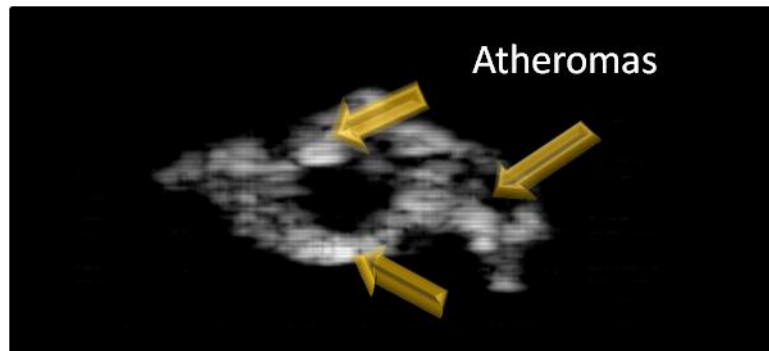


(c) 3D reconstruction - Atheroma lesion slide - Front view

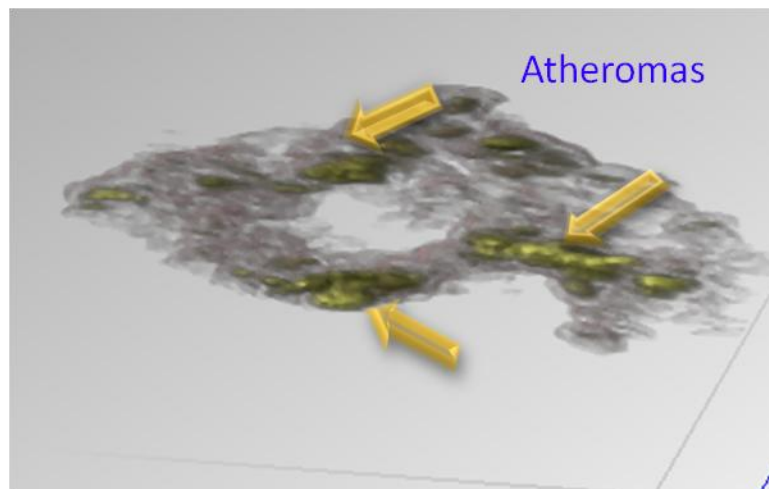
Figure 5.4. 3D ultrasound reconstruction of aorta APOE F 50 weeks – Sample 1.



(a) Optical image



(b) B-Mode cross section

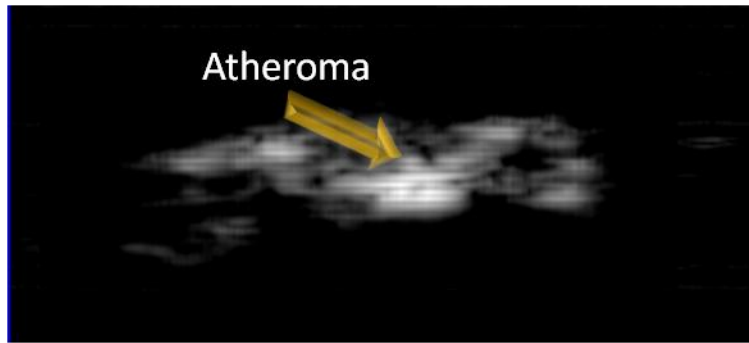


(c) 3D reconstruction - Atheroma lesion slide - Front view

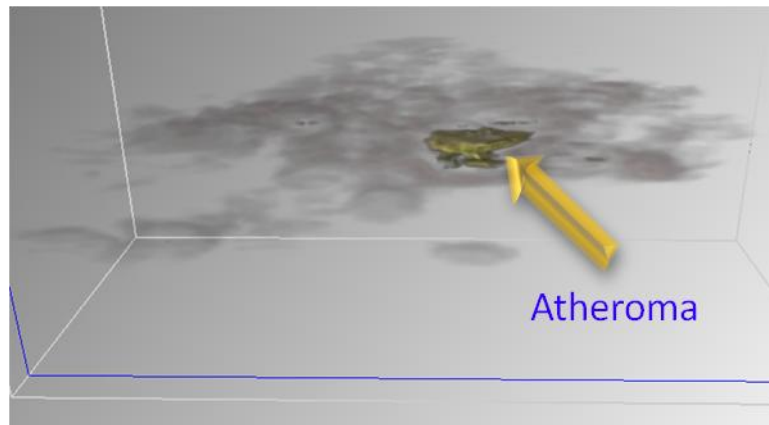
Figure 5.5. 3D ultrasound reconstruction of aorta DKO M1 50 weeks – Sample 9.



(a) Optical image



(b) B-Mode cross section

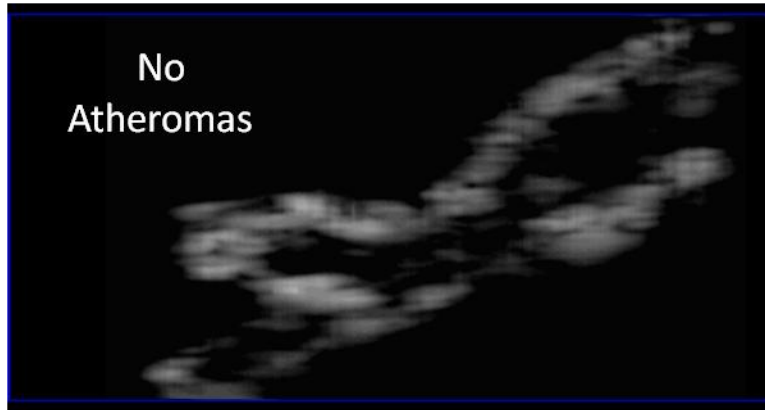


(c) 3D reconstruction - Atheroma lesion slide - Front view

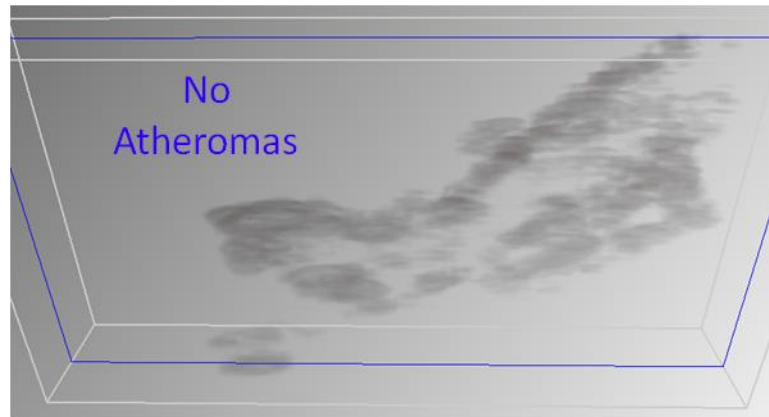
Figure 5.6. 3D ultrasound reconstruction of aorta DKO F1 50 weeks – Sample 8.



(a) Optical image

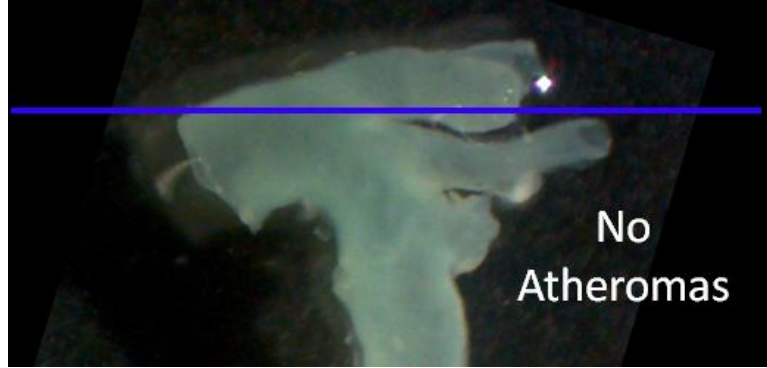


(b) B-Mode cross section

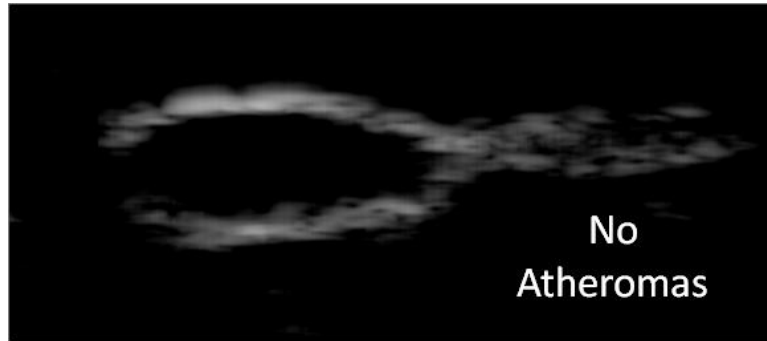


(c) 3D reconstruction – No atheroma lesion slide - Front view

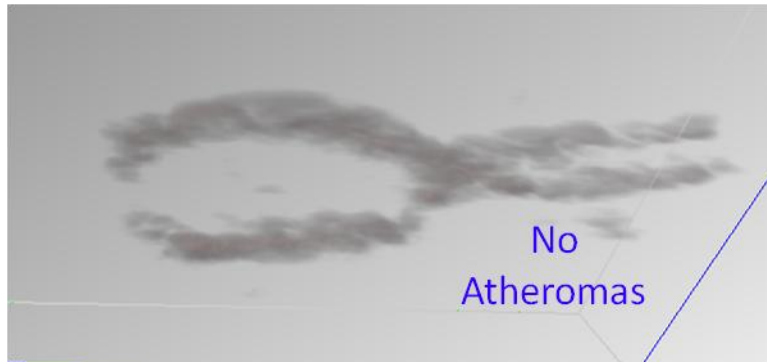
Figure 5.7. 3D ultrasound reconstruction of aorta C57 M 70 weeks – Sample 7.



(a) Optical image



(b) B-Mode cross section



(c) 3D reconstruction – No atheroma lesion slide - Front view

Figure 5.8. 3D ultrasound reconstruction of aorta C57 F 70 weeks – Sample 6.

5.3.2. 3D Mouse Hearts

In a similar way, a series of *in vitro* studies were performed with mouse hearts using our high-resolution ultrasound system. Mouse hearts were scanned in 3D from top to bottom covering their entire region. Figure 5.9 and Figure 5.10 show 3D ultrasound reconstructions for an APOE and DKO mouse model respectively. These figures show in part (a) the optical images of the sample acquired, in part (b) the 3D structure of the samples after 3D ultrasound reconstruction, and in part (c) the B-mode image of the cross section located at the blue lines in figures (a) and (b). Data corresponds to 3D ultrasound acquisitions of samples in Table 5.3 or Table 5.4.

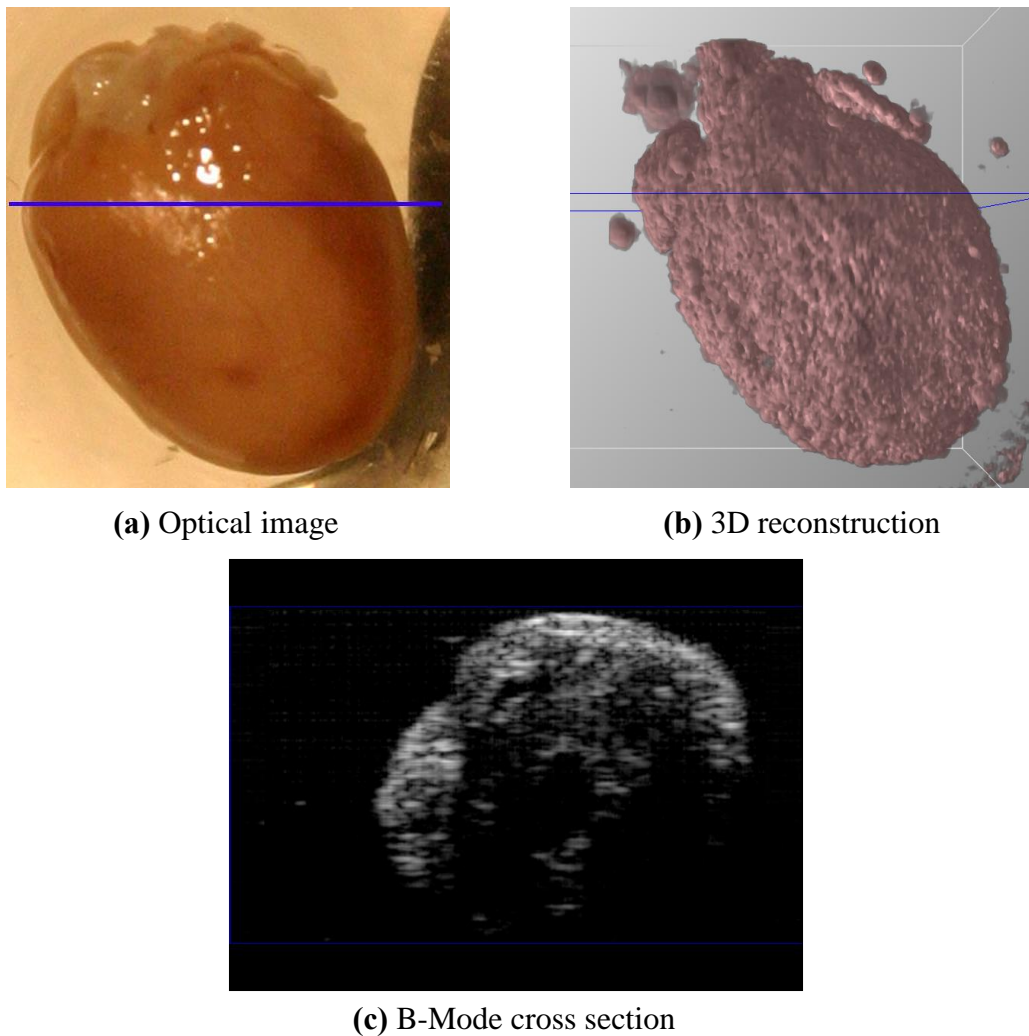
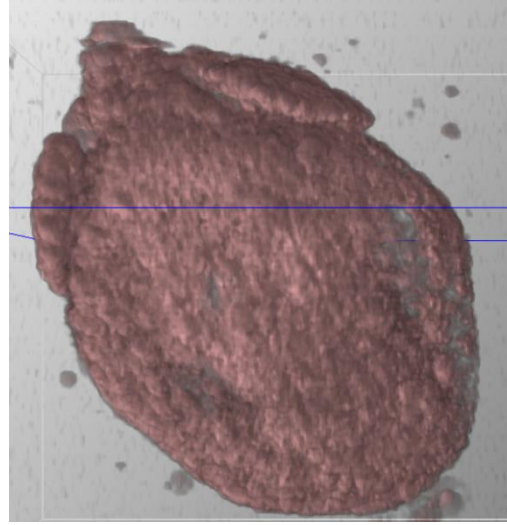


Figure 5.9. 3D ultrasound reconstruction of mouse heart APOE M1 16 weeks – Sample

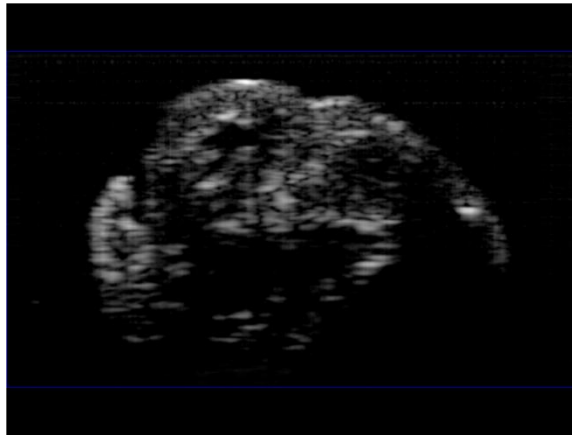
9.



(a) Optical image



(b) B-Mode cross section



(c) 3D reconstruction

Figure 5.10. 3D ultrasound reconstruction of mouse heart DKO M1 16 weeks – Sample 13.

From these results it can be seen that the morphology of the 3D reconstructed ultrasound match with the optical images of the hearts, showing the capabilities of the 3D reconstruction with different samples. Due to the early stage of the mouse heart samples (16 and 20 weeks) non major atherosclerotic plaque were found in these.

5.4. 3D Quantitative Assessment of Atherosclerotic Plaque

After an analysis of a 3D reconstruction, a 3D quantitative assessment of atherosclerotic plaque can be performed. 3D atherosclerotic plaque estimation for the region of interest was calculated by thresholding each B-mode image of the 3D sequence with the atherosclerotic plaque color (yellow) assigned in the 3D rendering. Atherosclerotic plaque was shown in yellow color in the Figures 5.3 to 5.6. After B-mode images are thresholded, the atherosclerotic plaque pixels in each image are counted. Finally, the atherosclerotic plaque in each B-mode image are added and multiplied by the voxel size of the high-resolution ultrasound acquisition. The previous method was developed in MATLAB 7.1 (The MathWorks, Inc., Natick, MA, USA). The volume of the atherosclerotic plaque in Figure 5.3 (c) was evaluated and found approximately as 0.015 mm^3 .

- CHAPTER 6 -

CONCLUSIONS & FUTURE WORK

In this work a real-time high-resolution 3D ultrasound imaging system is developed, allowing the 3D acquisition and imaging of high-resolution ultrasound data for biomedical applications. It includes the development of two graphical user interfaces in C++ to interact with a high-resolution ultrasound system and to imaging the high-resolution ultrasound data. In addition, a methodology is described and implemented in the system for 3D ultrasound reconstruction and visualization. The development of these GUIs allows easy 3D high-resolution ultrasound acquisition and imaging to any user with basic knowledge in ultrasound and with only minimal and faster training in the system and the GUIs. This capability opens the system to any researcher or person interested in performing experimentations with high-resolution ultrasound.

The high-resolution 3D ultrasound imaging system is tested to assess atherosclerosis using different mouse models. To assess atherosclerosis, a series of *in vitro* studies are performed to 3D scan vessels of mouse aortas and carotids vessels with atherosclerosis, as well as mouse hearts with atherosclerosis. The apolipoprotein E-knockout (APOE) and the apolipoprotein E-A1 adenosine receptor double knockout (DKO) mice model with their wild type control (C57) are used. Three-dimensional reconstructions were rendered showing good matches with the samples morphology. In addition, 3D sections of the data are reconstructed showing atherosclerotic plaque in the samples. The 3D ultrasound reconstruction allows for us to analyze a sample from outside and inside by rotating around any angle and cropping non-relevant data, allowing us to observe shape and appearance of the 3D structures. Also, 3D reconstruction allows us to reconstruct B-mode images of the cross sectional and longitudinal views, that were not available initially with the original transversal scans. As well, 3D image reconstructions were used to locate and select 2D regions of interest (ROI) precisely instead of using a reference point or a surgical needle. Finally, after reconstructing and analyzing the 3D ultrasound images, a 3D quantitative assessment of atherosclerotic plaque is performed. After analyzing the samples, the plaque lesions of DKO mouse

model exhibits smaller areas than those of the APOE mouse model. Additionally, the C57 mouse model was clean of any atherosclerosis. These findings are in agreement with a previous study of our group for these mouse models.

The 3D ultrasound acquisitions were limited to *in vitro* experiments that require killing the animals to get the samples. Therefore, future work should focus on developing high-resolution ultrasound *in vivo* experiments, which also will allow the long term monitoring of disease progression or treatment. On the other hand, it was difficult to quantitatively assess atherosclerotic components in the 3D ultrasound images using only the B-mode images, due to the low contrast-resolution between these and normal tissue. Consequently, the quantitative assessment of atherosclerotic plaque could be improved by the development of parametric imaging for tissue classification, which in addition will allow the imaging of 3D parametric images. Furthermore, the 3D high-resolution ultrasound imaging system can be tested with other samples, objects, or small animals. For example, in order to detect and imaging the progression of other diseases or to analyze 3D fractures in structures. Some of these challenges are currently on research in our laboratory at WVU.

REFERENCES

- [1] U. S. Government, "Chronic disease overview," 1999.
- [2] W. Rosamond, *et al.*, "Heart disease and stroke statistics - 2007 update - A report from the American Heart Association Statistics Committee and Stroke Statistics Subcommittee," *Circulation*, vol. 115, pp. E69-E171, Feb. 2007.
- [3] B. B. Goldberg and B. A. Kimmelman, *Medical Diagnostic Ultrasound: A Retrospective on Its 40th Anniversary*. New York, N.Y.: Eastman Kodak Company, 1988.
- [4] K. Tanaka, *Diagnosis of Brain Disease by Ultrasound*. Japan: Shindan-To-Chiryō Sha Co., Ltd., 1969.
- [5] W. J. Fry, "Action of ultrasound on nerve tissue. A review," *Journal of the Acoustical Society of America (SAUO)*, vol. 25, pp. 1-5, 1953.
- [6] I. Edler, "Mitral valve function studied by the ultrasound echo method," in *Proceedings of the First International Conference on Diagnostic Ultrasound*, Pittsburgh, Pa., 1965.
- [7] K. K. Shung, "Introduction," in *Diagnostic Ultrasound: Imaging and Blood Flow Measurements*, ed: CRC Press, 2005, pp. 1-4.
- [8] D. A. Christensen, "Diagnostic Imaging Configurations," in *Ultrasonic Bioinstrumentation*, ed: Wiley, 1988, pp. 123-174.
- [9] H. D. Crawford, *et al.*, "Transmission of ultrasound through living human thorax," *Medical Electronics, IRE Transactions on*, vol. ME-6, pp. 141-146, 1959.
- [10] S. Hakim, *et al.*, "Measurement of cranial bone thickness using A-mode ultrasound," in *Engineering in Medicine and Biology Society, 1997. Proceedings of the 19th Annual International Conference of the IEEE*, 1997, pp. 613-616 vol.2.
- [11] R. Youmaran, *et al.*, "Automatic detection of features in ultrasound images of the eye," in *Instrumentation and Measurement Technology Conference, 2005. IMTC 2005. Proceedings of the IEEE*, 2005, pp. 1829-1834.
- [12] J. Nakayama, *et al.*, "Imaging of a two-dimensional target by means of hologram matrix - An ultrasound experiment," *Proceedings of the IEEE*, vol. 66, pp. 1287-1289, 1978.
- [13] R. H. Smallwood and P. Dixon, "An electronic Doppler signal generator for assessing continuous-wave ultrasonic Doppler flowmeters," *Physical Science, Measurement and Instrumentation, Management and Education - Reviews, IEEE Proceedings*, vol. 133, pp. 104-108, 1986.
- [14] S. K. Holland, *et al.*, "Frequency-dependent attenuation effects in pulsed doppler ultrasound: Experimental results," *Biomedical Engineering, IEEE Transactions on*, vol. BME-31, pp. 626-631, 1984.
- [15] F. S. Foster, *et al.*, "Advances in ultrasound biomicroscopy," *Ultrasound in Medicine and Biology*, vol. 26, pp. 1-27, Jan. 2000.
- [16] M. D. Sherar, *et al.*, "Ultrasound Backscatter Microscopy Images the Internal Structure of Living Tumor Spheroids," *Nature*, vol. 330, pp. 493-495, Dec. 1987.

- [17] C. J. Pavlin, *et al.*, "Subsurface ultrasound microscopic imaging of the intact eye," *Ophthalmology*, vol. 97, pp. 244-250, Feb. 1990.
- [18] C. J. Pavlin, *et al.*, "Ultrasound biomicroscopic features of pigmentary glaucoma," *Canadian Journal of Ophthalmology-Journal Canadien D Ophthalmologie*, vol. 29, pp. 187-192, Aug. 1994.
- [19] C. R. Meyer, *et al.*, "Feasibility of high-resolution, intravascular ultrasonic-imaging catheters," *Radiology*, vol. 168, pp. 113-116, Jul. 1988.
- [20] S. E. Nissen, *et al.*, "Application of a new phased-array ultrasound imaging catheter in the assessment of vascular dimensions - In vivo comparison to cineangiography," *Circulation*, vol. 81, pp. 660-666, Feb. 1990.
- [21] K. Hoffmann, *et al.*, "20-MHz B-mode ultrasound in monitoring the course of localized scleroderma (morphea)," *Acta Dermato-Venereologica*, pp. 3-16, 1991.
- [22] K. Hoffmann, *et al.*, "Malignant-melanoma in 20-MHz B-scan sonography," *Dermatology*, vol. 185, pp. 49-55, 1992.
- [23] E. Cherin, *et al.*, "Ultrahigh frame rate retrospective ultrasound microimaging and blood flow visualization in mice in vivo," *Ultrasound in Medicine and Biology*, vol. 32, pp. 683-691, May. 2006.
- [24] D. H. Turnbull, *et al.*, "Ultrasound backscatter microscope analysis of early mouse embryonic brain-development," *Proceedings of the National Academy of Sciences of the United States of America*, vol. 92, pp. 2239-2243, Mar. 1995.
- [25] S. Srinivasan, *et al.*, "Noninvasive, in utero imaging of mouse embryonic heart development with 40-MHz echocardiography," *Circulation*, vol. 98, pp. 912-918, Sep. 1998.
- [26] F. S. Foster, *et al.*, "A new ultrasound instrument for in vivo microimaging of mice," *Ultrasound in Medicine and Biology*, vol. 28, pp. 1165-1172, Sep. 2002.
- [27] M. Mancini, *et al.*, "Morphological ultrasound microimaging of thyroid in living mice," *Endocrinology*, vol. 150, pp. 4810-4815, Oct. 2009.
- [28] J. C. Sullivan, *et al.*, "Novel use of ultrasound to examine regional blood flow in the mouse kidney," *American Journal of Physiology - Renal Physiology*, May. 2009.
- [29] A. Razuvaev, *et al.*, "Noninvasive real-time imaging of intima thickness after rat carotid artery balloon injury using ultrasound biomicroscopy," *Atherosclerosis*, vol. 199, pp. 310-316, Aug. 2008.
- [30] S. Andonian, *et al.*, "Real-time quantitation of renal ischemia using targeted microbubbles: In-vivo measurement of P-selectin expression," *Journal of Endourology*, Feb. 2009.
- [31] A. Stokvis, *et al.*, "High-resolution ultrasonography of the cutaneous nerve branches in the hand and wrist," *Journal of Hand Surgery (European Volume)*, Sep. 2009.
- [32] R. N. Rankin, *et al.*, "3-Dimensional donographic reconstruction - Techniques and diagnostic applications," *American Journal of Roentgenology*, vol. 161, pp. 695-702, Oct. 1993.
- [33] J. F. Greenleaf, *et al.*, "Multidimensional visualization in echocardiography - An Introduction," *Mayo Clinic Proceedings*, vol. 68, pp. 213-220, Mar. 1993.

- [34] A. Fenster and D. B. Downey, "3-D ultrasound imaging: A review," *IEEE Engineering in Medicine and Biology Magazine*, vol. 15, pp. 41-51, Nov-Dec. 1996.
- [35] A. Fenster, *et al.*, "Three-dimensional ultrasound imaging of the vasculature," *Ultrasonics*, vol. 36, pp. 629-633, Feb. 1998.
- [36] A. Fenster and D. B. Downey, "Three-dimensional ultrasound imaging," *Annual Review of Biomedical Engineering*, vol. 2, pp. 457-475, 2000.
- [37] S. W. Smith, *et al.*, "2-Dimensional arrays for medical ultrasound," *Ultrasonic Imaging*, vol. 14, pp. 213-233, Jul. 1992.
- [38] M. Pernot, *et al.*, "A 3D elastography system based on the concept of ultrasound-computed tomography for *in vivo* breast examination," in *Ultrasonics Symposium, 2006. IEEE, 2006*, pp. 1037-1040.
- [39] R. Seip, *et al.*, "Remotely operated robotic high intensity focused ultrasound (HIFU) manipulator system for critical systems for trauma and transport (CSTAT)," in *Ultrasonics Symposium, 2006. IEEE, 2006*, pp. 200-203.
- [40] C. D. Barry, *et al.*, "Three-dimensional freehand ultrasound: Image reconstruction and volume analysis," *Ultrasound in Medicine and Biology*, vol. 23, pp. 1209-1224, 1997.
- [41] R. W. Prager, *et al.*, "Rapid calibration for 3-D freehand ultrasound," *Ultrasound in Medicine and Biology*, vol. 24, pp. 855-869, Jul. 1998.
- [42] P. C. Li, *et al.*, "Tissue motion and elevational speckle decorrelation in freehand 3D ultrasound," *Ultrasonic Imaging*, vol. 24, pp. 1-12, Jan. 2002.
- [43] A. Fenster, *et al.*, "3D ultrasound analysis of carotid plaque volume and surface morphology," *Ultrasonics*, vol. 44, pp. E153-E157, Dec. 2006.
- [44] A. M. Duckelmann and K. D. Kalache, "Three-dimensional ultrasound in evaluating the fetus," *Prenatal Diagnosis*, vol. 30, pp. 631-638, Jul. 2010.
- [45] H. C. Stary, *et al.*, "A definition of advanced types of atherosclerotic lesions and a histological classification of atherosclerosis - A report from the committee on vascular-lesions of the council on arteriosclerosis, American-Heart-Association," *Circulation*, vol. 92, pp. 1355-1374, Sep. 1995.
- [46] D. Baumgart, *et al.*, "Comparison of electron beam computed tomography with intracoronary ultrasound and coronary angiography for detection of coronary atherosclerosis," *Journal of the American College of Cardiology*, vol. 30, pp. 57-64, Jul. 1997.
- [47] H. Sakuma, *et al.*, "MR measurement of coronary blood flow," *Journal of Magnetic Resonance Imaging*, vol. 10, pp. 728-733, Nov. 1999.
- [48] G. Y. Chang, *et al.*, "Positron emission tomography imaging of conditional gene activation in the heart," *Journal of Molecular and Cellular Cardiology*, vol. 43, pp. 18-26, Jul. 2007.
- [49] S. N. Roper, *et al.*, "In vivo detection of experimentally induced cortical dysgenesis in the adult rat neocortex using optical coherence tomography," *Journal of Neuroscience Methods*, vol. 80, pp. 91-98, Mar. 1998.
- [50] O. Aristizabal, *et al.*, "40-MHz echocardiography scanner for cardiovascular assessment of mouse embryos," *Ultrasound in Medicine and Biology*, vol. 24, pp. 1407-1417, Nov. 1998.

- [51] J. E. Wilhjelm, *et al.*, "Quantitative analysis of ultrasound B-mode images of carotid atherosclerotic plaque: Correlation with visual classification and histological examination," *IEEE Transactions on Medical Imaging*, vol. 17, pp. 910-922, Dec. 1998.
- [52] A. Landry, *et al.*, "Measurement of carotid plaque volume by 3-dimensional ultrasound," *Stroke*, vol. 35, pp. 864-869, Apr. 2004.
- [53] J. C. R. Seabra, *et al.*, "A 3-D ultrasound-based framework to characterize the echo morphology of carotid plaques," *IEEE Transactions on Biomedical Engineering*, vol. 56, pp. 1442-1453, May. 2009.
- [54] C. D. Ainsworth, *et al.*, "3D ultrasound measurement of change in carotid plaque volume - A tool for rapid evaluation of new therapies," *Stroke*, vol. 36, pp. 1904-1909, Sep. 2005.
- [55] J. Baglione and J. D. Smith, "Quantitative assay for mouse atherosclerosis in the aortic root," *Methods in Molecular Medicine*, vol. 129, pp. 83-95, 2006.
- [56] A. M. Mahmoud, *et al.*, "High frequency precise ultrasound imaging system to assess mouse hearts and blood vessels," in *Proceedings of the ASME 2008 Summer Bioengineering Conference*, FL, 2008.
- [57] A. M. Mahmoud, *et al.*, "High-frequency tissue classification of atherosclerotic plaques in an APOE-KO mouse model using spectral analysis," in *Proceedings of the ASME International Mechanical Engineering Congress and Exposition (IMECE)*, 2009, pp. 505-508.
- [58] K. K. Shung, "Gray-scale ultrasonic imaging," in *Diagnostic Ultrasound: Imaging and Blood Flow Measurements*, ed: CRC Press, 2005, pp. 79-101.
- [59] S. S. Young, *et al.*, *Signal Processing and Performance Analysis for Imaging Systems*. Norwood, MA.: Artech House, 2008.
- [60] C. H. Frazier and W. D. O'Brien, "Synthetic aperture techniques with a virtual source element," *IEEE Transactions on Ultrasonics Ferroelectrics and Frequency Control*, vol. 45, pp. 196-207, Jan. 1998.
- [61] M. L. Li, *et al.*, "Improved synthetic aperture focusing technique with applications in high-frequency ultrasound imaging," *IEEE Transactions on Ultrasonics Ferroelectrics and Frequency Control*, vol. 51, pp. 63-70, Jan. 2004.
- [62] A. Mahmoud, "Novel techniques for tissue imaging and characterization using biomedical ultrasound," Ph.D. dissertation, Dept. Mech. and Aero. Eng., West Virginia Univ., Morgantown, WV, 2009.
- [63] J. H. Chang, *et al.*, "A novel envelope detector for high-frame rate, high-frequency ultrasound imaging," *IEEE Transactions on Ultrasonics Ferroelectrics and Frequency Control*, vol. 54, pp. 1792-1801, Sep. 2007.
- [64] M. Schlaikjer, *et al.*, "Trade off study on different envelope detectors for B-mode imaging," in *Ultrasonics, 2003 IEEE Symposium on*, 2003, pp. 1938-1941 Vol.2.
- [65] H. E. Rowe, *Signals and Noise in Communication Systems*. Princeton, N.J.: Van Nostrand, 1965.
- [66] "Standard test form (TP103) for ultrasound transducer," Olympus NDT Inc., Waltham, MA., May. 2009.
- [67] A. Mahmoud, *et al.*, "High-resolution quantitative ultrasound imaging for tissue classification of atherosclerosis in mouse models," *Annals of Biomedical Engineering*, Submitted.

- [68] J. Meyer-Spradow, *et al.*, "Voreen: A Rapid-Prototyping Environment for Ray-Casting-Based Volume Visualizations," *IEEE Computer Graphics and Applications*, vol. 29, pp. 6-13, 2009.
- [69] D. Sun, *et al.*, "Mediation of tubuloglomerular feedback by adenosine: evidence from mice lacking adenosine 1 receptors," in *Proceedings of the National Academy of Sciences USA (PNAS)* 2001, pp. 9983-9988.
- [70] B. Teng, *et al.*, "Isolation and characterization of coronary endothelial and smooth muscle cells from A1 adenosine receptor-knockout mice," *American Journal of Physiology - Heart and Circulatory Physiology*, vol. 290, pp. H1713-1720, Nov. 2006.
- [71] B. Teng, *et al.*, "Reduced Atherosclerotic Lesions in A1 Adenosine Receptor (AR)/Apolipoprotein E (APOE) Double Knockout mice: Role for A1 AR in the Development of Atherosclerosis.," *Arteriosclerosis, Thrombosis, and Vascular Biology*, vol. 29, pp. e73-74, Jul. 2009.